

**Study on Development of  
Novel Multi-Component Mg-Based Alloys  
by Rapid Solidification Technology  
Using of Twin Roll Casting**

**双ロール鋳造を用いた急冷凝固技術による  
新規多成分 Mg 系合金の開発に関する研究**

**Zhipu Pei**

**Saitama Institute of Technology**

**February, 2018**



## Table of Contents

Preface .....	I
<b>Chapter 1 Introduction .....</b>	<b>1</b>
1.1 Background and history of metallic glasses and nanocrystalline alloys .....	2
1.1.1 Metallic glasses, nanocrystalline alloys and quasicrystals .....	2
1.1.2 Metallic glasses and nanocrystalline alloys .....	6
1.2 Rapid solidification techniques in producing metallic glasses .....	14
1.2.1 Rapid solidification apparatuses .....	14
1.2.2 Rapid solidification of twin roll strip casting technique .....	20
1.3 Material selection and process determination.....	25
1.3.1 Material selection .....	26
1.3.2 Process determination .....	31
1.4 Purpose of this thesis .....	34
References .....	37
<b>Chapter 2 Kinetics of rapid solidification on microstructure and alloy composition design ....</b>	<b>49</b>
2.1 Thermodynamics and kinetics of glass formation .....	49
2.1.1 Thermodynamic stability of metallic glasses .....	49
2.1.2 Kinetics of glass formation .....	51
2.2 Evaluation of critical cooling rate .....	52
2.2.1 Calculation of time reduced-temperature transformation and CCT diagrams .....	54
2.2.2 Estimation of the critical cooling rates using CCT curves .....	57
2.2.3 Process programming—transition from TTT diagram to CCT diagram.....	59
2.3 Criteria of glass forming ability .....	60
2.3.1 Characteristics of bulk metallic glasses .....	60
2.3.2 Three empirical rules for estimating glass forming ability.....	62
2.4 Topological models of bulk glass formers .....	62
2.5 Alloy composition design .....	67
2.6 Concluding remarks .....	70
References .....	72
<b>Chapter 3 Simulation of solidification behavior during twin roll casting .....</b>	<b>75</b>
3.1 Introduction.....	75
3.2 Pilot vertical type twin roll caster .....	76
3.3 Simulation of twin roll strip casting .....	80
3.3.1 Simplifications, boundary conditions and governing equations .....	80

3.3.2 Thermal flow simulation .....	82
3.4 Results and discussion .....	83
3.5 Concluding remarks .....	89
References .....	90
<b>Chapter 4 TRC experiment and microstructure analyses .....</b>	<b>93</b>
4.1 Experiment.....	93
4.1.1 Enlightenment form normal TRC experiment .....	94
4.1.2 Rapid solidification of TRC process .....	96
4.2 X-ray diffraction analysis.....	106
4.3 TEM analysis .....	110
4.3.1 Sample preparation by focused ion beam (FIB) milling technique .....	110
4.3.2 TEM analysis results .....	112
4.4 Corrosion properties.....	114
4.4.1 Surface morphology of the AZ31 Light sheet after corrosion.....	115
4.4.2 Surface morphology of the AZ31-In-Sn alloy sheet after corrosion.....	116
4.4.3 Surface morphology of the Mg-RE alloy sheet after corrosion .....	118
4.4.4 Corrosion mechanism exploration .....	120
4.5 Mechanical properties of the dual phase Mg-RE alloy .....	123
4.6 Concluding remarks .....	126
References .....	127
<b>Chapter 5 Summary and prospect .....</b>	<b>129</b>
5.1 Summary.....	129
5.2 Prospect.....	130
References .....	132
<b>Appendix.....</b>	<b>133</b>
<b>Related Publications .....</b>	<b>135</b>
<b>ACKNOWLEDGEMENTS .....</b>	<b>137</b>

## Preface

Magnesium and its alloys have a diverse range of markets and applications due to their advantageous characteristics. However, their utilization is limited by the restricted plasticity and corrosion resistance. In recent years, metallic glass (metallic amorphous materials) has received great attention and made a lot of progress. However, the preparation technology of amorphous materials is complex, and the high processing cost is one of the major topics at present. In order to solve these problems, this paper mainly proposed a low cost, easy to achieve rapid solidification technology to prepare Mg-based amorphous or amorphous and fine grain mixed materials. This work has two main purposes: (i) proposing a new multi-component magnesium-based alloy design method and its theory and (ii) using twin-roll casting technology to prepare amorphous or amorphous and fine grain mixed materials. Improved ductility and better corrosion resistance are expected in our materials.

Chapter 1 firstly introduces the background of metallic glasses, nanocrystalline alloys and strip casting technology. Purpose of this thesis was proposed at the last of this chapter.

In Chapter 2, using the homogeneous nucleation theory, time temperature transition (TTT) diagram which indicates the transformation of crystalline phase from supercooled liquid state was plotted. Based on the additivity rule, continuous cooling transformation (CCT) diagram was transformed from the TTT diagram. Critical cooling rates of materials to form metallic glasses were estimated using the CCT diagrams. Referring to the criteria for the formation of bulk metallic glasses and considering the effects of alloying elements to Mg, three kinds of alloys (i.e., AZ31, AZ31-In-Sn and Mg-RE) were put forward as the objects for our study.

In Chapter 3, thermal-flow simulation was carried out to calculate the thermal and flow phenomena during twin roll casting (TRC) of magnesium alloys. Cooling rates with 3 to 4 orders of magnitude by the vertical type twin roll casting (VTRC) process under the current conditions can be attained, which shows that VTRC technique has a potential ability in continuous fabrication of Mg-based bulk amorphous or amorphous phase and fine crystalline phase dual-phase alloys in sheet form.

In Chapter 4, rapid solidification of TRC experiments were conducted. The Mg-RE alloy strip exhibited good corrosion resistance and higher ultimate tensile strength and elongation comparing to the as-cast AZ31 alloy strips. The elongation of Mg-RE alloy strip is also high than the AZ91 and ZK61 under powder metallurgy processing. These indicate that Mg-RE alloy produced by our method has a better ductility. Electron probe micro-analysis (EPMA) results and Transmission electron microscopy (TEM) analyses show that the quasi-amorphous phase has a high concentration in Al and RE element, which results in the fact that the quasi-amorphous phase has a better glass forming ability (GFA) than the matrix phase.

Finally, conclusions and expositions of the dissertation are given in Chapter 5, and some future research directions are also proposed.

### Chapter 1 Introduction

Considering the impact of modern industry on environment and sustainable development, new materials and new processes are expected and many researchers devote themselves to these fields. It has been clarified that noncrystalline and nanocrystalline alloys have new alloy compositions and new atomic configurations which differ from those of crystalline alloys. These features have facilitated the appearance of various characteristics, such as good mechanical properties, useful physical properties and unique chemical properties which have not been obtained from conventional crystalline alloys <sup>[1]</sup>. This chapter is intended to introduce the development history of noncrystalline alloys (metallic glasses) and summarize recent works on nanocrystalline alloys. Their synthesis techniques with a focus on twin roll casting process were also pointed out. Taking aim at developing new Mg-based materials by rapid solidification techniques, the main purposes of this thesis are stated at last of this chapter.

To begin with this part, for the sake of avoiding ambiguity and confusion, the author would like to characterize several terms (noncrystalline, amorphous, glassy) which are being used in describing noncrystalline materials in literature <sup>[2]</sup>:

“Noncrystalline” is a generic term to describe any solid material that does not possess crystallinity. The noncrystalline solids formed by continuous cooling processes from their liquid states are called “glass.” (This is because that people were able to produce glasses only from the liquid state at beginning), while a solid is defined as any body having a viscosity greater than  $10^{14}\text{P}$  ( $10^{13}\text{Pa}\cdot\text{s}$ ), although this value is a somewhat arbitrary <sup>[3]</sup>. On the other hand, a noncrystalline material, obtained by any other process (e.g., vapor deposition or solid-state processing methods such as mechanical alloying) but not directly from the liquid state, is called “amorphous” material. It should be

## Chapter 1 Introduction

recognized that both glasses and amorphous solids are noncrystalline. In this thesis, the materials were produced by continuous cooling from the liquid state and if there was a noncrystalline phase, it should be called “glass”. In summary:

*Glass* is any noncrystalline solid obtained by continuous cooling from the liquid state, and *amorphous solid* is any noncrystalline material obtained by any other method, except by continuous cooling from the liquid state.

### 1.1 Background and history of metallic glasses and nanocrystalline alloys

#### 1.1.1 Metallic glasses, nanocrystalline alloys and quasicrystals

A perfect crystal is a three-dimensional periodic or quasi-periodic array of atoms, which in a regular repeating structure of atoms and is infinite in extent <sup>[4]</sup>. Solids which are deviating from this perfectly ordered structure could be divided into two classes <sup>[5]</sup>: One is obtained by thermally disordering crystalline structure of a material and freezing-in the disordered state by means of quenching. A glass may be considered as a solid with frozen-in liquid structure <sup>[3]</sup>. A two-dimensional hard sphere model of a glass is shown in Fig. 1.1(a) in comparison to a perfect crystal of hard spheres (Fig. 1.1(b)). In most glassy materials, the density and the nearest neighbor coordination varies typically by a few percent relative to the perfect crystal <sup>[5]</sup>.

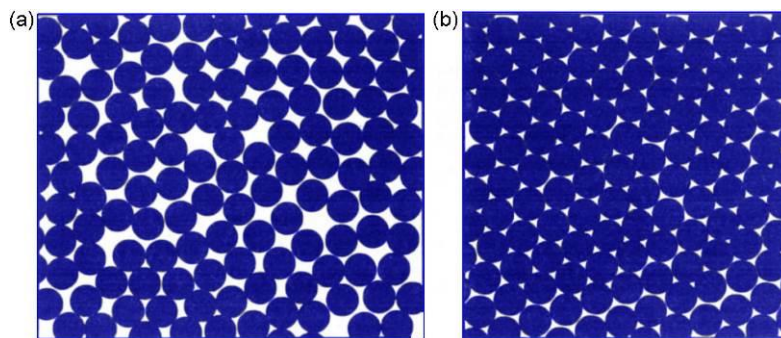


Fig. 1.1 Hard sphere model of (a) a two-dimensional glassy structure, and (b) a two-dimensional structure of a perfect crystal (hexagonal array of atoms).



## Chapter 1 Introduction

As shown in Fig. 1.2, the other class of disordered materials deviated from the perfect crystal has a characteristic that the disorder is induced by incorporating defects (e.g., vacancies, dislocations and grain or interphase boundaries). Atomic density and coordination in the defect core region are significantly altered by atomic displacements associated with the incorporation of defects.

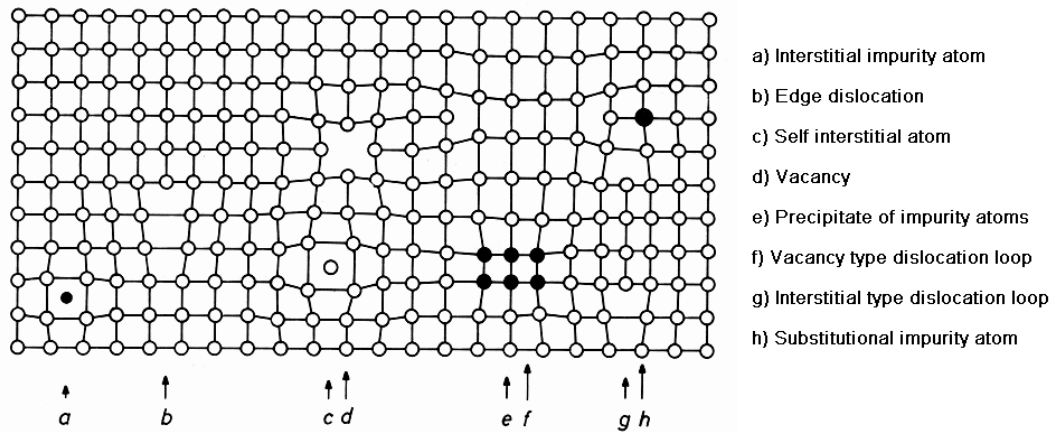


Fig. 1.2 Schematic drawing of various crystal lattice defects. ([http://www.tf.uni-kiel.de/matwis/amat/def\\_en/](http://www.tf.uni-kiel.de/matwis/amat/def_en/))

The structural changes obtained by freezing-in the high temperature atomic arrangement is different from the structural changes caused by the incorporation of defects of the same material because both structures have different physical origin. The former is due to the thermal energy stored in the material. The latter (defect core structure) is caused by the incompatibility introduced into the lattice in the form of a defect and does not require any thermal energy <sup>[5]</sup>. In the specific case of grain boundaries, the atomic structure of the boundary core is a two-dimensional periodic arrangement of atoms <sup>[6]</sup>, which in another way indicates the difference between the defect-induced disorder and the thermally induced disorder. In conventional polycrystals (grain size typically  $\geq 1 \mu\text{m}$ ) the atomic structures of the boundary cores are not noticed in most structural investigations such as X-ray diffraction, Extended X-Ray Absorption Fine Structure (EXAFS), spectroscopic studies, because the fraction of atoms located in the core of the boundaries is  $10^{-4}$  or less. However, if one generates a

## Chapter 1 Introduction

material which contains such a high density of defects that 50% or more of the atoms are situated in the cores of defects, then the atomic structure of the entire material depends on the core structures of the defects. This is the basic idea of nanocrystalline materials. They have a common microstructural feature that a large volume fraction of defect cores which contain 50% or more atoms (molecules) are the main structure and (strained) crystal lattice regions are consisted in them. Fig. 1.3 shows the structure of a two-dimensional nanocrystalline material.

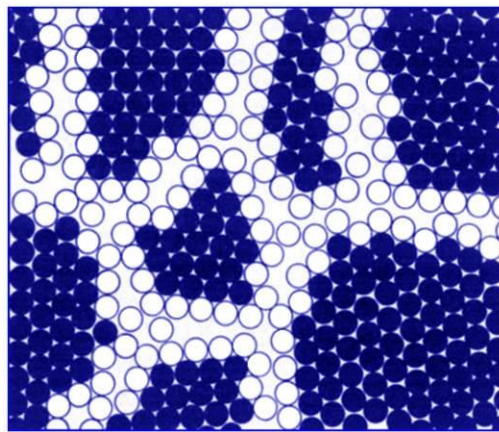


Fig. 1.3 Atomic structure of a two-dimensional nanocrystalline material. Atoms (hexagonal arrays) in the centers of the “crystals” are indicated in filled circles. The ones in the boundary core regions are represented by open circles <sup>[5]</sup>.

Generally speaking, a nanocrystalline material is a polycrystalline material with a crystallite size of only a few nanometers, which is commonly defined as a crystallite (grain) size below 100 nm. It fills the gap between amorphous materials and conventional coarse-grained materials. Grain sizes from 100~500 nm are typically considered “ultrafine” grains. The grain size of a nanocrystalline sample can be estimated using X-ray diffraction <sup>[7, 8]</sup>. In materials with very small grain sizes, the diffraction peaks will be broadened. This broadening can be related to a crystallite size using the Scherrer equation\* (applicable up to ~50 nm), a Williamson-Hall plot, or more sophisticated methods such as the Warren-Averbach method or computer modeling of the diffraction pattern. The crystallite size can be measured directly using transmission

## Chapter 1 Introduction

electron microscopy<sup>[1]</sup>.

\*The equation is  $D_{hkl} = K\lambda/B_{hkl} \cos\theta$ <sup>[9]</sup>, where  $D_{hkl}$  is the crystallite size in the direction perpendicular to the lattice planes,  $hkl$  are the Miller indices of the planes being analyzed,  $K$  is a numerical factor frequently referred to as the crystallite-shape factor,  $\lambda$  is the wavelength of the X-rays,  $B_{hkl}$  is the width (full-width at half-maximum) of the X-ray diffraction peak in radians and  $\theta$  is the Bragg angle. In addition to depending on the crystallite shape, the numerical factor  $K$  also depends on the definitions of the average crystallite size (for example, if the cube root of the crystallite volume is used instead of the definition above) and the width (for example, if the integral line width is used, as in von Laue's derivation of Scherrer's formula, rather than the full width at half-maximum, which is usually easier to obtain from experimental data). The structure of the formula is not affected by these definitions, but the numerical value of  $K$  may change appreciably. Using the above definition of  $D_{hkl}$ , and in the absence of detailed shape information,  $K = 0.9$  is a good approximation. It is important to note that Scherrer's equation can only be applied for average sizes up to about 100–200 nm (depending on the instrument, sample, and signal-to-noise ratio), because diffraction-peak broadening decreases with increasing crystallite size and it becomes difficult to separate the peak broadening due to crystallite size from the broadening due to other factors.

Different from the crystal (possessing long-range translational symmetry) and noncrystal (absence of long-range order), Shechtman et al. reported another type of solid in 1984 which is now referred to quasicrystal<sup>[10]</sup>. Quasicrystals constitute a new class of condensed matter characterized by a non-crystallographic orientational symmetry<sup>[11]</sup>. Most quasicrystals produced by non-equilibrium processes such as rapid quenching are metastable. About a decade later, after the discovery of quasicrystals, there were still numerous basic questions need to be answered<sup>[11]</sup>. Another decade past, in 2004, Inoue<sup>[12]</sup> wrote an article which mentioned quasicrystal and summarized the properties and application fields. Even in recent years<sup>[13-15]</sup>, researches in this field are almost all based on the lattice structure models proposed in the early age. The basic questions still exist.

In summary of the above, we list some striking features of metallic glasses, nanocrystals and quasicrystals in Table 1.1 to give these materials a brief description.

## Chapter 1 Introduction

Table 1.1 Characteristics of metallic glasses, nanocrystalline materials and quasicrystals.

	Characteristics	Ref.
Metallic glasses	Atomic arrangement is random. Lack of long-range atomic order and very similar to a frozen-in liquid. Metastable state. Absence of dislocation-mediated slip.	[16-19]
Nanocrystalline materials	Crystallite (grain) size below 100 nm. Structurally characterized by a large volume fraction of grain boundaries. Contain a high density of interfaces, a substantial fraction of atoms lie in the interfaces	[5, 20, 21]
Quasicrystals	A rotational symmetry structure, but no translational symmetry, exists over large distances. Its diffraction spots are as sharp as those of crystals but cannot be indexed to any Bravais lattice. The solid is metastable and forms from the melt by a first-order phase transition*.	[2, 10, 11]

\*First-order phase transition (discontinuous phase transition): A transition in which the molar Gibbs energies or molar Helmholtz energies of the two phases (or chemical potentials of all components in the two phases) are equal at the transition temperature, but their first derivatives with respect to temperature and pressure (for example, specific enthalpy of transition and specific volume) are discontinuous at the transition point, as for two dissimilar phases that coexist and that can be transformed into one another by a change in a field variable such as pressure, temperature, magnetic or electric field. Example: The transition on heating CsCl to 752K at which it changes from the low-temperature, CsCl-type structure to the high-temperature NaCl-type structure [22].

### 1.1.2 Metallic glasses and nanocrystalline alloys

#### (1) Metallic glasses

Metallic glasses are currently the focus of intense research in the international metals community due to their special microstructure and properties. Setting aside elevated-temperature applications, these amorphous materials have exciting potential for structural applications [23]. Despite the flurry of activity, it is still a mystery about

## Chapter 1 Introduction

those questions on the development, structure and physical properties of this new phase.

Glass-forming systems have been found in all major bonding classes, including covalent, ionic, van der Waals, hydrogen bond, and metallic <sup>[24]</sup>. The forming of metallic glasses (MGs) needs extremely high cooling rates (on the order of  $10^5$  to  $10^6$  K/s) due to the non-directional nature of metallic bonds and the fact that metals are comprised of individual spherical atoms, as opposed to non-spherical compounds such as SiO<sub>2</sub> and other oxide glasses. Within metals, individual atoms can rearrange quickly into lower energy configurations or crystalline phases, thus a higher cooling rate is required to avoid crystallization <sup>[25]</sup>.

Pol Duwez and his colleagues at the California Institute of Technology (CalTech) were the first to successfully quench a binary Au–Si eutectic composition (Au<sub>75</sub>Si<sub>25</sub>) fast enough to form a metallic glass upon cooling from the melt <sup>[26]</sup>. There is an interesting phenomenon that in most of the papers <sup>[24, 27-35]</sup>, it is said that the first metallic glass phase was formed by continuous cooling from melt in 1960. This may be due to the fact that Duwez's group published their work in the year of 1960 <sup>[26]</sup>. Actually, in 1981 <sup>[36]</sup>, a historical description about the discovery of metallic glasses was provided by Duwez himself, it points out that the very thin foil of the first metallic glass was obtained in September 1959. The amorphous foil was quite unstable and crystallization could have occurred during the 3 hours exposure in the Debey-Scherrer camera <sup>[36]</sup>.

In 1961, Cohen and Turnbull pointed out that the glass-forming tendency (for a given cooling rate and for substances of a given molecular type) is greater the lower is the reduced melting temperature <sup>[37]</sup>:

$$\tau_m = \frac{kT_m}{h_v} \quad (1-1)$$

## Chapter 1 Introduction

where  $T_m$  is the thermodynamic crystallization temperature, and  $h_v$  is the molecular heat of vaporization. In consulting a compilation of phase diagrams, Duwez found that quite a few binary alloys between a metal and a semimetal (similar to Au-Si) had a eutectic point at a rather low temperature compared to that of the metal. In the subsequent development of alloy systems susceptible to be quenched into glasses, Duwez group replaced the Au into Pd in considering the thermal instability of Au-Si amorphous alloys, because the metal Pd have a higher melting point (thermal stability) <sup>[36, 38]</sup>. Hot on the heels of the discovery of amorphous Pd-20 at.%Si alloy, Chen and Turnbull reported the existence of glass transition temperature for the first time <sup>[39, 40]</sup> in the late 1960s. It is worth to mention that Angell <sup>[41]</sup> pointed out that the presence of  $T_g$  is not essential for a material to be called a glass in 1995.

In 1965 AuCo metallic glass was initially investigated as a ferromagnetic material by Duwez group. As the ferromagnetic metallic glass was synthesized by vapor deposition, the thickness of the alloy films are in the range of 200~600 Å <sup>[42]</sup>. In order to obtain stronger ferromagnetic metallic glassy materials, Fe-P alloy system was developed. In 1967, the first strongly ferromagnetic metallic glass Fe<sub>75</sub>P<sub>15</sub>C<sub>10</sub> was discovered by a scientific serendipity <sup>[43]</sup>. It was the prototype for all the ferromagnetic metallic glasses which have been extensively studied during the next decade.

In 1969 on the bases of studying the Pd-Si alloy system extensively, Chen and Turnbull formed the amorphous alloys with thicknesses up to 1 mm. They also found that glasses of Pd-Si binary alloys were less stable than corresponding ternary alloys containing 2~10 at.% noble metals <sup>[40]</sup>. With further optimization Chen and collaborators (1974) used simple suction-casting methods to develop ternary Pd-Cu-Si metallic glass rods in millimeter diameter (1~3 mm) at a significantly lower cooling rate estimated to be less than 10<sup>3</sup> K/s <sup>[44, 45]</sup>. In the paper Johnson wrote in 1999, there is a

## Chapter 1 Introduction

comment on the ternary materials produced by Chen group that if one arbitrarily defines the millimeter scale as “bulk”, then these ternary glasses were perhaps the first examples of “bulk” metallic glasses <sup>[45]</sup>. These materials are opposed to “traditional metallic glasses” where one sample dimension is very thin ( $\sim 50\text{ }\mu\text{m}$ ) due to the required high critical cooling rate (CCR).

Beginning in 1982, Turnbull and collaborators also developed a fluxing technique, which reduced heterogeneous nucleation at the sample surface, resulting in a much lower CCR <sup>[46, 47]</sup>. They carried out experiments on Pd-Ni-P alloys using boron oxide fluxing to dissolve heterogeneous nucleation centers into surface coating. The alloy  $\text{Pd}_{40}\text{Ni}_{40}\text{P}_{20}$  could be quenched from its molten to glass state in virtually bulk form at cooling rates of only 1 K/s.

A significant development made by Inoue in the late 1980s was the production of La-based three- and four-component “bulk metallic glass” (BMG) alloys with critical casting thickness of several millimeters <sup>[48, 49]</sup>. They produced 1.2 mm diameter rods of  $\text{La}_{55}\text{Al}_{25}\text{Ni}_{20}$  alloy in a fully glassy condition by water quenching (having a solidification rate about  $10^2\sim 10^3\text{ K/s}$ ) in 1989 <sup>[50]</sup>. This is the first time that glass formation was demonstrated in such size in an alloy without the presence of a noble metal.

In the early 1990s <sup>[51, 52]</sup>, again at CalTech, Johnson and co-workers developed a number of five-component Zr-based series alloys ( $\text{Zr}_{41.2}\text{Ti}_{13.8}\text{Cu}_{12.5}\text{Ni}_{10.0}\text{Be}_{22.5}$ ), called “Vitreloy”. Bulk metallic glasses (BMGs) have indeed been difficult to obtain, and BMG-forming compositions mostly have been discovered only since 1990 <sup>[23]</sup>. From this period, metallic glassy materials are entering into the *Bulk Age*.

More on the development of metallic glasses can be found in Refs. <sup>[33, 45, 53-57]</sup>. A

## Chapter 1 Introduction

summary of these historical developments is presented in Table 1.2, which clearly illustrates the trends of increased alloy complexity and decreasing CCR.

Table 1.2 Chronology of metallic glass development illustrating increasing alloy complexity and decreasing CCR <sup>[25, 34]</sup>.

Year		Alloy		Researcher	Critical cooling rate (K/s)	Cooling method
1960s	1960	Au-Si		Duwez group	10 <sup>5</sup> -10 <sup>6</sup>	
	1965	Pd-Si			“Gun quenching” or “piston and anvil technique” <sup>[38, 43, 58]</sup>	
	1965	ferromagnetic materials	Au-Co			
	1966		Pd-Co-Si, Pd-Ni-Si, Pd-Fe-Si			
	1967		(prototype)			Fe <sub>75</sub> P <sub>15</sub> C <sub>10</sub>
	1969	Pd-Si, Pd-Cu-Si		Turnbull, Chen	10 <sup>5</sup>	
1970s	1974	Pd-Cu-Si (BULK)		Chen	10 <sup>3</sup>	
1980s	1982	Pd-Ni-P (Fluxing Method)		Greer, Turnbull	10	
	The late 1980s	La-Al-Ni, La-Al-Cu, La-Al-Cu-Ni Mg-Y-Cu, Mg-Y-Ni Zr-Cu-Ni-Al		Inoue	10 <sup>2</sup>	
Bulk Age (1990s~)	1989	La <sub>55</sub> Al <sub>25</sub> Ni <sub>20</sub>		Inoue	10 <sup>2</sup> ~10 <sup>3</sup> K/s	
	1991~1993	La <sub>55</sub> Al <sub>25</sub> Ni <sub>10</sub> Cu <sub>10</sub>			High-pressure die casting	
		Mg-Cu-Y			Copper mold injection casting <sup>[59]</sup>	
			Zr-Ti-Cu-Ni-Be		Peker, Johnson	1

Metallic glasses have been produced in the forms of flakes, droplets, ribbons, wires, sheets, and bulk since the initial investigations. Metallic glasses in bulk form have sections thicker than 1 mm, whereas ribbons can be as thin as few microns <sup>[34]</sup>. They



## Chapter 1 Introduction

have been commercialized in applications for engineering, medicine, electronics, military, sports, jewelry making, etc. Despite the approaches have been made in this field, we are only in an early stage of exploiting the full potential of metallic glasses and there are many opportunities worth pursuing <sup>[23]</sup>.

### (2) Nanocrystalline alloys

Bulk nonequilibrium alloys, e.g., bulk amorphous, nanocrystalline and nanoquasicrystalline alloys, exhibit unique characteristics which cannot be obtained from conventional materials <sup>[60]</sup>.

In the late of 1980s Gleiter and co-workers synthesized a new class of material called nanocrystalline material, it has grain sizes of 1~50 nm <sup>[5]</sup>. Many properties of this material are reported to be remarkably different from those of normal coarse-grained polycrystalline materials and glasses <sup>[61]</sup>. Rapid solidification, deposition techniques and solid state reaction method are the main ways of synthesizing nanocrystalline materials. Among the above methods, manufacturing these materials from their amorphous precursors is of high level of international scientific interest for researchers.

In 1990, K. Lu reported a method to prepare nanocrystalline alloys by crystallizing amorphous alloys <sup>[61]</sup>. Precursory ordered clusters formed during annealing of amorphous alloys and then followed by nucleation and growth of crystallites. As a raw material, the amorphous alloys were made by rapid solidification from liquid state and in the form of ribbon, string or particles. Fe-based, Ni-based and Pd-based nanometer-sized crystalline materials had been prepared by them. Annealing temperature and time were two crucial factors of this process.

Zr-Al-Cu based bulk nanocrystalline alloys with high tensile strength and good

ductility were prepared by annealing their amorphous counterpart alloys for different times in the temperature range between  $T_g$  and  $T_x$  ( $T_g$  and  $T_x$  represent the glass-transition and crystallization temperature, respectively), followed by water quenching <sup>[62]</sup>. Pd was added into  $Zr_{60}Al_{10}Cu_{30}$  amorphous alloy for the formation of nanostructure. The good mechanical properties of the bulk nanostructured alloys were presumably due to the remaining amorphous phase can contain a number of free volumes by water quenching process after annealing.

Effects of diffusion processes induced by heat treatment on modern bulk amorphous and nanocrystalline materials were studied by Konrad Gruszka <sup>[7]</sup>. Through controlled thermal treatment of base amorphous alloys, nanocrystalline grains in suitably small sizes which surrounded by amorphous matrix could be obtained. Changes in the phase structure of  $Fe_{62-x}Co_{10}Y_8Me_xB_{20}$  ( $Me = Cr, Be$  or  $Cu$ ;  $x = 0$  or  $1$ ) alloy were investigated. Fig. 1.4 and Fig. 1.5 show the X-ray diffraction patterns and electronograms of the above alloys before and after the thermal treatment, which indicate the glassy and crystalline states respectively.

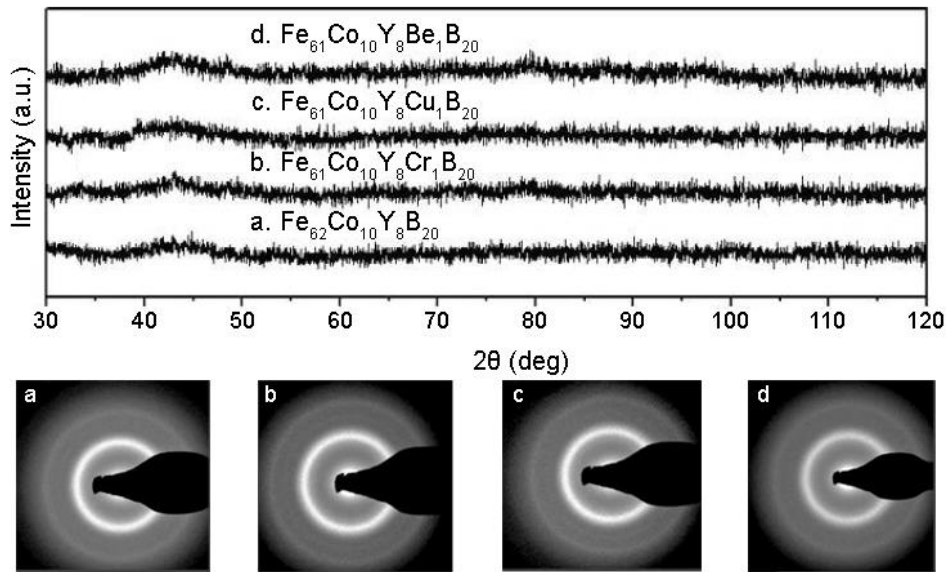


Fig. 1.4 X-ray diffraction patterns and electronograms of four alloys studied by K. Gruszka, before annealing process <sup>[7]</sup>.

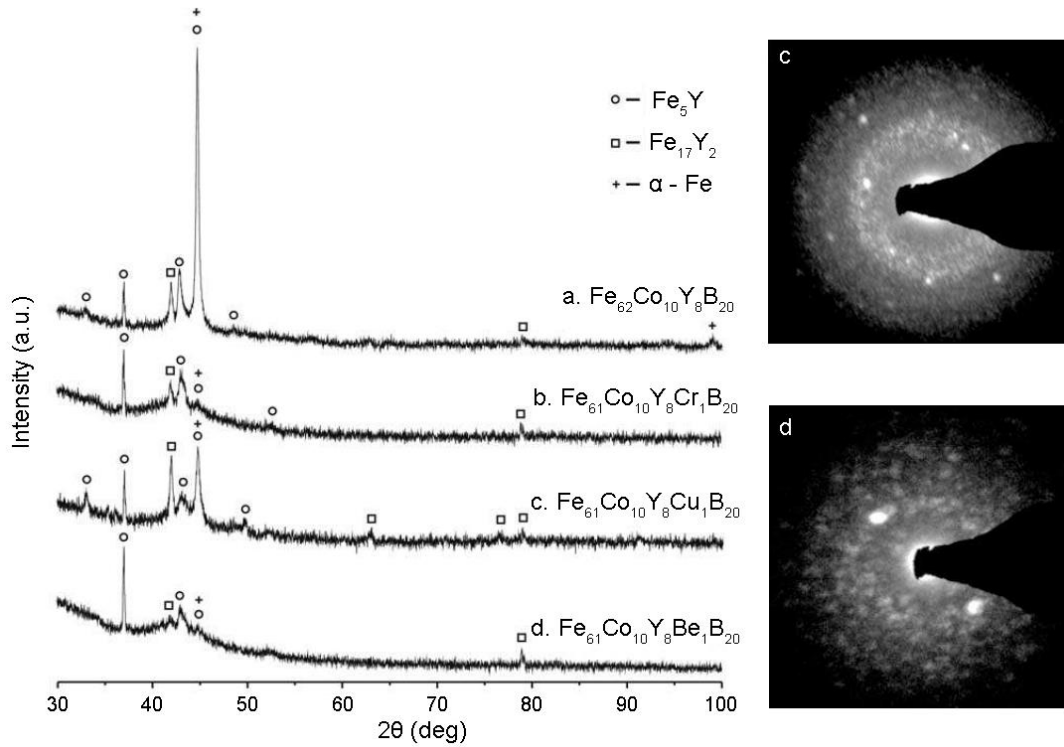


Fig. 1.5 X-ray diffraction patterns and electronograms of four alloys studied by K. Gruszka, after annealing process [7].

It is said that most methods of producing stronger materials are based on controlling defects (such as dislocations) to impede their motion [63]. But such methods have their limitations when it comes to single-phase nanocrystalline alloys and single-phase metallic glasses because of the reverse Hall-Petch effect and shear-band formation, respectively [63-67]. A magnesium-based ‘supra-nanometre-sized dual-phase glass-crystal’ material comprising  $\text{MgCu}_2$  grains of around 6 nm in diameter, uniformly embedded in Mg-enriched amorphous shells which are around 2 nm thick was fabricated by magnetron sputtering technique. This material has a near-ideal strength of 3.3 GPa and a low Young’s modulus of 65 GP.

Strategies for developing materials with excellent dual mechanical properties of high strength and high ductility are sorely needed by scientists [68]. Despite the ultrahigh strength of nanostructured materials and bulk metallic glasses, low ductility is a big

obstacle for practical applications, especially in bulk forms. By adopting nanocrystalline phases, it provides an efficient way to improve the ductility of metallic glass materials and is important for future development of high-strength ductile material.

### 1.2 Rapid solidification techniques in producing metallic glasses

Metallic glasses have been produced by rapidly solidifying metallic melts at cooling rates of about  $10^6 \text{ K}\cdot\text{s}^{-1}$  more than half a century ago. This early excitement of being able to produce metallic materials in a glassy state with excellent mechanical, chemical, and magnetic properties, led to the development of a variety of techniques. And metallic glasses in different sizes and shapes (ribbons, wires, powders, etc.) were able to be produced. After that, commercial requirements of large-size sheets for different applications resulted in the development of the planar flow casting method, wherein rapidly solidified sheets of at least 30 cm in width could be produced <sup>[2]</sup>. It is said that once the potential of a material for any certain application was recognized, a scaling-up method was needed to deploy it commercially <sup>[69]</sup>.

#### 1.2.1 Rapid solidification apparatuses

As illustrated in Fig. 1.6 <sup>[69]</sup>, amorphization techniques are basically divided into two groups. One group is energy (heat) has to be rapidly extracted from the gaseous or liquid state <sup>[26, 28, 45, 53, 70]</sup> during amorphization processes (Fig. 1.6a). The other group is energy has to be added to the solid system (crystal) <sup>[71-75]</sup> to attain amorphous state (Fig. 1.6b). In the latter case, energy is provided to the crystal in the form of chemical reactions (solid-state amorphization <sup>[71]</sup>), radiation (amorphization by high-energy neutrons, protons, heavy ions or electrons <sup>[72]</sup>), pressure (pressure-induced amorphization <sup>[73]</sup>), deformation and cold welding (mechanical milling <sup>[74]</sup>), or shear (severe plastic deformation <sup>[75]</sup>). As the term “glass” is restricted to an amorphous

material produced via cooling from the liquid state, in this thesis we put our focus on the rapid solidification techniques from liquid (and more rarely from gaseous) state.

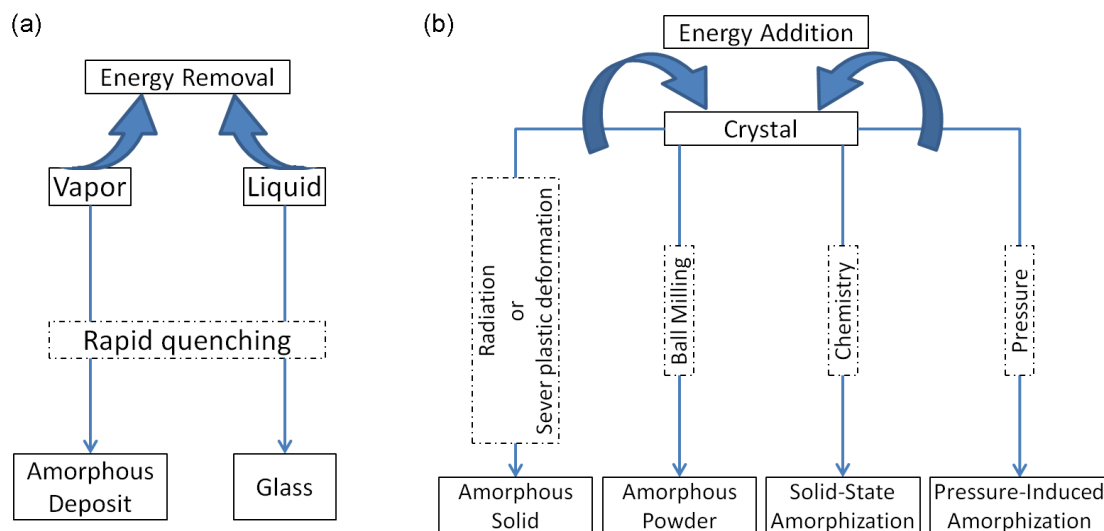


Fig. 1.6 Schematic diagrams representing the various amorphization techniques: (a) energy is extracted from a vapor or liquid phase; (b) energy has to be added to the system <sup>[69]</sup>.

Through the liquid to solid transition, rapid solidification with very high cooling rates was achieved by Pol Duwez. And it was found that high velocity impact of tiny droplets onto a chill substrate could achieve some novel metastable effects. These effects included retention of a single phase f.c.c. structure in an Ag-Cu alloy <sup>[76]</sup> that was two phases under equilibrium conditions, formation of a missing Hume-Rothery phase in an Ag-Ge alloy <sup>[77]</sup> and formation of a metallic glass in an Au-Si system <sup>[26]</sup>. New possibilities were opened up in 1960s followed the remarkable findings published by Duwez in 1960, and various improvements to the Duwez ‘gun’ technique of rapid quenching from the melt were generated <sup>[29]</sup>.

Duwez decided in 1959 that the most favorable conditions for achieving rapid cooling from the melt required the rapid creation of a thin layer of melt in intimate and effective contact with a solid of good thermal conductivity. He tried two versions, the

gun and the piston-and-anvil apparatus, as shown in Fig. 1.7 and Fig. 1.8, respectively.

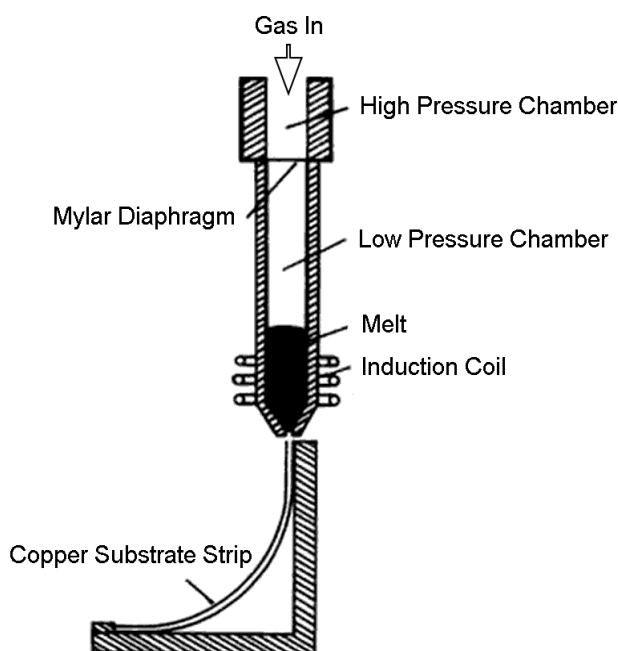


Fig. 1.7 Gun technique of Duwez used for rapid solidification of melts.

In the gun, a high-pressure reservoir of inert gas is built up above a Mylar diaphragm, and when the compressed gas finally ruptures, a shock wave forms and breaks up the small melt drop into minute droplets which are propelled rapidly onto a polished copper substrate strip. It was possible to achieve cooling rates of  $\sim 10^6$  K/s. The tiny flakes thus generated are ideal for X-ray diffraction and (as was found a little later) for TEM. In the piston-and-anvil device, later modified into a two-piston variant, a falling melt drop breaks a light beam and this releases a pneumatically operated piston that squashes the falling drop against the anvil piston, between two copper sheets (Fig. 1.8). This generates larger and thicker foils at a cooling rate of  $\sim 10^6$  K/s, useful when physical properties such as resistivity are to be measured <sup>[29, 69]</sup>.

It should be mentioned here that, at about the same time as Duwez's first papers in the field, two Russians, Miroshnichenko and Salli <sup>[78]</sup>, quite independently published an account of a variant of the Duwez gun. However, there has been very little follow-up

from the Soviet Union since then.

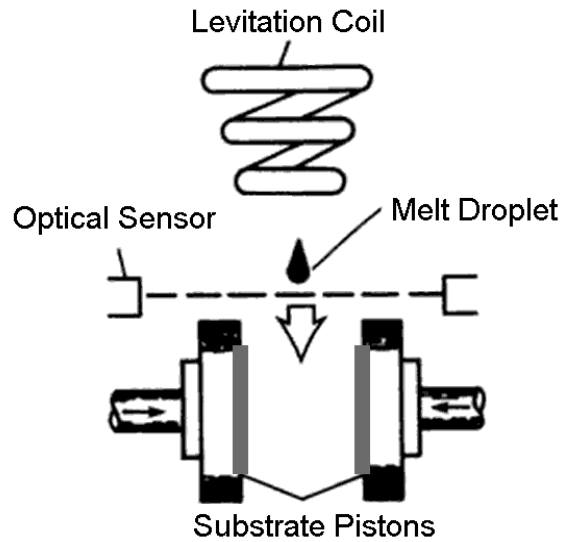


Fig. 1.8 Illustration of Piston-and-Anvil apparatus.

In the 1970s<sup>[79-81]</sup>, when Fe-based metallic glasses with improved soft-magnetic properties were discovered, continuous casting or melt spinning methods gained momentum in response to the requirement in commercial adoptions. These techniques facilitated the production of metallic ribbons cast onto a rotating copper wheel, as is shown in Fig. 1.9.

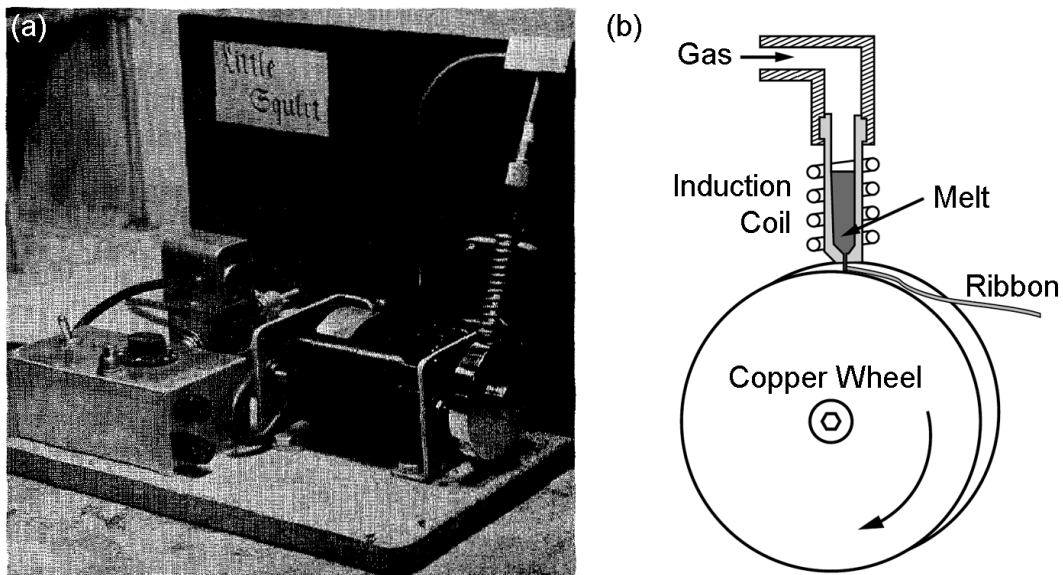


Fig. 1.9 Melt spinning Technique: (a) an apparatus used in making amorphous ribbons<sup>[79]</sup>; (b) schematic illustration of melt spinner<sup>[69]</sup>.

## Chapter 1 Introduction

The key development that permitted single-roller melt spinning to become a major industrial production technique was its conversion into the process which has come to be known as “planar flow casting”. The Pond-Maddin-Masumoto version <sup>[82]</sup> of single-roller melt spinning did not permit wide sheets to be made; the width limit was only a few millimeters. The new process, patented by Narasimhan <sup>[81]</sup>, involves a jet orifice held very close to the rotating wheel so that the resultant melt puddle is physically constrained between the wheel and the lips of the nozzle. With this geometry it is possible to use nozzles in the form of long slits and hence to make wide sheet, more than simply a few centimeters across, of high uniformity in dimensions and properties. Relations between processing parameters and ribbon quality and dimensions have been discussed by some researchers in recent years <sup>[83-86]</sup>, however, only a small fraction of the metallic glasses have so far been commercially deployed mainly due to the difficulty in obtaining good quality in such thin products. For applications in transformer cores, metallic glasses such as Metglas® Alloy 2605SA1 can reduce transformation losses by 70% compared to crystalline iron cores <sup>[69]</sup>.

With the development of complex multicomponent metallic glasses with very low critical cooling rate in the early 1990s, it is possible to quench bulk metallic glass samples in large copper molds. There are two basic techniques for forcing the liquid into a mold: (1) Using an inert-gas pressure difference (via inert-gas pressure injection or suction casting); (2) Piston injection, where a solid piston shoots the melt into a copper mold. These systems have so far mainly been used in configurations similar to that of Fig. 1.10 and Fig. 1.11, where the material is kept in either a quartz or boron-nitride crucible during heating, before being cast into the mold via application of a pressure difference <sup>[69]</sup>. Table 1.3 shows a simple list of the rapid solidification techniques in producing metallic glasses.



## Chapter 1 Introduction

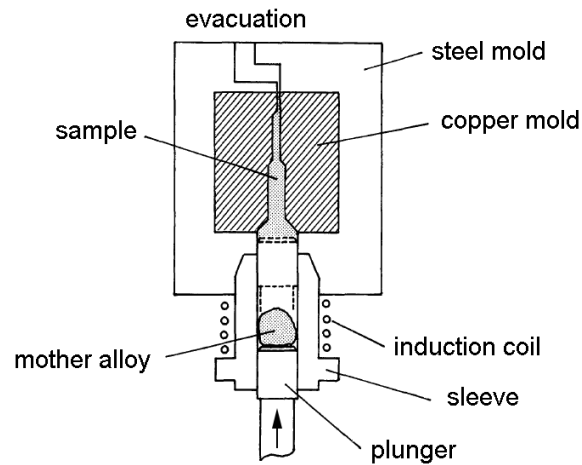


Fig. 1.10 Schematic illustration of a high-pressure die casting equipment <sup>[87]</sup>.

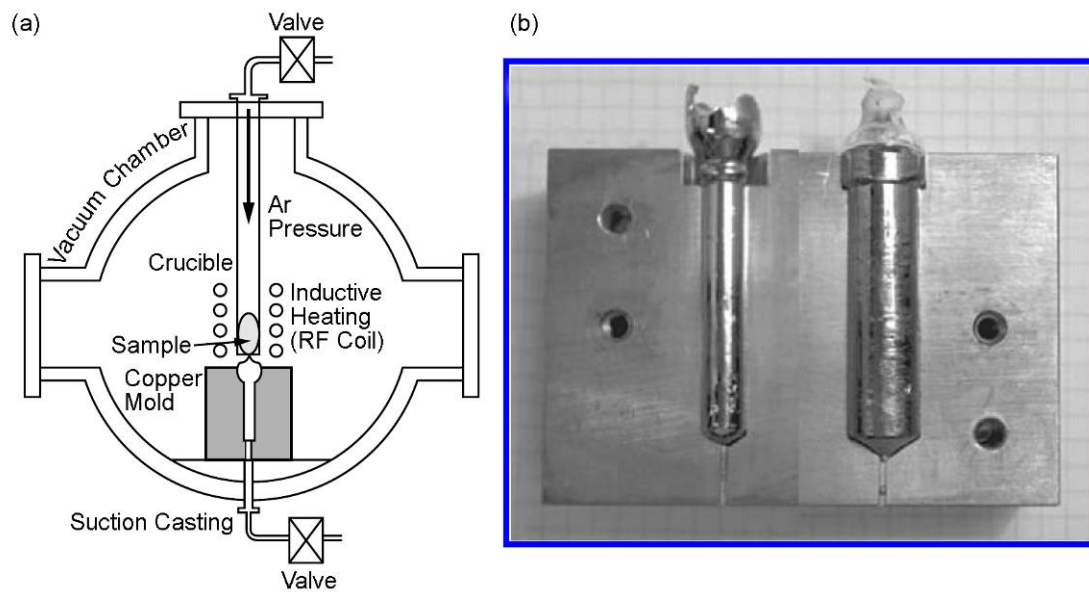


Fig. 1.11 (a) Schematic illustration of copper mold casting, samples are inductively heated and cast by either suction or pressure injection; (b) Copper mold with cast Zr-based bulk metallic glass samples of diameters 5 and 10 mm <sup>[69]</sup>.

Table 1.3 Rapid solidification techniques in producing metallic glasses.

Year	Rapid solidification technique	Cooling rates	Production size	Ref.
1960s	Gun quenching	$\sim 10^6$ K/s	Thin foil, $\phi$ 1~4 cm,	[69]
↓	Splat quenching	$\sim 10^6$ K/s	Thickness of up to 50 $\mu$ m	[69]
1970s	Melt spinning	$\sim 10^6$ K/s	0.05~0.5mm width,	1969 <sup>[82]</sup>

## Chapter 1 Introduction

Year	Rapid solidification technique	Cooling rates	Production size	Ref.
↓			15~50 $\mu\text{m}$ thickness	
			Thickness of 10~40 $\mu\text{m}$ , Width/thickness of 15~55 Mass/length of 0.05~0.24 mg/mm	1976 <sup>[79]</sup>
			Few centimeters width	1979 <sup>[81]</sup>
1990s	Copper mold casting	$10^2 \sim \text{K/s}$	Bulk	<sup>[87]</sup>

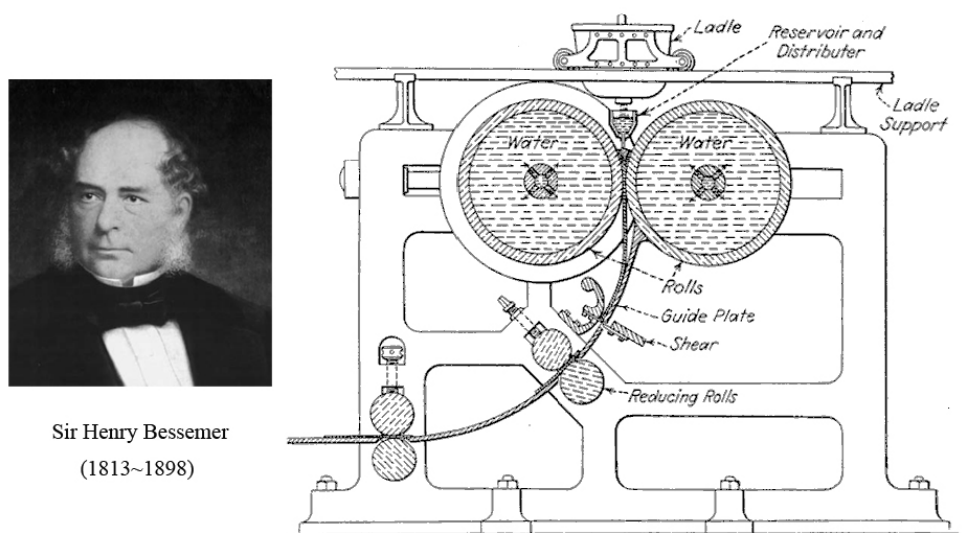
Apart from these synthesis methods, various processing methods for discovering new bulk metallic glass compositions have also been developed in recent years. The high-temperature centrifugation method <sup>[88, 89]</sup>, for example, can in multicomponent alloys physically isolate deep eutectic compositions, which have a high potential for good glass-forming ability <sup>[69]</sup>.

### 1.2.2 Rapid solidification of twin roll strip casting technique

The most significant milestone in the rapid solidification processing (RSP) field was the development of the chill block melt spinning technique in the 1970s and several of its variants (a rapid cooling technique that can routinely quench liquid alloys as 10~50  $\mu\text{m}$  thick ribbons at cooling rates of  $10^3 \sim 10^6 \text{ K/s}$  by impinging a melt stream on a spinning copper wheel <sup>[90]</sup>). The main advantages of the melt-spinning technique are: (1) it will be possible to produce ribbons of uniform cross section, (2) its process parameters have been optimized, and (3) melt spinners are commercially available <sup>[2]</sup>.

In the melt spinning process, conditions between the roll-contact surface and free surface of ribbon are different (e.g., asymmetric heat extraction), and these will affect the final ribbon quality <sup>[84, 91, 92]</sup>. Another shortcoming is that the thickness cannot be

increased much by any of the known melt-spinning methods (20~50  $\mu\text{m}$  in common) <sup>[2]</sup>. In contrast, metallic ribbons or strips produced by twin roll casting technique are casted and hot rolled at the same time and a better surface quality is expected. The concept of continuous casting in a single stage dates back to Bessemer, in 1846, who envisioned using a twin roll technique to cast steel strips <sup>[29]</sup>, but technical realization was more than a century later. A sketch of Bessemer's twin roll caster is shown in Fig. 1.12.



Sir Henry Bessemer  
(1813~1898)

Fig. 1.12 Bessemer's twin roll caster.

In 1970, after Duwez's seminal discoveries, a twin roll casting (TRC) technique for preparing uniform films of metastable phases was taken out by Chen and Miller <sup>[93]</sup>. And to date, this technique in producing metallic glass ribbons is almost still limited to laboratory scale studies <sup>[94-100]</sup>. It turns out that TRC is an available process for producing amorphous alloy sheets with a wide range of cooling rates. Nevertheless, most of the studies so far are based on horizontal type twin-roll casters. Studies on TRC technique for produce metallic glasses are list in Table 1.4 <sup>[101]</sup>.

Table 1.4 Papers on the research of TRC of metallic glasses.

Year	Type	Cooling rate (K/s)	Speed (rpm)	Ref.
1970	Vertical	$10^5$	100~5000	[93]
1974	Vertical	$10^5$	---	[94]

## Chapter 1 Introduction

Year	Type	Cooling rate (K/s)	Speed (rpm)	Ref.
2005	Horizontal	$10^2 \sim 10^3$	1, 3	[95, 96, 102]
2007	Horizontal	---	0.75 m/s	[98]
2010	Horizontal	---	1.7 m/min	[100]
2013	Vertical	$1 \sim 10^3$	---	[99]

The apparatus proposed by Chen and Miller in 1970 is shown in Fig. 1.13. The rollers are 5 cm diam  $\times$  5 cm width and held together with pressure  $p$  which ranges from 20 to 90 kg. Rotation speed of the rollers can be varied from 100 to 5000 rpm (15.7~785.4 m/min). Amorphous solids could be formed in ribbon or oval shapes ( $5 \times 50$  mm<sup>2</sup> with thickness 40~100  $\mu$ m,  $20 \times 20$  mm<sup>2</sup> with thickness 10  $\mu$ m). The thickness of the film decreased with increasing rotation speed and pressure on the rollers [93]. Quenching rate of the apparatus is in the order of  $10^5$  K/s.

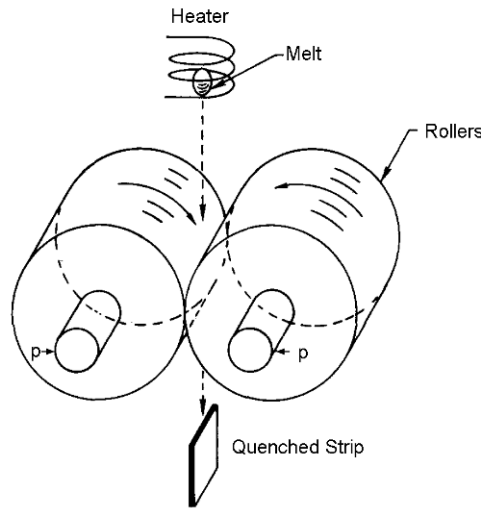


Fig. 1.13 Schematic drawing of the quenching apparatus proposed by Chen and Miller [93].

Assuming the melt has solidified at the time of the exit from the rollers, they evaluated the quenching rate  $\dot{T}$  with the following equation:

$$\dot{T} = \Delta T / \Delta t \approx (T_i - T_g) v / d \quad (1-2)$$

where  $T_i$  and  $T_g$  are, respectively, the initial and the glass temperature of the melt, and

## Chapter 1 Introduction

$\Delta t$  is the time duration of contact between the melt and the rollers,  $v$  is the linear velocity of the roller and  $d$  is the distance traveled by the melt during solidification. This apparatus was used for the preparation of uniform specimens of metastable phases for studies of the structure and properties of metastable materials including amorphous and supersaturated alloys <sup>[93]</sup>.

Referring the twin roller device shown in Chen and Miller's work, Suzuki designed an apparatus in 1974 and 20 binary oxides were obtained as non-crystalline solid (NCS) for the first time by using their technique <sup>[94]</sup>. The vertical type caster has two steel rollers with both diameters of 55 mm and 20 mm in width. The foils made by the caster were found have thicknesses of 1~40  $\mu\text{m}$ .

In 1981, Miyazawa and Szekely published a paper on simulation of the twin roll casting technique <sup>[103]</sup>. A mathematical model was developed to represent the heat and flow phenomena and pressure distribution in the solid phase. In the calculations, property values of aluminum were used. They considered roll spacing, feed rate and angular velocity of the rolls as main variables and got a conclusion that for a given material there exists only a narrow range of these parameters that affords stable operation. It also mentioned that the rapid solidification process has the ability of quenching metals or alloys into microcrystalline or amorphous structure.

In the 2000s, a group of researchers from Korea paid attention to studying of twin roll casting technique in metallic glasses <sup>[95-97, 104]</sup>. Based on the simulation of solidification behavior and actual twin-roll strip casting results, the optimum casting condition was found out to be that alloys are in supercooled liquid state at roll nip area rather than fully amorphized state. The horizontal twin roll caster they used has a roll diameter of 200 mm, roll gap was set as 2 mm, roll speed was 1 rpm and 3 rpm. Vit-1 alloy ( $\text{Zr}_{41.2}\text{Ti}_{13.8}\text{Cu}_{12.5}\text{Ni}_{10.0}\text{Be}_{22.5}$ , critical cooling rate of  $\sim 1$  K/s) was successfully

## Chapter 1 Introduction

casted into amorphous state with casting speed of 3 rpm. Microstructure of the sheet was amorphous matrix with a few polygonal crystalline particles. They got a conclusion that the twin-roll strip casting can be applied for the fabrication of bulk amorphous alloy sheets with a wide range of critical cooling rates <sup>[95]</sup>.

There two papers published in 2007 which were both about twin roll casting of Fe-base glassy alloys <sup>[97, 98]</sup>. Some of the details are listed in Table 1.5.

Table 1.5 Twin roll casting of Fe-base glassy alloys.

	Nack J. Kim group <sup>[97]</sup>	Akihisa Inoue group <sup>[98]</sup>
Caster type	Horizontal	Horizontal
Roller diameter (mm)	200	Upper : 100
		Lower : 400
Roller width (mm)	---	200
Plate size	Thickness of 1 mm	Width of 70 mm, thickness of 0.5 mm, length of 150 mm
Rotating speed (m/min)	1.9 (3rpm)	45
Roll gap (mm)	1	---
Materials	Fe <sub>63</sub> B <sub>15</sub> Zr <sub>8</sub> Co <sub>6</sub> Mo <sub>7</sub> Al <sub>1</sub>	Fe <sub>36</sub> Co <sub>36</sub> B <sub>20</sub> Si <sub>4</sub> Nb <sub>4</sub>
Microstructure	Amorphous structure with some dendritic crystalline phase.	Small crystalline grains dispersed in the glassy matrix. Grain size is evaluated to be 20~100 μm and the crystalline grains were observed mainly in the center of the plate.
Crystalline grains	α-Fe phase	α-Fe phase
Conclusion	Possibility of continuously producing glassy plate.	

In 2010 Daniel and coworkers fabricated magnesium sheet (Mg<sub>60</sub>Cu<sub>29</sub>Gd<sub>11</sub>) in glassy state by twin roll casting technique <sup>[100]</sup> with discussing the influences of roll speed. Amorphous sheet with thickness of 3 mm and width of 50 mm were produced by a horizontal twin roll caster at CSIRO. They found that the structure of the as-cast sheet changed from being crystalline to fully amorphous and then back to crystalline with the increasing roll speed. A malleable sheet with no surface defects could be produced

## Chapter 1 Introduction

through careful selection of the casting speed and with which the exit temperature of the sheet remains within the supercooled liquid region. This conclusion is the same as which is mentioned in reference <sup>[95]</sup>. This work shows that twin roll sheet casting is a viable process for the production of magnesium-based bulk glassy sheet in a continuous manner and on an industrial scale <sup>[100]</sup>.

A patent about twin roll casting of bulk metallic glasses was published in 2013. It is a vertical type caster and composited in an inert environment. It may produce thin, semi-continuous or continuous sheets of bulk metallic glasses (BMGs) and bulk metallic glass matrix composites (BMGMCs) with thickness between approximately 0.1 mm and 10 mm that are largely, or full, free of oxygen or other contamination caused by environmental casting conditions <sup>[99]</sup>. As far as the author concerned, despite how many advantages of a rapid solidification technique possesses, when it comes to vacuum, maybe it is no longer suitable for industrial application consider the economic aspect.

### 1.3 Material selection and process determination

It has been shown that different processing techniques generate different atomic structure and free volume in metallic glasses, and that these differences are very sensitive to the cooling rates with which they are produced <sup>[69]</sup>. This in turn can have a drastic effect on mechanical and other physical properties. Metallic glasses get crystallized during annealing at high temperatures and lose all the beneficial effects. Thus, during the 1980's, there was a resurgence of activity in the area of rapidly solidified microcrystalline alloys (especially those based on light metals) for possible application in the aerospace industry. The discovery of quasicrystalline phases (Shechtman et al., 1984 <sup>[10]</sup>) has given a short-lived added impetus to the field of metallic glasses. Recent development of new multicomponent alloys incorporating crystalline particles within an amorphous matrix has shown a promise for improved

plasticity<sup>[105, 106]</sup>.

### 1.3.1 Material selection

Magnesium is 36% lighter per unit volume than aluminum and 78% lighter than iron. It is the lightest of all the engineering metals and the third most abundant structural metal following steel, aluminum. When alloyed, magnesium has the highest strength-to-weight ratio of all the structural metals. Due to the ease of recycling, magnesium has received global attention from the standpoint of environmental preservation. More and more weight-saving and energy-saving applications select magnesium as structural and non-structural materials by means of their high specific strength, high damping and good electromagnetic shield abilities. Fig. 1.14 shows some automotive components made from magnesium alloy. Due to their excellent properties of heat dissipation, electromagnetic shielding and “metal feeling” sense comparing with plastics, magnesium alloys are also applied to the 3C market. The products cover computers, communications and consumer electronics such as notebook PCs, mobile phones, mini-disc players, cameras and other handheld devices<sup>[107]</sup>. Fig. 1.15 shows some applications of magnesium alloy on 3C products. In this work, we adopted magnesium alloys as the object considering the viewpoints stated above.



Fig. 1.14 Automotive components made from magnesium alloys.



## Chapter 1 Introduction



Fig. 1.15 Magnesium alloys applied to 3C products.

Magnesium is most commonly alloyed with other metals when being used in structural applications. Table 1.6 <sup>[108]</sup> displays a number of commonly used alloying elements accompanied with their effects upon the resulting metal. (Reference International Magnesium Association: [http://intlmg.site-ym.com/?page=design\\_mag\\_all\\_ima](http://intlmg.site-ym.com/?page=design_mag_all_ima))

Table 1.6 General effects of alloying elements on magnesium (I/M: ingot metallurgy).

Alloying element	Melting and casting behavior	Mechanical and technological properties	Corrosion behavior I/M produced
Ag		Improves elevated temperature tensile and creep properties in the presence of rare earths	Detrimental influence on corrosion behavior
Al	Improves castability, tendency to microporosity; average alloy contains about 2~9 wt.% of aluminum and can be heat treated with > 6 wt.%	Solid solution hardener, precipitation hardening at low temperature (< 393 K); increases hardness, strength and castability while only increasing density minimally; increased amount of aluminum decreases the ductility of the alloy.	Minor influence
Be	Significantly reduces oxidation of melt surface at very low concentrations (< 30 ppm); lead to coarse	Can be a carcinogenic material and is being rejected by some companies for use.	

## Chapter 1 Introduction

Alloying element	Melting and casting behavior	Mechanical and technological properties	Corrosion behavior I/M produced
	grains; included only in very small quantities;		
Ca	Effective grain refining effect, slight suppression of oxidation of the molten metal	Improves thermal and mechanical properties as well as assists in grain refinement and creep resistance; allows for better rollability of sheet metal; additions exceeding .3 wt.%, increases the risk of cracking during welding; reduces surface tension.	Detrimental influence on corrosion behavior
Cu	System with easily forming metallic glasses; improves castability;	Assists in increasing both room and high temperature strength; negatively impacts ductility.	Detrimental influence on corrosion behavior, limitation necessary
Fe	Magnesium hardly reacts with mild steel crucibles		Detrimental influence on corrosion behavior, limitation necessary
Li	Increases evaporation and burning behavior, melting only in protected and sealed furnaces	Solid solution hardener at ambient temperatures, reduces density, enhances ductility	Decreases corrosion properties strongly, coating to protect from humidity is necessary
Mn	Control of Fe content by precipitating Fe-Mn compound, refinement of precipitates	Increases creep resistivity; reduces the adverse effects of iron, usually present in .2~4 wt.%	Improves corrosion behavior due to iron control effect; increases saltwater corrosion resistance within some aluminum containing alloys.
Ni	System with easily forming metallic glasses	Increases both yield and ultimate strength at room temperature; negatively impacts ductility.	Detrimental influence on corrosion behavior, limitation necessary

## Chapter 1 Introduction

Alloying element	Melting and casting behavior	Mechanical and technological properties	Corrosion behavior I/M produced
Rare earths	Improve castability, reduce microporosity	Solid solution and precipitation hardening at ambient and elevated temperatures; improve elevated temperature tensile and creep properties; allows lower casting porosity and weld cracking in processing.	Improve corrosion behavior
Ce		Increases plastic deformation capability, magnesium elongation, and work hardening rates; reduces yield strength.	Improves corrosion resistance
Y	Grain refining effect	Improves elevated temperature tensile and creep properties	Improve corrosion behavior
Si	Decreases castability, forms stable silicide compounds with many other alloying elements, compatible with Al, Zn and Ag, weak grain refiner; can increase molten alloys' fluidity; only used in pressure die casting	Improves elevated temperature properties, especially creep resistance.	Detrimental influence on corrosion behavior
Sr		Used in conjunction with other elements to enhance creep performance	
Sn		When used with aluminum it improves ductility, and reduces tendency to crack during processing.	
Th	Suppresses microporosity	Improves elevated	Improve corrosion

## Chapter 1 Introduction

Alloying element	Melting and casting behavior	Mechanical and technological properties	Corrosion behavior I/M produced
		temperature tensile and creep properties, improves ductility, most efficient alloying element	behavior
Zn	Second most commonly used alloying metal with magnesium; increase fluidity of the melt, weak grain refiner, tendency to microporosity;	Precipitation hardening, improves strength at ambient temperature, tendency to brittleness and hot shortness unless Zr refined; additions of 2 wt.% or greater tend to be prone to hot cracking	Minor influence, when added to magnesium alloys with nickel and iron impurities, it can improve corrosion resistance; sufficient Zn content compensates for the detrimental effect of Cu
Zr	Most effective grain refiner, incompatible with Si, Al, and Mn, removes Fe, Al, and Si from the melt	Improves ambient temperature tensile properties slightly	

There are two basic magnesium alloy systems, Mg-Al alloy and Mg-Zr alloy, depending on addition alloy elements. It also can be divided into casting and wrought alloys based on processing methods. The addition of aluminum and zinc generally leads to higher room-temperature strength. Zirconium additions produce very fine grain sizes in certain magnesium alloys, predominantly those alloys not containing aluminium, because aluminum and zirconium can readily form stable intermetallic phases which are unfortunately ineffective as nucleants for magnesium grains. AZ91 alloy is the most favored casting alloy, being used in approximately 90 percent of all magnesium cast products. However, the range of applications for this alloy is limited by the low strength and poor creep resistance at temperatures above 150 °C. AZ31B is most widely used wrought alloy for sheet and plate and is available in several grades and tempers.

## Chapter 1 Introduction

Rare earth addition can improve creep strength at elevated temperatures. It was reported that adding RE elements can improve the properties of Mg-Al alloys at elevated temperature <sup>[109, 110]</sup>. Due to the formation of highly thermally stable  $\text{Al}_{11}\text{RE}_3$  and  $\text{Al}_2\text{RE}$  intermetallic phases,  $\text{Mg}_{17}\text{Al}_{12}$  phase is suppressed and AE42 (Mg-4Al-2RE, wt.%) exhibits major improvement in creep resistance. Jinghuai Zhang investigated the effect of Ce on high-pressure die-cast Mg-4Al-based alloy <sup>[109]</sup>. It was found that with addition of Ce, the grains of Mg-4Al-0.3Mg alloy are refined and corrosion resistance is improved. Al and Ce/La could form compact corrosion product film during the corrosion of Mg-4Al-4Ce/La-0.4Mn alloy and it exhibits good corrosion resistance <sup>[111]</sup>.

RE in magnesium alloys has the characteristic of so-called “scavenger effect” <sup>[112]</sup>. Impurity elements could form intermetallic compounds with RE and they are less cathodic. Simultaneously, the formation of  $\beta$  ( $\text{Mg}_{17}\text{Al}_{12}$ ) phase is restrained by RE. The micro-galvanic couples could be depressed which leading to an improvement of corrosion resistance of magnesium alloys. In the investigation of effect of rare earth element Ce and La on corrosion behavior of AM60 <sup>[112]</sup>, it was found that the optimal content of Ce and La was 0.82 wt.% and 0.59 wt.%, respectively.

### 1.3.2 Process determination

Mg alloys produced by traditional ingot metallurgy (I/M) processing exhibit lower strength, ductility, creep resistance and corrosion resistance <sup>[113]</sup>. Recent researches have revealed that grain refinement substantially improves the deformability of magnesium alloys by introducing new deformation mechanisms. In the extreme case, nanostructured magnesium alloys were found to exhibit superplasticity and the deformation mechanism responsible for such superplasticity is Grain Boundary Sliding (GBS). J. Koike et al. found that in fine grained (7  $\mu\text{m}$ ) AZ31 alloy, dislocation cross slip to non-basal planes occurred very easily in the entire grain region <sup>[114]</sup>. They also

## Chapter 1 Introduction

found that GBS can occur at room temperature and its contribution to the total strain was 8% when the tensile test was performed at a strain rate of  $10^{-3} \text{ s}^{-1}$ . As a consequence of introducing new deformation mechanisms, fine grained AZ31 alloy was found to exhibit 45% elongation at room temperature. This fact has raised a lot of interest in achieving grain refinement in magnesium alloys through various methods.

Usually grain refinement can be achieved through the addition of alloying elements (e.g., zirconium, calcium, rare earth elements) due to their grain growth restriction effects during solidification process <sup>[115-117]</sup>. Another grain refinement approach is processing control method including controlling parameters of solidification and consequent thermomechanical processing, such as mechanical and supersonic vibrations <sup>[118-120]</sup>, electromagnetic stirring <sup>[121]</sup>, superheating treatment <sup>[122]</sup>, FeCl<sub>3</sub> addition <sup>[123]</sup>, carbon inoculation <sup>[124]</sup>, severe plastic deformation (SPD) <sup>[125-127]</sup> and rapid solidification <sup>[128, 129]</sup>. Grain refinement also can be achieved by low temperature rolling process, in which dynamic recrystallization was promoted and grain growth was suppressed.

Sheet metal is one of the fundamental forms in industry and share more than 80% of metals and alloys products <sup>[95]</sup>. Application of magnesium alloy sheets with competitive cost is considered a real breakthrough of wrought magnesium. However, conventional magnesium sheet rolling process is high cost and low productivity, especially in the final rolling passes. In order to obtain crack-free surface, repeated rolling and reheating are necessary. It results in the fact that less than one percent of magnesium alloys were provided in the form of sheet or strip coil. Developing new forming process for magnesium sheets with excellent properties is expected to lower their cost and extend their applications.

It has been shown that twin-roll strip casting can produce high quality Mg sheet products which have equivalent mechanical properties to conventional ingot casting Mg

## Chapter 1 Introduction

alloys. Twin-roll strip casting process combines casting and hot rolling into a single step, having an advantage of one-step processing of flat rolled products. Magnesium sheet production R&D has been attracted global attention over the past years (CSIRO Australia, ThyssenKrupp Germany, POSCO Korea, Gonda Metal Industry and MITSUBISHI ALUMINUM Japan, Luoyang Copper Group Co. Ltd. and Wenxi Yinguang Magnesium Group Co. Ltd. China, CANMET Energy Technology Centre Canada, etc.). Generally, most of their casting processes are focused at producing strip width in the 500-700 mm, thickness in the 4~10 mm and casting speed at 1~6 m/min range by horizontal type twin roll casting process. For example, in Australia, CSIRO has developed a horizontal twin roll casting technology which is used extensively in the aluminum industry since 2000 <sup>[130]</sup>. The CSIRO Twin Roll Caster aims to produce as-cast magnesium sheet in commercial quantities using patented CSRIO systems which were specifically developed for handling molten magnesium. It has shown out that their technology is economically efficient and suitable for semi-continuous production of 100~200 kg coils of typically 3 mm thick magnesium sheet. As we mentioned in *Section 1.2*, the caster in CSRIO was also used for producing Mg-based metallic glasses in 2010 <sup>[100]</sup>.

Besides being such a cost-effective process, twin-roll strip casting also has beneficial effects on microstructure such as reducing segregation and grain size with a consequent improvement of mechanical properties and corrosion resistance. These are due to a relatively high solidification rate ranging from  $10^2$  to  $10^3$  K/s, which is located between those of ingot casting and rapid solidification techniques. It is well known that the quite high solidification rate of rapid solidification process enables the utilization of dispersion strengthening by alloying elements which have limited solubilities in Mg, which are usually avoided in ingot casting since these elements form coarse intermetallic particles at a low solidification rate. It is expected that such dispersion

## Chapter 1 Introduction

strengthening can also be utilized in twin-roll strip casting which is a semi-rapid solidification processing <sup>[131]</sup>. Because the influence of gravity, it shows that the casting speed of vertical type twin roll casting (VTRC) is higher than horizontal-type twin-roll casting (HTRC), and the heat transmission of the former is more effective <sup>[132-134]</sup>. In this study, twin roll strip casting technique was adopted as the processing method.

### 1.4 Purpose of this thesis

The term lightweight has been proposed for many years and it is still a hot topic in modern society, magnesium and its alloys as lightweight material are well accepted for many applications in automobile and aerospace industries. However, the applications of Mg alloys are very limited because of the restricted plasticity of Mg (owing to the hexagonal closed-packed crystal structure which possesses few slip systems) and their poor corrosion resistance (do not form a protective oxide film) comparing with other metals <sup>[8, 135]</sup>. In this work, we focused on developing a new kind of Mg-based alloy with proper mechanical performance and good corrosion resistance. Considering its application, we proposed a cost-competitive method to produce the new material in sheet-form. It is considered as an efficient mass-production technique.

Despite the superior properties (e.g., ultrahigh strength, excellent soft magnetic properties) of bulk metallic glasses to crystalline alloys, low ductility, making them prone to catastrophic failure in load-bearing applications, is a big obstacle for practical applications. Another drawback is the quit limited size and shape of bulk amorphous alloy products. This is because the commercially available processes for their fabrication are die-casting and melt spinning. Beside these, fairly large amounts of expensive alloying elements are required to form amorphous structure in bulk form, such as the Pd-based materials.



## Chapter 1 Introduction

By adopting nanocrystalline <sup>[7, 62, 63]</sup> or quasicrystalline <sup>[106]</sup> phases it provides an efficient way to improve the ductility of metallic glass materials and is important for future development of high-strength ductile material. This technique requires the initial synthesizing of amorphous phases, and the complex process brings two close-coupled reactors, i.e., difficult scale-up and high cost.

Recent development of new multicomponent alloys incorporating crystalline particles within an amorphous matrix has also shown a promise for improved plasticity <sup>[105, 136]</sup>. Only the materials with good glass forming abilities were appropriate and the available alloy systems are limited.

Rapid solidification extends the solid solubility limits, allowing the addition of novel alloying elements in larger contents than traditional ingot casting without gross segregation, and these results in a refinement of microstructures and the formation of new or metastable phases which are beneficial to improvement of product performance. Consider the twin roll strip casting process has a relatively high solidification rate ranging from  $10^2$  to  $10^3$  K/s, this technique is adopted in the current work.

The main target is to propose an effective rapid solidification method with low cost and high productivity to prepare amorphous or amorphous and fine grain mixed materials feasibly and practically. Improved ductility and better corrosion resistance are expected in our materials. The following aspects will be emphasized:

### (I) Novel multi-component magnesium-based alloy design

As Tin has the potential of improve creep resistance and ductility of Mg-Al alloy <sup>[137]</sup>, Indium is used in Mg battery materials <sup>[138, 139]</sup>, AZ31-In-Sn battery material was produced and studied in our work.

## Chapter 1 Introduction

As rare earth (RE) element has a characteristic of so-called “scavenger effect” in magnesium alloys <sup>[112]</sup>, impurity elements could form less cathodic intermetallic compounds with RE, in order to improve the corrosion resistance of the product, Lanthanum and Cerium were adopted in our designment.

### (II) Casting glassy + crystalline Mg-based alloy sheet by vertical twin roll casting technology

Twin roll casting is a rapid solidification process with high temperature gradient combined with thermal flow and rolling deformation in the casting region. Microstructure of as-cast alloy is sensitive to casting conditions, and it greatly affects the mechanical properties. Vertical twin roll casting of magnesium sheet technology was adopted in this research, since higher casting speed and thinner magnesium sheet can be achieved comparing with conventional horizontal twin roll casting process. Fig. 1.16 shows the cooling path by which a liquid may solidify. The pale yellow zone is an interesting transition region that it is easy to form a dual phase (amorphous and crystalline phase) material and the crystalline phase may have very fine grains. We intend to study this zone by rapid solidification of twin roll strip casting technique.

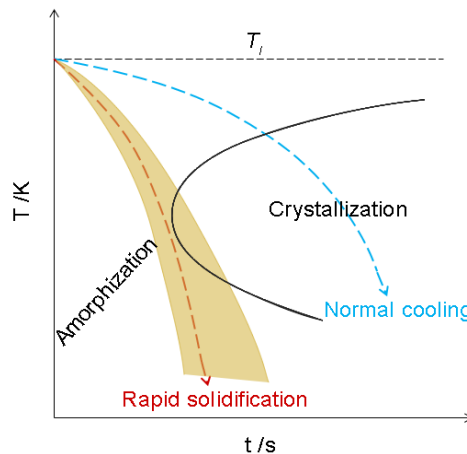


Fig. 1.16 Illustration of cooling path by which a liquid may solidify. A slow cooling rate leads to crystallization (blue curve). A rapid quench leads to amorphization (red curve).

### References

- [1] Inoue A, Hashimoto K. Amorphous and nanocrystalline materials: Preparation, properties, and applications [M]. Springer-Verlag Berlin Heidelberg, 2001.
- [2] Suryanarayana C, Inoue A. Bulk metallic glasses [M]. CRC Press, 2010.
- [3] Chen H S. Glassy metals [J]. Reports on Progress in Physics, 1980, 43(4): 353.
- [4] Beeler Jr J R. OUTLINE OF DEFECT PROPERTIES COMPUTATIONS [M]. Radiation Effects Computer Experiments. Oxford; Elsevier. 1983: 113-159.
- [5] Gleiter H. Nanocrystalline materials [J]. Progress in Materials Science, 1989, 33(4): 223-315.
- [6] Gleiter H. On the structure of grain boundaries in metals [J]. Materials Science and Engineering, 1982, 52(2): 91-131.
- [7] Gruszka K, Nabiałek M, Błoch K, et al. Analysis of the structure (XRD) and microstructure (TEM, SEM, AFM) of bulk amorphous and nanocrystalline alloys based on FeCoB [J]. International Journal of Materials Research, 2015, 106(7): 689-696.
- [8] Xu W, Birbilis N, Sha G, et al. A high-specific-strength and corrosion-resistant magnesium alloy [J]. Nature materials, 2015, 14(12): 1229-1235.
- [9] Holzwarth U, Gibson N. The Scherrer equation versus the 'Debye-Scherrer equation' [J]. Nature Nanotechnology, 2011, 6(9): 534.
- [10] Shechtman D, Blech I, Gratias D, et al. Metallic Phase with Long-Range Orientational Order and No Translational Symmetry [J]. Physical Review Letters, 1984, 53(20): 1951-1953.
- [11] Kelton K F. Quasicrystals: structure and stability [J]. International Materials Reviews, 1993, 38(3): 105-137.
- [12] Inoue A, Takeuchi A. Recent progress in bulk glassy, nanoquasicrystalline and nanocrystalline alloys [J]. Materials Science and Engineering: A, 2004, 375-377(Supplement C): 16-30.
- [13] Dotera T, Bekku S, Zihler P. Bronze-mean hexagonal quasicrystal [J]. Nature materials, 2017, 16(10): 987.
- [14] Nagao K, Inuzuka T, Nishimoto K, et al. Experimental Observation of

- Quasicrystal Growth [J]. *Physical Review Letters*, 2015, 115(7): 075501.
- [15] Verbin M, Zilberberg O, Lahini Y, et al. Topological pumping over a photonic Fibonacci quasicrystal [J]. *Physical Review B*, 2015, 91(6): 064201.
- [16] Turnbull D. Under what conditions can a glass be formed? [J]. *Contemporary Physics*, 1969, 10(5): 473-488.
- [17] Uhlmann D R. Glass formation [J]. *Journal of Non-Crystalline Solids*, 1977, 25(1–3): 42-85.
- [18] Suryanarayana C. Metallic glasses [J]. *Bulletin of Materials Science*, 1984, 6(3): 579-594.
- [19] Greer A L. Metallic glasses...on the threshold [J]. *Materials Today*, 2009, 12(1): 14-22.
- [20] Gleiter H. Nanocrystalline Materials [M]//BUNK W G J. *Advanced Structural and Functional Materials: Proceedings of an International Seminar Organized by Deutsche Forschungsanstalt für Luft- und Raumfahrt (DLR), Köln, June 1991*. Berlin, Heidelberg; Springer Berlin Heidelberg. 1991: 1-37.
- [21] Meyers M A, Mishra A, Benson D J. Mechanical properties of nanocrystalline materials [J]. *Progress in Materials Science*, 2006, 51(4): 427-556.
- [22] Clarke J B, Hastie J W, Kihlberg L H E, et al. Definitions of terms relating to phase transitions of the solid state (IUPAC Recommendations 1994) [M]. *Pure and Applied Chemistry*. 1994: 577.
- [23] Greer A L, Ma E. Bulk Metallic Glasses: At the Cutting Edge of Metals Research [J]. *MRS Bulletin*, 2007, 32(08): 611-619.
- [24] Susanne S. Bulk metallic glasses [J]. *Journal of Physics: Condensed Matter*, 2001, 13(34): 7723.
- [25] Arata E R. High-temperature, ultrahigh-gravity centrifugal processing of metallic melts [D]; Citeseer, 2008.
- [26] JUN. W K, Willens R H, Duwez P. Non-crystalline Structure in Solidified Gold-Silicon Alloys [J]. *Nature*, 1960, 187(4740): 869-870.
- [27] Busch R. The thermophysical properties of bulk metallic glass-forming liquids [J]. *JOM*, 2000, 52(7): 39-42.
- [28] Inoue A. Stabilization of metallic supercooled liquid and bulk amorphous alloys [J]. *Acta Materialia*, 2000, 48(1): 279-306.
- [29] Jones H. A perspective on the development of rapid solidification and

- nonequilibrium processing and its future [J]. *Materials Science and Engineering: A*, 2001, 304–306(1): 11-19.
- [30] Wang W H, Dong C, Shek C H. Bulk metallic glasses [J]. *Materials Science and Engineering: R: Reports*, 2004, 44(2–3): 45-89.
- [31] Miracle D B. The efficient cluster packing model – An atomic structural model for metallic glasses [J]. *Acta Materialia*, 2006, 54(16): 4317-4336.
- [32] Li Y, Poon S J, Shiflet G J, et al. Formation of Bulk Metallic Glasses and Their Composites [J]. *MRS Bulletin*, 2007, 32(08): 624-628.
- [33] Schroers J. Processing of Bulk Metallic Glass [J]. *Advanced Materials*, 2010, 22(14): 1566-1597.
- [34] Aqida S N, Shah L H, Naher S, et al. Rapid Solidification Processing and Bulk Metallic Glass Casting [M]//BATALHA G F, TYNE C J V, YILBAS B. *Comprehensive Materials Processing*. Oxford; Elsevier. 2014: 69-88.
- [35] Davies H A. Chapter 2 - Metallic glass formation [M]//LUBORSKY F E. *Amorphous Metallic Alloys*. Butterworth-Heinemann. 1983: 8-25.
- [36] Duwez P. Metallic glasses-historical background [M]//GÜNTHERODT H-J, BECK H. *Glassy Metals I: Ionic Structure, Electronic Transport, and Crystallization*. Berlin, Heidelberg; Springer Berlin Heidelberg. 1981: 19-23.
- [37] Cohen M H, Turnbull D. Composition Requirements for Glass Formation in Metallic and Ionic Systems [J]. *Nature*, 1961, 189(4759): 131-132.
- [38] Duwez P, Willens R H, Crewdson R C. Amorphous Phase in Palladium—Silicon Alloys [J]. *Journal of Applied Physics*, 1965, 36(7): 2267-2269.
- [39] Chen H S, Turnbull D. Evidence of a Glass–Liquid Transition in a Gold–Germanium–Silicon Alloy [J]. *The Journal of Chemical Physics*, 1968, 48(6): 2560-2571.
- [40] Chen H S, Turnbull D. Formation, stability and structure of palladium-silicon based alloy glasses [J]. *Acta Metallurgica*, 1969, 17(8): 1021-1031.
- [41] Angell C A. Formation of glasses from liquids and biopolymers [J]. *Science*, 1995, 267(5206): 1924-1935.
- [42] Mader S, Nowick A S. METASTABLE Co–Au ALLOYS: EXAMPLE OF AN AMORPHOUS FERROMAGNET [J]. *Applied Physics Letters*, 1965, 7(3): 57-59.
- [43] Duwez P, Lin S C H. Amorphous Ferromagnetic Phase in Iron - Carbon -

- Phosphorus Alloys [J]. *Journal of Applied Physics*, 1967, 38(10): 4096-4097.
- [44] Chen H S. Thermodynamic considerations on the formation and stability of metallic glasses [J]. *Acta Metallurgica*, 1974, 22(12): 1505-1511.
- [45] Johnson W L. Bulk Glass-Forming Metallic Alloys: Science and Technology [J]. *MRS Bulletin*, 1999, 24(10): 42-56.
- [46] Drehman A J, Greer A L, Turnbull D. Bulk formation of a metallic glass: Pd<sub>40</sub>Ni<sub>40</sub>P<sub>20</sub> [J]. *Applied Physics Letters*, 1982, 41(8): 716-717.
- [47] Kui H W, Greer A L, Turnbull D. Formation of bulk metallic glass by fluxing [J]. *Applied Physics Letters*, 1984, 45(6): 615-616.
- [48] Inoue A, Zhang T, Masumoto T. Glass-forming ability of alloys [J]. *Journal of Non-Crystalline Solids*, 1993, 156-158(Part 2): 473-480.
- [49] Inoue A, Takeuchi A. Recent progress in bulk glassy alloys [J]. *Materials Transactions*, 2002, 43(8): 1892-1906.
- [50] Inoue A, Kita K, Zhang T, et al. An Amorphous La<sub>55</sub>Al<sub>25</sub>Ni<sub>20</sub> Alloy Prepared by Water Quenching [J]. *Materials Transactions, JIM*, 1989, 30(9): 722-725.
- [51] Peker A, Johnson W L. A highly processable metallic glass: Zr<sub>41.2</sub>Ti<sub>13.8</sub>Cu<sub>12.5</sub>Ni<sub>10.0</sub>Be<sub>22.5</sub> [J]. *Applied Physics Letters*, 1993, 63(17): 2342-2344.
- [52] Lin X H, Johnson W L. Formation of Ti–Zr–Cu–Ni bulk metallic glasses [J]. *Journal of Applied Physics*, 1995, 78(11): 6514-6519.
- [53] Jörg F L. Bulk metallic glasses [J]. *Intermetallics*, 2003, 11(6): 529-540.
- [54] JIANG Q, XU X, NIU H, et al. Packing Densities and Glass Forming Ability of Alloys [J]. *J Mater Sci Technol*, 1996, 12(4): 299-302.
- [55] Johnson W L. Bulk metallic glasses — a new engineering material [J]. *Current Opinion in Solid State and Materials Science*, 1996, 1(3): 383-386.
- [56] Huang L, Pu C, Fisher R K, et al. A Zr-based bulk metallic glass for future stent applications: Materials properties, finite element modeling, and in vitro human vascular cell response [J]. *Acta Biomaterialia*, 2015, 25(C): 356-368.
- [57] Celtek M, Sengul S, Domekeli U. Glass formation and structural properties of Zr<sub>50</sub>Cu<sub>50-x</sub>Al<sub>x</sub> bulk metallic glasses investigated by molecular dynamics simulations [J]. *Intermetallics*, 2017, 84(1): 62-73.
- [58] Tsuei C C, Duwez P. Metastable Amorphous Ferromagnetic Phases in

- Palladium - Base Alloys [J]. *Journal of Applied Physics*, 1966, 37(1): 435-435.
- [59] Inoue A, Kato A, Zhang T, et al. Mg-Cu-Y Amorphous Alloys with High Mechanical Strengths Produced by a Metallic Mold Casting Method [J]. *Materials Transactions, JIM*, 1991, 32(7): 609-616.
- [60] Inoue A. Bulk amorphous and nanocrystalline alloys with high functional properties [J]. *Materials Science and Engineering: A*, 2001, 304-306(1): 1-10.
- [61] Lu K, Wang J T, Wei W D. A new method for synthesizing nanocrystalline alloys [J]. *Journal of Applied Physics*, 1991, 69(1): 522-524.
- [62] Fan C, Takeuchi A, Inoue A. Preparation and Mechanical Properties of Zr-based Bulk Nanocrystalline Alloys Containing Compound and Amorphous Phases [J]. *Materials Transactions, JIM*, 1999, 40(1): 42-51.
- [63] Wu G, Chan K-C, Zhu L, et al. Dual-phase nanostructuring as a route to high-strength magnesium alloys [J]. *Nature*, 2017, 545(7652): 80-83.
- [64] Zhu L, Ruan H, Li X, et al. Modeling grain size dependent optimal twin spacing for achieving ultimate high strength and related high ductility in nanotwinned metals [J]. *Acta Materialia*, 2011, 59(14): 5544-5557.
- [65] Lu L, Chen X, Huang X, et al. Revealing the Maximum Strength in Nanotwinned Copper [J]. *Science*, 2009, 323(5914): 607-610.
- [66] Wang W H. Correlations between elastic moduli and properties in bulk metallic glasses [J]. *Journal of Applied Physics*, 2006, 99(9): 093506.
- [67] Schiøtz J, Jacobsen K W. A Maximum in the Strength of Nanocrystalline Copper [J]. *Science*, 2003, 301(5638): 1357-1359.
- [68] Kou H, Lu J, Li Y. High - Strength and High - Ductility Nanostructured and Amorphous Metallic Materials [J]. *Advanced Materials*, 2014, 26(31): 5518-5524.
- [69] Andreas A K, Jörg F L, Florian H D T. Rapid Solidification and Bulk Metallic Glasses - Processing and Properties [M]. *Materials Processing Handbook*. CRC Press. 2007: 17.11-17.44.
- [70] Löffler J F. Recent progress in the area of bulk metallic glasses [J]. *Zeitschrift für Metallkunde*, 2006, 97(3): 225-233.
- [71] Schwarz R B, Johnson W L. Formation of an Amorphous Alloy by Solid-State Reaction of the Pure Polycrystalline Metals [J]. *Physical Review Letters*, 1983, 51(5): 415-418.
- [72] Russell K C. Phase stability under irradiation [J]. *Progress in Materials*

- Science, 1984, 28(3): 229-434.
- [73] Ponyatovsky E G, Barkalov O I. Pressure—induced amorphous phases [J]. Materials Science Reports, 1992, 8(4): 147-191.
- [74] Schultz L, Eckert J. Mechanically alloyed glassy metals [M]. Glassy Metals III: Amorphization Techniques, Catalysis, Electronic and Ionic Structure. Berlin, Heidelberg; Springer Berlin Heidelberg. 1994: 69-120.
- [75] Valiev R Z, Islamgaliev R K, Alexandrov I V. Bulk nanostructured materials from severe plastic deformation [J]. Progress in Materials Science, 2000, 45(2): 103-189.
- [76] Duwez P, Willens R H, Klement W. Continuous Series of Metastable Solid Solutions in Silver - Copper Alloys [J]. Journal of Applied Physics, 1960, 31(6): 1136-1137.
- [77] Duwez P, Willens R H, Jr. W K. Metastable Electron Compound in Ag - Ge Alloys [J]. Journal of Applied Physics, 1960, 31(6): 1137-1137.
- [78] Anantharaman T R, Suryanarayana C. Review: A decade of quenching from the melt [J]. Journal of Materials Science, 1971, 6(8): 1111-1135.
- [79] Liebermann H, Graham C. Production of amorphous alloy ribbons and effects of apparatus parameters on ribbon dimensions [J]. IEEE Transactions on Magnetics, 1976, 12(6): 921-923.
- [80] Sheldon K. Method of forming metallic filament cast on interior surface of inclined annular quench roll [M]. Google Patents. 1975.
- [81] Narasimhan M C. Continuous casting method for metallic strips [M]. U.S. Patent 4,142,571. 1979.
- [82] Masumoto T, Maddin R. The mechanical properties of palladium 20 a/o silicon alloy quenched from the liquid state [J]. Acta Metallurgica, 1971, 19(7): 725-741.
- [83] Huang S C, Fiedler H C. Amorphous ribbon formation and the effects of casting velocity [J]. Materials Science and Engineering, 1981, 51(1): 39-46.
- [84] Carpenter J, Steen P. Planar-flow spin-casting of molten metals: process behaviour [J]. Journal of materials science, 1992, 27(1): 215-225.
- [85] Wilde P D, Matthys E F. Experimental investigation of the planar flow casting process: development and free surface characteristics of the solidification puddle [J]. Materials Science and Engineering: A, 1992, 150(2): 237-247.
- [86] Sohrabi S, Arabi H, Beitollahi A, et al. Planar Flow Casting of



- Fe<sub>71</sub>Si<sub>13.5</sub>B<sub>9</sub>Nb<sub>3</sub>Cu<sub>1</sub>Al<sub>1.5</sub>Ge<sub>1</sub> Ribbons [J]. Journal of Materials Engineering and Performance, 2013, 22(8): 2185-2190.
- [87] Inoue A, Nakamura T, Sugita T, et al. Bulky La-Al-TM (TM=Transition Metal) Amorphous Alloys with High Tensile Strength Produced by a High-Pressure Die Casting Method [J]. Materials Transactions, JIM, 1993, 34(4): 351-358.
- [88] Löffler J F, Bossuyt S, Peker A, et al. Eutectic isolation in Mg-Al-Cu-Li(-Y) alloys by centrifugal processing [J]. Philosophical Magazine, 2003, 83(24): 2797-2813.
- [89] Löffler J F, Johnson W L. Crystallization of Mg-Al and Al-based metallic liquids under ultra-high gravity [J]. Intermetallics, 2002, 10(11): 1167-1175.
- [90] Chen M. A brief overview of bulk metallic glasses [J]. NPG Asia Mater, 2011, 3(9): 82-90.
- [91] Praisner T J, Chen J S, Tseng A A. An experimental study of process behavior in planar flow melt spinning [J]. Metallurgical and materials transactions B, 1995, 26(1): 1199-1208.
- [92] Frommeyer G, Frech W. Continuous casting and rapid solidification of wires produced by a newly developed shape flow casting technique [J]. Materials Science and Engineering: A, 1997, 226-228(Supplement C): 1019-1024.
- [93] Chen H S, Miller C E. A Rapid Quenching Technique for the Preparation of Thin Uniform Films of Amorphous Solids [J]. Review of Scientific Instruments, 1970, 41(8): 1237-1238.
- [94] Suzuki T, Anthony A-M. Rapid quenching on the binary systems of high temperature oxides [J]. Materials Research Bulletin, 1974, 9(6): 745-753.
- [95] Lee J G, Park S S, Lee S B, et al. Sheet fabrication of bulk amorphous alloys by twin-roll strip casting [J]. Scripta Materialia, 2005, 53(6): 693-697.
- [96] Lee J G, Lee H, Oh Y S, et al. Continuous fabrication of bulk amorphous alloy sheets by twin-roll strip casting [J]. Intermetallics, 2006, 14(8-9): 987-993.
- [97] Oh Y S, Lee H, Lee J G, et al. Twin-Roll Strip Casting of Iron-Base Amorphous Alloys [J]. MATERIALS TRANSACTIONS, 2007, 48(7): 1584-1588.
- [98] Urata A, Nishiyama N, Amiya K, et al. Continuous casting of thick Fe-base

- glassy plates by twin-roller melt-spinning [J]. *Materials Science and Engineering: A*, 2007, 449–451(12): 269-272.
- [99] Hofmann D C, Roberts S N, Johnson W L. Twin roll sheet casting of bulk metallic glasses and composites in an inert environment [M]. US. 2013.
- [100] East D R, Kellam M, Gibson M A, et al. Amorphous magnesium sheet produced by twin roll casting [J]. *Materials Science Forum*, 2010, 654-656(1): 1078-1081.
- [101] Pei Z, Ju D. Simulation of the Continuous Casting and Cooling Behavior of Metallic Glasses [J]. *Materials*, 2017, 10(4): 420.
- [102] Park Y S, Lee S B, Kim N J. Microstructure and Mechanical Properties of Strip Cast Al-Mg-Si-X Alloys [J]. *MATERIALS TRANSACTIONS*, 2003, 44(12): 2617-2624.
- [103] Miyazawa K, Szekely J. A mathematical model of the splat cooling process using the twin-roll technique [J]. *Metallurgical Transactions A*, 1981, 12(6): 1047-1057.
- [104] Lee J G, Park S S, Lee D, et al. Mechanical property and fracture behavior of strip cast Zr-base BMG alloy containing crystalline phase [J]. *Intermetallics*, 2004, 12(10): 1125-1131.
- [105] Szuecs F, Kim C P, Johnson W L. Mechanical properties of Zr<sub>56.2</sub>Ti<sub>13.8</sub>Nb<sub>5.0</sub>Cu<sub>6.9</sub>Ni<sub>5.6</sub>Be<sub>12.5</sub> ductile phase reinforced bulk metallic glass composite [J]. *Acta Materialia*, 2001, 49(9): 1507-1513.
- [106] Kim Y C, Na J H, Park J M, et al. Role of nanometer-scale quasicrystals in improving the mechanical behavior of Ti-based bulk metallic glasses [J]. *Applied Physics Letters*, 2003, 83(15): 3093-3095.
- [107] Takara A, Higashi K. The forming process of magnesium alloy for Japanese home electric components; proceedings of the Materials Science Forum, F, 2005 [C]. *Trans Tech Publ*: 509-512.
- [108] Matucha K H. *Materials Science and Technology, Structure and Properties of Nonferrous Alloys* [M]. Wiley, 1996.
- [109] Zhang J, Leng Z, Zhang M, et al. Effect of Ce on microstructure, mechanical properties and corrosion behavior of high-pressure die-cast Mg–4Al-based alloy [J]. *Journal of Alloys and Compounds*, 2011, 509(3): 1069-1078.
- [110] Wang J, Liao R, Wang L, et al. Investigations of the properties of Mg–5Al–0.3Mn–xCe (x=0–3, wt.%) alloys [J]. *Journal of Alloys and Compounds*, 2009, 477(1): 341-345.

- [111] Zhang J, Zhang D, Tian Z, et al. Microstructures, tensile properties and corrosion behavior of die-cast Mg–4Al-based alloys containing La and/or Ce [J]. *Materials Science and Engineering: A*, 2008, 489(1): 113-119.
- [112] Liu W, Cao F, Chang L, et al. Effect of rare earth element Ce and La on corrosion behavior of AM60 magnesium alloy [J]. *Corrosion Science*, 2009, 51(6): 1334-1343.
- [113] Yamasaki M, Hayashi N, Izumi S, et al. Corrosion behavior of rapidly solidified Mg–Zn–rare earth element alloys in NaCl solution [J]. *Corrosion Science*, 2007, 49(1): 255-262.
- [114] Koike J, Kobayashi T, Mukai T, et al. The activity of non-basal slip systems and dynamic recovery at room temperature in fine-grained AZ31B magnesium alloys [J]. *Acta Materialia*, 2003, 51(7): 2055-2065.
- [115] Kojima Y, Kamado S. Fundamental magnesium researches in Japan; proceedings of the Materials Science Forum, F, 2005 [C]. *Trans Tech Publ*: 9-16.
- [116] Qian M, Das A. Grain refinement of magnesium alloys by zirconium: Formation of equiaxed grains [J]. *Scripta Materialia*, 2006, 54(5): 881-886.
- [117] Kang S B, Kim J W, Kim H W. Effect of deformation route and Sc and Zr addition on ultra-fine grain formation and superplasticity in Al-Mg alloys; proceedings of the Materials science forum, F, 2006 [C]. *Trans Tech Publ*: 847-852.
- [118] Maltais A, Fiset M, Dubé D. Grain refinement of magnesium alloy AZ91D cast in permanent mold using mechanical vibrations; proceedings of the Materials Science Forum, F, 2003 [C]. *Trans Tech Publ*: 527-532.
- [119] Zhang Z Q, Le Q C, Cui J Z. Ultrasonic treatment of magnesium alloy melts and its effects on solidification microstructures; proceedings of the Materials science forum, F, 2007 [C]. *Trans Tech Publ*: 129-132.
- [120] Jian X, Xu H, Meek T T, et al. Effect of power ultrasound on solidification of aluminum A356 alloy [J]. *Materials Letters*, 2005, 59(2): 190-193.
- [121] Miwa K, Mizutani Y, Tamura T, et al. New application of electromagnetic vibration process for creation of high potential metallic materials; proceedings of the Materials science forum, F, 2007 [C]. *Trans Tech Publ*: 323-328.
- [122] Motegi T, Yano E, Tamura Y, et al. Clarification of grain refining mechanisms of superheat-treated Mg-Al-Zn alloy castings; proceedings

- of the Materials science forum, F, 2000 [C]. Trans Tech Publ: 191-198.
- [123] Lu L, Dahle A K, Taylor J A, et al. Theoretical and practical considerations of grain refinement of Mg-Al alloys; proceedings of the Materials Science Forum, F, 2005 [C]. Trans Tech Publ: 299-302.
- [124] Jin Q, Eom J-P, Lim S G, et al. A study on the grain refining effects of carbon inoculation by C<sub>2</sub>Cl<sub>6</sub> addition on AZ31 magnesium alloy; proceedings of the Materials Science Forum, F, 2003 [C]. Trans Tech Publ: 587-592.
- [125] Kim W J, Jeong H G. Strength of AZ31 Alloys Subject to Severe Deformation by ECAP and DSR; proceedings of the Materials science forum, F, 2007 [C]. Trans Tech Publ: 455-458.
- [126] Sun H Q, Shi Y N, Zhang M X, et al. Plastic strain-induced grain refinement in the nanometer scale in a Mg alloy [J]. Acta Materialia, 2007, 55(3): 975-982.
- [127] Jin Q, Lim S G, You B S. Effects of grain refinement on rollability of AZ31 Mg alloy; proceedings of the Materials Science Forum, F, 2005 [C]. Trans Tech Publ: 533-536.
- [128] Di H S, Li Y L, Ning Z-l, et al. New processing technology of twin roll strip casting of AZ31B magnesium strip; proceedings of the Materials Science Forum, F, 2005 [C]. Trans Tech Publ: 615-618.
- [129] Liu T, Wang Y D, Wu S D, et al. Improving the strength and ductility of magnesium alloys by grain refinement and texture modification; proceedings of the Materials science forum, F, 2005 [C]. Trans Tech Publ: 177-180.
- [130] Liang D, Cowley C B. The twin-roll strip casting of magnesium [J]. JOM, 2004, 56(5): 26-28.
- [131] Park S S, Oh Y S, Kang D H, et al. Microstructural evolution in twin-roll strip cast Mg–Zn–Mn–Al alloy [J]. Materials Science and Engineering: A, 2007, 449-451(Supplement C): 352-355.
- [132] Ding P-d, Pan F-s, Jiang B, et al. Twin-roll strip casting of magnesium alloys in China [J]. Transactions of Nonferrous Metals Society of China, 2008, 18(Supplement 1): s7-s11.
- [133] Hu X-d, Ju D-y, Zhao H-y. Thermal flow simulation of twin-roll casting magnesium alloy [J]. J Shanghai Jiaotong Univ (Sci), 2012, 17(4): 479-483.
- [134] Haga T, Suzuki S. Melt ejection twin roll caster for the strip casting of

- aluminum alloy [J]. *Journal of Materials Processing Technology*, 2003, 137(1–3): 92-95.
- [135] Jung I-H, Sanjari M, Kim J, et al. Role of RE in the deformation and recrystallization of Mg alloy and a new alloy design concept for Mg–RE alloys [J]. *Scripta Materialia*, 2015, 102(1): 1-6.
- [136] Hays C C, Kim C P, Johnson W L. Microstructure Controlled Shear Band Pattern Formation and Enhanced Plasticity of Bulk Metallic Glasses Containing in situ Formed Ductile Phase Dendrite Dispersions [J]. *Physical Review Letters*, 2000, 84(13): 2901-2904.
- [137] She J, Pan F, Zhang J, et al. Microstructure and mechanical properties of Mg–Al–Sn extruded alloys [J]. *Journal of Alloys and Compounds*, 2016, 657(1): 893-905.
- [138] Schloffer D, Bozorgi S, Sherstnev P, et al. Manufacturing and characterization of magnesium alloy foils for use as anode materials in rechargeable magnesium ion batteries [J]. *Journal of Power Sources*, 2017, 367(1): 138-144.
- [139] Murgia F, Weldekidan E T, Stievano L, et al. First investigation of indium-based electrode in Mg battery [J]. *Electrochemistry Communications*, 2015, 60(1): 56-59.

## Chapter 1 Introduction

## **Chapter 2 Kinetics of rapid solidification on microstructure and alloy composition design**

Deep eutectic points in binary and ternary alloy systems have been widely used as an indication for developing good glass formers. However, representing more than three components on a phase diagram is scarcely impossible, and the eutectic transitions in quaternary and higher systems are rarely known. Therefore, it is difficult to ferret out the compositions for best glass formers in multicomponent alloy systems. Most multicomponent metallic glasses found up to now have been identified by trial and error, and it requires considerable experience and involves major commitments in time and resources to develop new BMG materials. Uncovering the underlying mechanisms for the formation of BMGs is thus a compelling demand for research <sup>[1]</sup>.

### **2.1 Thermodynamics and kinetics of glass formation**

It is necessary to mention that any glass (and even more suitable for metallic glasses) is not in a thermodynamically stable (equilibrium) state. In fact, the thermodynamic principles are applicable only to the systems which are in equilibrium states. In spite of the above, when a system under the consideration of an undercooled liquid, using of thermodynamic principles is acceptable.

#### **2.1.1 Thermodynamic stability of metallic glasses**

The thermodynamic stability of a system at constant temperature and pressure is determined by its Gibbs free energy,  $G$ , defined as <sup>[2]</sup>

$$G = H - TS \quad (2-1)$$

where,  $H$  is the enthalpy,  $T$  is the absolute temperature.  $S$  is the entropy.

Thermodynamically, if a system has attained the lowest possible value of the Gibbs

free energy, it will be in a state of steady equilibrium, that is, it will not transform into any other phase(s) under given temperature and pressure conditions. The above equation predicts that by increasing entropy or decreasing enthalpy or both, a system at any temperature can be more stable. Metallic crystalline solids have the strongest atomic bonding and therefore the lowest enthalpy,  $H$ . Consequently, crystalline solids are most stable phases at low temperatures. On the other hand, the atomic vibration frequency increases with increasing temperature and consequently, the entropy,  $S$  is high at elevated temperatures. As a result, the product of temperature and entropy increases and therefore the value of  $-TS$  term dominates at higher temperatures.

Using the above concepts, it may be stated that a glass becomes more “stable” when the free energy of the glassy phase is lower than that of the competing crystalline phase(s). In other words, the change in free energy,  $\Delta G (= G_{\text{glass}} - G_{\text{crystal}})$  becomes negative. Mathematically expressed:

$$\Delta G = \Delta H_f - T\Delta S_f \quad (2-2)$$

where the  $\Delta$  symbol represents the change in these quantities between the final and initial states,  $H_f$  and  $S_f$  represent the enthalpy of fusion and entropy of fusion, respectively.

The system becomes stable when the value of  $G$  is the lowest, or  $\Delta G$  is negative. A negative value of  $\Delta G$  can be obtained either by decreasing the value of  $\Delta H_f$  or increasing the value of  $\Delta S_f$  or both. Since entropy is nothing but a measure of the different ways in which the constituent atoms can be arranged (microscopic states), this value will increase with increasing number of components in the alloy system.

Actually, in a constant temperature, the free energy of a system can also be decreased in cases of low chemical potential due to low enthalpy, and large interfacial



energy between the liquid and solid phases. Since it will be difficult to intentionally control these parameters in an alloy system, decreasing the free energy seems to be the easiest way to increase  $\Delta S_f$ . And this can be realized by having a large number of components in the alloy system.

### 2.1.2 Kinetics of glass formation

If the liquid could be cooled sufficiently rapidly to prevent the formation of detectable amount of a crystalline phase, glass formation could be achieved. Hence, the fact whether a glass forms or not is related to the rapidity with which the liquid could be cooled and also to the kinetic constants.

The kinetics of crystallization was first treated by Turnbull <sup>[3]</sup>. The following assumptions were made:

1. The composition of the crystals forming is the same as that of the liquid.
2. Nucleation transients are unimportant.
3. Bulk free energy change associated with the transformation of the undercooled liquid to the crystal phase,  $\Delta G_v$ , is given by the linear approximation,  $\Delta G_v = \Delta H_f \cdot T_r$ , where  $H_f$  is the molar enthalpy of fusion and  $\Delta T_r$  is the reduced undercooling ( $\Delta T_r = (T_l - T)/T_l$ , where  $T_l$  is the melting (liquidus) temperature).

The homogeneous nucleation rate,  $I$ , for the formation of crystalline nuclei from a supercooled melt (in a liquid free of nuclei or heterogeneous, i.e., preferred nucleation sites) can be expressed as

$$I = \frac{k_n}{\eta(T)} \exp \left[ -\frac{b\alpha^3\beta}{T_r(\Delta T_r)^2} \right] \quad (2-3)$$

where,  $b$  is a shape factor ( $=16\pi/3$  for a spherical nucleus);  $k_n$  is a kinetic constant;  $\eta(T)$  is the shear viscosity of the liquid at temperature  $T$ ;  $T_r$  is the reduced temperature ( $T_r = T/T_l$ );  $\Delta T_r$  is the reduced supercooling ( $\Delta T_r = 1 - T_r$ );  $\alpha$  and  $\beta$  are dimensionless parameters related, respectively, to the liquid/solid interfacial energy ( $\sigma$ ) and to the molar entropy of fusion,  $\Delta S_f$ .

Thus,

$$\alpha = \frac{(N_A \bar{V}^2)^{1/3} \sigma}{\Delta H_f} \quad (2-4)$$

$$\beta = \frac{\Delta S_f}{R} \quad (2-5)$$

where,  $N_A$  is Avogadro's number;  $\bar{V}$  is the molar volume of the crystal;  $R$  is the universal gas constant.

It is clear from Equation (2-3) for  $I$  that for a given temperature and  $\eta$ , as  $\alpha^3\beta$  increases, the nucleation rate decreases very steeply. Increase in  $\alpha$  and  $\beta$  means an increase in  $\sigma$  and  $\Delta S_f$  and/or a decrease in  $\Delta H_f$ , all consistent with the thermodynamic approach of increased glass-forming ability explained in section 2.2.1.

## 2.2 Evaluation of critical cooling rate

It has generally been noted that the solidification rate achieved,  $R$ , is inversely proportional to the square of the thickness of the solidified molten layer. For a layer of thickness  $x$  that has solidified at a heat transfer coefficient of  $\infty$ , the solidification rate may be expressed as:

$$R = \frac{A}{x^2} \quad (2-6)$$

where,  $x$  is the distance from the splat/substrate interface, the constant  $A$  is a function of the material properties and initial temperatures, but is independent of  $x$  [2].

The value of  $A$  is  $8.1 \times 10^{-3} \text{ m}^2 \cdot \text{K} \cdot \text{s}^{-1}$  for ideal cooling (when the heat transfer coefficient is  $\infty$ ) and it is less for non-ideal cooling conditions. For example, assuming an average value of  $A = 10^{-3} \text{ m}^2 \cdot \text{K} \cdot \text{s}^{-1}$ , for rough estimates, the solidification rate achieved will be approximately  $10^5 \text{ K} \cdot \text{s}^{-1}$  for  $x = 100 \text{ } \mu\text{m}$  and  $10^9 \text{ K} \cdot \text{s}^{-1}$  for  $x = 1 \text{ } \mu\text{m}$ . The typical thickness of a rapidly solidified foil is about  $50 \text{ } \mu\text{m}$ , and therefore the foil would have solidified at a rate of approximately  $10^6 \text{ K} \cdot \text{s}^{-1}$ . These examples are used to illustrate that in order to obtain a high solidification rate, it is necessary to make the cross section thickness as small as possible [2]. In order to evaluate the critical cooling rates of metallic glass formation, lots of works had been taken out by researchers, but it seems that quantitative measurements of critical cooling rates are cumbersome and impractical for alloy development [4, 5].

In the current study, in order to evaluate the critical cooling rate of glass formation, continuous cooling transformation (CCT) diagrams of Mg-based alloys were proposed, which expressed the beginning line of crystal transformation from supercooled liquid, as shown in Fig. 2.1. If the required time which need by a supercooled liquid for forming detectable amount of crystalline phase could be calculated under each temperature before a liquid metal becomes solid ( $t_1, t_2, \dots, t_n$ ), then one can plot the temperature versus the required time, it forms a C-curve that expresses the crystalline phase transformation. In Fig. 2.1, the left side of C-curve shows there exist an undetectable number of crystals or crystal nuclei and liquids cool down in this zone will form glassy phase, e.g., the red dashed line. The right side of the C-curve expresses the crystal region and liquids cool down in this zone will form crystalline solids, e.g., the blue dashed line. The CCT diagram will be a convenient tool in process design and quality control in synthesizing new materials contain non-crystalline phases.

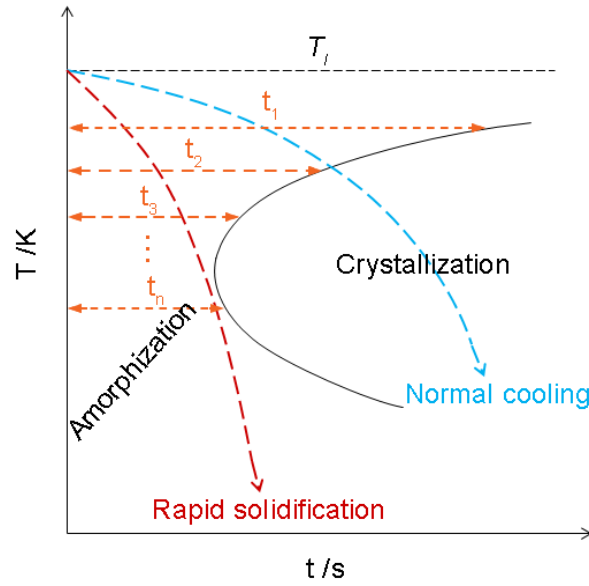


Fig. 2.1 Illustration of CCT diagram indicated the beginning line of crystal transformation from supercooled liquid.

### 2.2.1 Calculation of time reduced-temperature transformation and CCT diagrams

#### 1. Calculation of time reduced-temperature transformation (T-T<sub>r</sub>-T) diagram

The expression ‘glass’, in its original sense, refers to an amorphous or non-crystalline solid formed by continuous cooling of a liquid, while a solid is defined as any body having a viscosity greater than a somewhat arbitrary  $10^{14}$  P [6]. The viscosity of supercooled liquid metals is commonly described by the Vogel-Fulcher-Tammann (VFT) relation:

$$\eta(T) = \eta_0 \exp\left(\frac{B}{T - T_0}\right) = \eta_0 \exp\left(\frac{D^* T_0}{T - T_0}\right) \quad (2-7)$$

where  $T_0$  is known as an ideal glass transition temperature and B are constant depending on materials.  $\eta_0$  has the relation of  $\eta_0 = N_A h / V$ , with  $N_A$ , Avogadro’s constant,  $h$ , Planck’s constant and  $V$ , the molar volume [7]. In this paper, the values of  $V$  are

calculated by the JMatPro software firstly, as shown in Fig. 2.2. And then we can get  $\eta_0$  of each alloy, as listed in Table 2.1. It was found that the value of B is small in liquid metals, and  $T_0$  is a substantial fraction (e.g.  $\sim 1/3$  to  $2/3$ ) of melting temperature  $T_m$  [6].  $D^*$  is the fragility parameter ( $1 \leq D^* \leq 100$ ). Liquids are commonly referred to as “fragile” when  $D^* < 10$  and “strong” when  $D^* > 20$  [8].

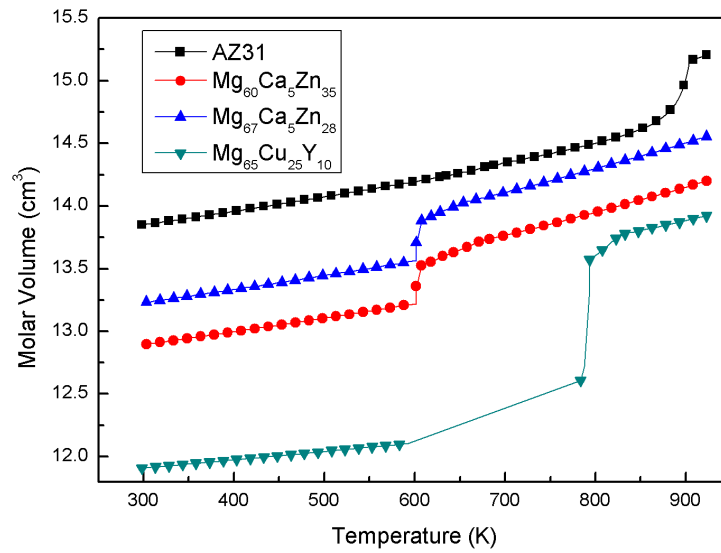


Fig. 2.2 Molar Volume of Mg-based alloys.

Table 2.1 Parameters used for the calculation of T-T<sub>r</sub>-T diagram for magnesium alloy

Alloy	$\eta_0$ / Pa·s	B/ K	B <sub>r</sub>	D*	T <sub>0</sub> / K	T <sub>0r</sub>	T <sub>m</sub> / K	x	No.
AZ31	$2.62 \times 10^{-5}$	4515	5	16.7	270.9	0.3	903	$10^{-6}$	
		5056.8	5.6	22	229.8	0.25			
		6501.6	7.2	18	361.2	0.4			
		2257.5	2.5	5	451.5	0.5			
		2022.7	2.24	4	505.68	0.56			
		4695.6	5.2	13	361.2	0.4			
Mg <sub>60</sub> Ca <sub>5</sub> Zn <sub>35</sub>	$2.89 \times 10^{-5}$	3530	5	11.1	317.1	0.45	706	$10^{-6}$	a-1
		3530	5	10.6	331.82	0.47			a-2
		3530	5	9.8	360.06	0.51			a-3
		4236	6	12.8	331.82	0.47			a-4
		5648	8	22.9	247.1	0.35			a-5
		4942	7	20	247.1	0.35			a-6
Mg <sub>76</sub> Ca <sub>5</sub> Zn <sub>28</sub>	$2.81 \times 10^{-5}$	2916	4.5	9	324	0.5	648	$10^{-6}$	b-1

Alloy	$\eta_0/\text{Pa}\cdot\text{s}$	B/ K	$B_r$	$D^*$	$T_0/\text{K}$	$T_{0r}$	$T_m/\text{K}$	x	No.
		5184	8	29.6	174.96	0.27			b-2
		5184	8	26.7	194.4	0.3			b-3
		4536	7	21.2	213.84	0.33			b-4
$\text{Mg}_{65}\text{Cu}_{25}\text{Y}_{10}$	$2.93 \times 10^{-5}$	5746	7.9	22.1	260	0.36	730	$10^{-6}$	c

The following equation <sup>[9]</sup>,

$$t = \left[ \frac{31}{k} \left( \frac{x a_0^9}{N_v} \right)^{1/4} \right] \times \left[ \frac{1}{T_r \Delta T_r^{3/4}} \exp \left( \frac{0.268}{T_r^3 \Delta T_r^2} \right) \exp \left\{ \frac{2}{5} \left( \frac{T_r}{\Delta T_r} \right)^{3/4} \right\} \right] \times \left[ \eta_{0r} \exp \left( \frac{B_r}{T_r - T_{0r}} \right) \right] \quad (2-8)$$

gives a time transformation curve (C-curve) that expresses the time to transform to crystal as a function of temperature. Here,  $k$  is the Boltzmann constant,  $x$  is the fraction of crystal formed in time  $t$ , and a volume fraction of  $10^{-6}$  as a just-detectable concentration of crystals was used <sup>[10]</sup>.  $a_0$  is the mean atomic diameter,  $N_v$  is the volume concentration of atoms.  $T_r (= T/T_m)$  is the reduced temperature, and  $\Delta T_r (= 1 - T_r)$  is the reduced undercooling of the melt.  $B_r$  and  $T_{0r}$  and  $\eta_{0r}$  are defined as  $B/T_m$ ,  $T_0/T_m$  and  $\eta_0/T_m$  respectively. The first term of the above equation is considered a constant <sup>[9]</sup>, in this paper it is  $0.89 \times 10^{-6} \text{ J} \cdot \text{K} \cdot \text{m}^3$ . Since  $B$  and  $T_0$  are empirical parameters and were not known clearly for the alloys below, referring to the data summarized by Takeuchi <sup>[9, 11]</sup>, parameters of hypothetical alloys used in this paper are listed in Table 2.1. These hypothetical alloys are assumed to have compositions range near the three given alloys (i.e., AZ31,  $\text{Mg}_{60}\text{Ca}_5\text{Zn}_{35}$  and  $\text{Mg}_{67}\text{Ca}_5\text{Zn}_{28}$ ). And the parameters of  $\text{Mg}_{65}\text{Cu}_{25}\text{Y}_{10}$  alloy are also listed for comparison <sup>[12]</sup>.

## 2. Calculation of CCT diagram

In order to determine the lowest cooling rate for a glass-forming material solidified from liquid state without crystallization, constructing a CCT curve instead of time-temperature-transformation (TTT) curve is more realistic <sup>[13]</sup>. And here, we used the additivity rule to relate the transformation behavior during continuous cooling with the isothermal transformation data calculated above.

The additivity rule was proposed by Scheil firstly and can be expressed by <sup>[14]</sup>:

$$\sum_{i=1}^n \frac{t_i}{\tau_i} = 1 \quad (2-9)$$

where  $t_i$  is the time spent at a particular temperature and  $\tau_i$  is the incubation time at that temperature. According to the additivity rule, CCT curve could be gained using the calculated T-T<sub>r</sub>-T diagram. And the cooling curves used for calculation are given by:

$$T(t) = T_m + qt \quad (2-10)$$

where  $q$  is the cooling rate, and here it is negative.

### 2.2.2 Estimation of the critical cooling rates using CCT curves

From equation (2-7), the following equation can be deduced:

$$\eta(T) = \eta_0 \exp\left(\frac{D^*}{T/T_0 - 1}\right) = \eta_0 \exp\left(\frac{D^*}{T_r/T_{0r} - 1}\right) \quad (2-11)$$

with the  $\eta_0$  is reduced to  $\eta_{0r}$ , the above equation becomes the third term expressed within the bracket of equation (2-8). And we can see that,  $D^*$ ,  $\eta_{0r}$  and  $T_{0r}$  are the main factors influencing the time of nucleation, with the variations of  $D^*$  and  $T_{0r}$ ,  $t$  changes exponentially.  $D^*$ , the fragility parameter of the supercooled liquid, relates to the nucleation and growth rate, and strong liquid behavior retards the formation of crystals kinetically and thermodynamically <sup>[12, 15]</sup>. It was found that strong glass formers exhibit a very small  $T_0$  and a very high melt viscosity, while fragile glass formers, show a  $T_0$

near  $T_g$ , as well as low melt viscosities <sup>[12]</sup>. For the Mg-based alloy  $Mg_{65}Cu_{25}Y_{10}$  glass forming liquid in R. Busch's study, which with  $D^*$  of 22.1, shows a strong liquid behavior.

The T-T<sub>r</sub>-T diagrams of Mg-based alloys listed in Table 2.1 calculated by equation. (2-8) are shown in Fig. 2.3. According to the above, alloys with compositions close to AZ31 could have small  $D^*$  and  $T_0$  near  $T_g$ , and they may have “C-curves” located between the area of the two curves which with  $B_r$  of 2.24 and 5.2, as shown in Fig. 2.3(a). The curve with  $B_r$  of 2.24 has a “nose time” of  $7.51 \times 10^{-4}$  s at  $T_r$  of 0.76 and a critical cooling rate of  $2.88 \times 10^5$  K/s. The curve with  $B_r$  of 5.2 has a “nose time” of  $1.78 \times 10^{-2}$  s at  $T_r$  of 0.75 and a critical cooling rate of  $1.27 \times 10^4$  K/s. Therefore, according to the T-T<sub>r</sub>-T curve, a critical cooling rate of four orders of magnitude was estimated for these alloys.

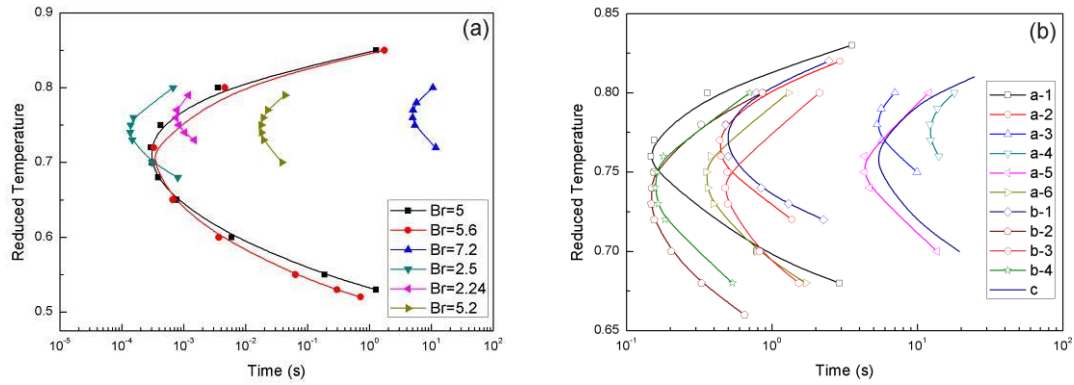


Fig. 2.3 Calculated T-T<sub>r</sub>-T diagrams: (a) alloys with compositions close to AZ31; (b) alloys with compositions close to  $Mg_{80-x}Ca_5Zn_{15+x}$  ( $x = 15$  and  $13$ ).

$Mg_{80-x}Ca_5Zn_{15+x}$  alloys ( $x = 5$  to  $20$ ) can be got under a cooling rate of  $10^2$  K/s or lower <sup>[16]</sup>, and then we calculated the probable values of  $B_r$  and  $T_{0r}$  of these alloys. As shown in Fig. 2.3(b), a series of C-curves were calculated with parameters listed in Table 2.1 for the alloys with compositions close to  $Mg_{80-x}Ca_5Zn_{15+x}$  ( $x = 15$  and  $13$ ) alloys. For the alloys number a-1, b-2 and b-4, they all have cooling rates of more than



1000K/s. For a-1 with  $D^*$  of 11.1, which is close to fragile liquid; for b-2 ( $D^* = 29.6$ ) and b-4 ( $D^* = 21.2$ ), which are classified as strong liquids, which values of  $T_{0r}$  are all not large enough for making cooling rates get down to  $10^2$  K/s. From Fig. 2.3(b), it can be inferred that  $Mg_{80-x}Ca_5Zn_{15+x}$  alloys ( $x = 5$  to 20) have a value of  $D^*$  from 10 to 25 and a relatively large  $T_{0r}$  associate with small  $D^*$ . And it was also found that, for the current series of alloys, the larger the  $D^*$  is, the smaller the reduced nose temperature gets.

As shown in Fig. 2.4, the calculated CCT curves of the alloy which has composition close to AZ31 with  $B_r$  of 2.24 (Fig. 2.4(a)) and  $Mg_{80-x}Ca_5Zn_{15+x}$  alloy with  $B_r$  of 7 and  $T_m$  of 706K (Fig. 2.4(b)). It can be found that the critical cooling rates of the two alloys are  $7.99 \times 10^4$  K/s and  $1.7 \times 10^2$  K/s respectively, and they are both lower than the values which attained from T-T<sub>r</sub>-T diagrams.

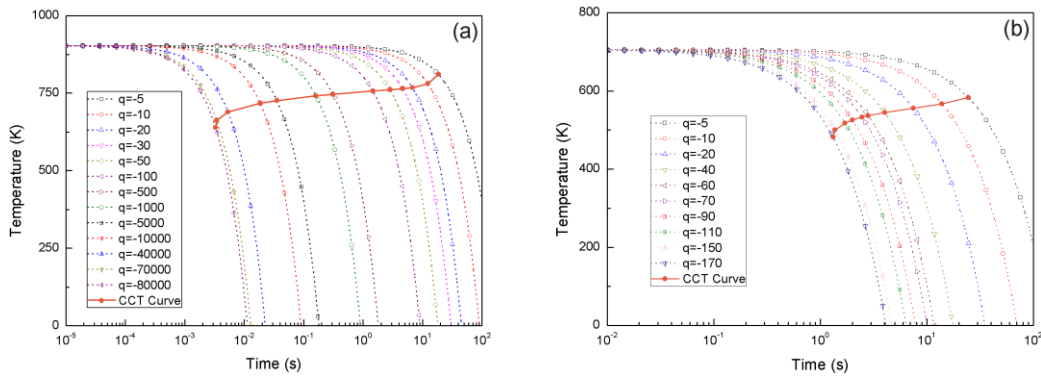


Fig. 2.4 Calculated CCT diagrams: (a) alloy with composition close to AZ31; (b) alloy with composition close to  $Mg_{80-x}Ca_5Zn_{15+x}$  ( $x = 15$  and 13).

### 2.2.3 Process programming—transition from TTT diagram to CCT diagram

During the constructing of CCT diagram, we developed two short programs to help calculating. The programs are shown in APPENDIX.

Executing the above programs in MATLAB software, a group of values of  $q$

(representing cooling rate in equation (2-10)) and  $T$  (temperature) could be attained, using equation (2-10) values of corresponding  $t$  (time) could be calculated. And then CCT diagram could be plotted finally.

### 2.3 Criteria of glass forming ability

#### 2.3.1 Characteristics of bulk metallic glasses

Bulk metallic glasses (BMGs) have the following four important characteristics <sup>[2]</sup>:

1. The alloy systems at least have three components, that is why they are commonly named as multicomponent alloy systems. Although binary BMGs have also been reported, but their maximum diameter of the rod products in fully glassy state is usually reported to be 1 or 2 mm. And even in such sections, a small volume fraction of nanocrystalline precipitates dispersed in the glassy matrix could frequently be observed.
2. The BMGs can be produced at slow solidification rates, typically  $10^3 \text{ K s}^{-1}$  or less. The lowest solidification rate was reported as  $0.067 \text{ K s}^{-1}$  (i.e.,  $4 \text{ K min}^{-1}$ ), which is indeed a really slow solidification rate.
3. BMGs exhibit large section thicknesses or diameters, a minimum of about 1 mm. The largest diameter of a bulk metallic glass rod produced is reported to be 72 mm of  $\text{Pd}_{40}\text{Cu}_{30}\text{Ni}_{10}\text{P}_{20}$  alloy.
4. A large supercooled liquid region is another character of BMGs. The difference between the glass transition temperature,  $T_g$ , and the crystallization temperature,  $T_x$ , (i.e.,  $\Delta T_x = T_x - T_g$ ) is large, usually a few tens of degrees, and the highest value reported so far is 131 K of  $\text{Pd}_{43}\text{Ni}_{10}\text{Cu}_{27}\text{P}_{20}$  alloy.

Akihisa Inoue <sup>[2]</sup> had mentioned that a metallic glass should not contain any

crystalline phases for it to be called a noncrystalline alloy. If it contains crystalline phases in addition to the glassy phase, it should be named as a composite more appropriately. Bulk metallic glass composites also have many interesting properties, but they are different from the BMGs. The presence of a broad and diffuse peak pattern by XRD techniques is often taken to be an evidence for the presence of a glassy phase and this is normally true. Inoue also point out that the technique of XRD is not very sensitive to the presence of a small volume fraction of a crystalline phase in a glassy phase, especially when the crystals are in nanocrystalline scales.

Starting with the initial discovery of the formation of BMGs in the La-Al-Ni system, Tohoku group in Japan produced a very large number of BMGs in different alloy systems based on Mg, Zr, Ti, Pd, Fe, Co, Ni, and Cu. During the last 20 years, they were able to produce several new alloys in the BMG state and also increase the critical diameter of the BMG alloy rods. In synthesis of BMG alloys, there are also many significant advances obtained by other researchers. The maximum diameters obtained in different alloy systems and the year in which they were discovered are presented in Fig. 2.5.

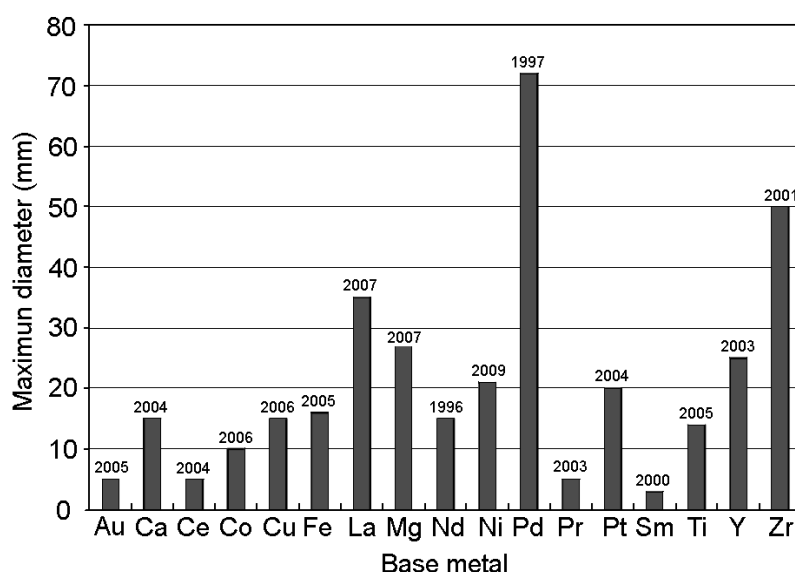


Fig. 2.5 Maximum diameters of the BMG rods achieved in different alloy systems and the years in which they were discovered <sup>[2]</sup>.

### 2.3.2 Three empirical rules for estimating glass forming ability

Based on the extensive data generated on the synthesized BMGs, Inoue had formulated three basic empirical rules for the formation of BMGs. They are stated as follows <sup>[17]</sup>:

1. The alloy must contain at least three components. The formation of glass becomes easier with increasing number of components in the alloy system.
2. A significant atomic size difference should exist among the constituent elements in the alloy. It is suggested that the atomic size differences should be above about 12% among the main constituent elements.
3. There should be negative heat of mixing among the (major) constituent elements in the alloy system.

### 2.4 Topological models of bulk glass formers

As more and more multicomponent bulk glass formers were detected, there have been many discussions on the underlying mechanisms of BMG formation. The excellent glass-forming ability of the new alloys has been generally attributed to the increased atomic packing density in the multicomponent system, as there are more atoms of the ‘right’ size to fill free space in the randomly packed glass structure <sup>[18]</sup>. This appears to be true since the total energy of alloys with directionless metallic bonding depends on the packing density; denser packing leads to lower energy and thereby higher stability. Besides consideration of the packing density, the improved glass-forming ability of the multicomponent systems has also been nominally understood by the ‘confusion principle’, i.e., the more elements involved, the lower the chance that the alloy can

select viable crystal structures, and hence the greater the chance of glass formation <sup>[19]</sup>. Since the discovery of metallic glasses by Duwez in 1959, a number of empirical rules on metallic glass formation have been suggested in consideration of factors such as atomic size, interatomic bonding, electron density and other structural features <sup>[20]</sup>. Although these empirical rules work for certain alloys, they frequently fail for others. By statistically analyzing hundreds of alloys that have excellent glassforming ability, Inoue suggested a more comprehensive set of empirical rules for the formation of BMGs <sup>[21]</sup>. Although most of the best glass formers follow those empirical rules, implying certain physical principles indeed play vital roles in the formation of BMGs in multicomponent systems, the empirical rules represent only the bare essentials for glass formation and are not sufficient for designing new alloys. The definite physical mechanisms for BMG formation therefore remain unclear, and the laws for quantitative composition design of bulk metallic glasses are still unknown <sup>[1]</sup>.

The difference in the densities between the as-cast amorphous and fully crystallized states is in the range of 0.30~0.54% <sup>[22]</sup>, which is much smaller than the previously reported value range of about 2% for ordinary amorphous alloys with much higher  $R_c$  above  $10^5$  K/s <sup>[21]</sup>. Such small differences in values indicate that the bulk amorphous alloys have higher dense randomly packed atomic configurations. On the assumption that a solid can exist in both the crystalline and noncrystalline states, it can be safely stated that the nearest neighbor distances are longer and the coordination numbers are smaller in a noncrystalline solid in comparison to its crystal counterpart <sup>[2]</sup>.

A topological model had been suggested by Senkov <sup>[18]</sup>. In their model, atomic concentrations were plotted versus atomic radii of the constitutive elements, and the concave upward shape of atomic size distributions for bulk amorphous alloys was pointed out, as shown in Fig. 2.6. As mentioned in their work, it should be noted that

there are a few exceptions from this trend, such as some Cu- and Mg-based alloys. However, the reason of these deviations is not clear yet.

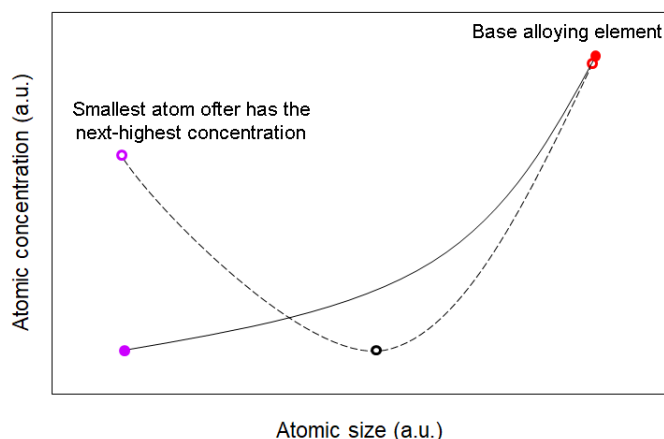


Fig. 2.6 Concave upward shape

In the Senkov's study <sup>[18]</sup> it was also found that ordinary amorphous alloys with high critical cooling rates showed a single-peak distribution with a concave downward shape. In these amorphous systems, there are at least one alloying element with a smaller radius, and at least one alloying element with a larger radius relative to the base element. As the difference in the atomic sizes of the base element and the alloying element increases, concentrations of the alloying elements decrease rapidly.

A model that explains the concave upward shape of atomic size distributions for the bulk amorphous alloys (the critical cooling rate is less than  $10^3 \text{ K}\cdot\text{s}^{-1}$ ) is suggested by Senkov. This model takes into account that all alloying elements in bulk glass formers are smaller than the matrix element, and some of them are located in interstitial sites while others substitute for matrix atoms in a reference crystalline solid solution. The interstitial and substitutional atoms attract each other and produce short-range ordered atomic configurations that stabilize the amorphous state. According to this model, the critical concentration of an interstitial element required to amorphize the alloy increases with increasing size difference from the matrix atom.

Formation of the liquid with specific atomic configurations and multicomponent interactions on a short-range scale has been suggested to increase the solid/liquid interfacial energy and decrease atomic diffusivity, which in turn, leads to suppression of nucleation and growth of crystalline phases <sup>[21]</sup>. Atomic size distributions of bulk amorphous alloys were summarized by Senkov <sup>[18]</sup>, as shown in Fig. 2.7. And the critical cooling rates of each group alloys are listed in Table 2.2.

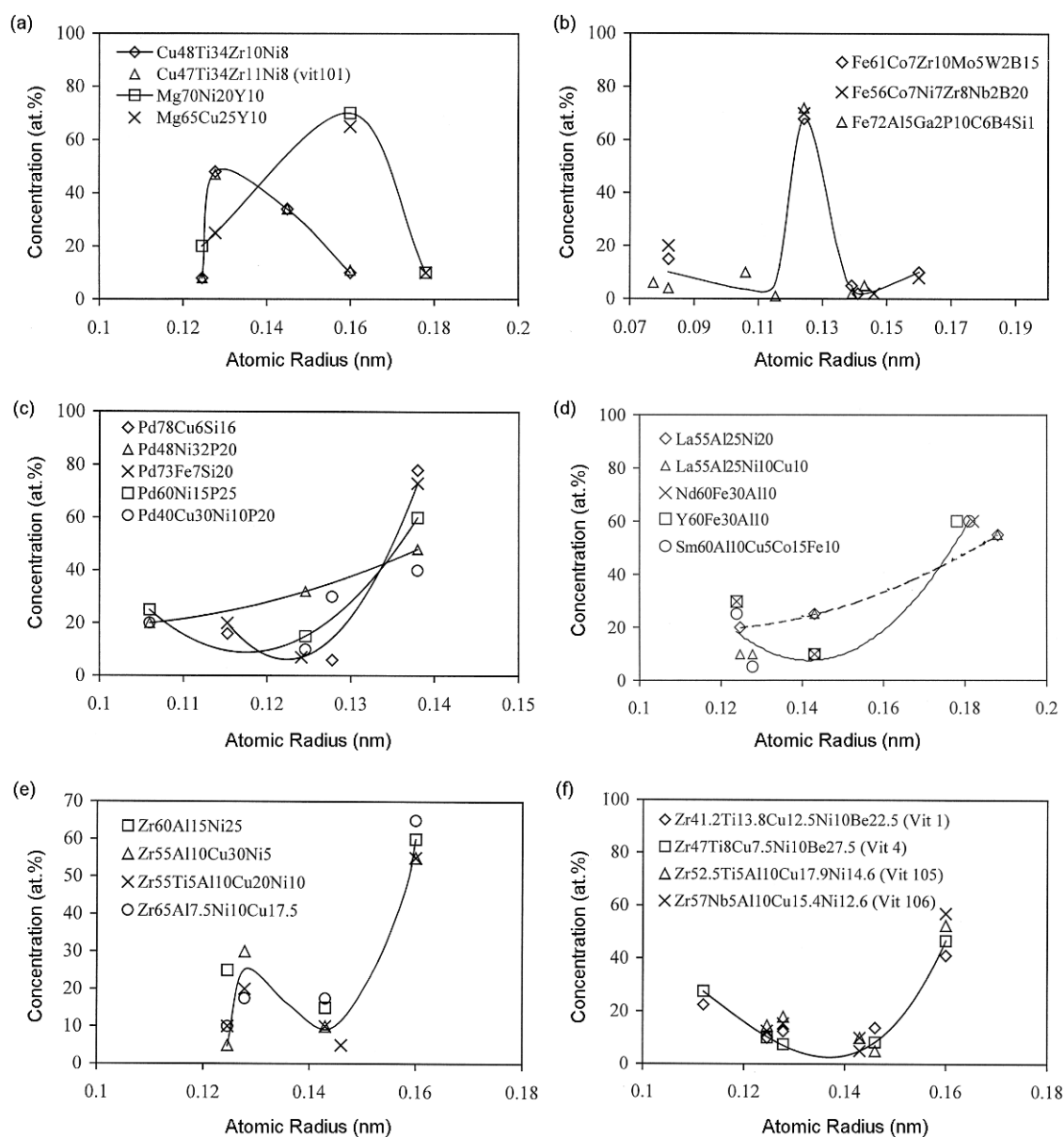


Fig. 2.7 Atomic size distributions of bulk amorphous alloys.

## Chapter 2 Kinetics of rapid solidification on microstructure and alloy composition design

Table 2.2 Critical cooling rates of different bulk amorphous alloys.

Alloy types in Fig. 2.7	Critical cooling rate/ ( $\text{K}\cdot\text{s}^{-1}$ )	Graph shape	Character
(a)	Mg-based: 30~100	Concave downward	Similar to ordinary amorphous alloys; Peaks are asymmetrical relative to the maximum
	Cu-based: $\leq 10^2 \sim 10^3$		
(b)	Fe and Co-based	Concave downward	Present valleys on both sides of the peak
(c)	Pd-based: 10~500	Concave upward	Base alloying element has the largest atomic size;
(d)	Platinum and rare-earth metal (Ln)-based		The concentrations of other alloying elements decrease when the atomic size decreases or show a minimum at an intermediate atomic size.
(e)	Zr-based: 1~500		alloys with higher critical cooling rates: atomic size distributions with two peaks, corresponding to Cu and Zr atoms
(f)		Concave upward	alloys with the best glass-forming ability: have a concave upward shape, similar to Pd-based alloys; the base alloy element is the largest atom, the smallest atom often has the next-highest concentration, atoms of intermediate radii are present at the lowest concentration.

From the above table, we can see that a concave upward plot generally characterizes bulk amorphous alloys with very good glass forming ability. On the other hand, Senkov also gave out a typical formulation of the amorphous alloys which have a critical cooling rate  $\geq 10^3 \text{ K}\cdot\text{s}^{-1}$ . They are commonly ternary or higher order alloys with 60–90% of the base metal. A significant concentration of each alloying element ( $\geq 5\%$ ) is typical. At least one alloying element is smaller and at least one is larger than the base element, the atomic radius of at least one of them falls well outside a bound of 15% of



the radius of the base atom, and the overall shape of the composition-radius plot is concave downward, with few exceptions <sup>[18]</sup>. There also came an conclusion that the concave upward distributions provide for more efficient atomic packing relative to alloys with concave downward distributions.

### 2.5 Alloy composition design

There are many criteria and models for evaluating glass forming ability or designing alloy compositions for bulk metallic glasses. Most of them are based on analysis of abundant experimental data or proposed empirically and not appropriate for all the alloy systems.

#### (1) Exceptions of the glass forming ability rules in Mg-based materials

Mismatch entropy normalized by Boltzmann constant ( $S_\sigma / k_B$ ) based on hard sphere model and mixing enthalpy ( $\Delta H$ ) based on regular solution model were expressed as a function of composition in multicomponent systems by Akira Takeuchi and Akihisa Inoue <sup>[23, 24]</sup>. They used the two parameters to evaluate glass forming abilities of multicomponent amorphous alloys, e.g., Pd-Cu-Ni-P, La-Al-Ni, Zr-Al-Ni-Cu and Fe-Co-Ni-Zr-B systems. The calculated  $R_c$  values are nearly the same order as the experimental data except Mg-Cu-Y system. It was said that the significant disagreement of Mg-based alloys may result from the low negative value of  $\Delta H$  <sup>[24]</sup>.

Atomic size distribution plots have been proposed by O.N. Senkov. It was found that a concave upward distribution correlates so strongly with improved glass forming ability. Mg-based alloys are deviate from this trend. This is another exception of Mg-based materials <sup>[18]</sup>.

(2) Compositions of the alloys

In order to retain an expect structure from the melt (1) appropriate quenching techniques must be applied, and (2) careful alloy selection must be made. Considering from the topological aspect, atomic radii of candidate alloying elements for magnesium alloys are listed in Table 2.3. Atomic size differences between the alloying elements and magnesium (aluminum) are also calculated, which are symbolized by  $ASD_{Mg}$  ( $ASD_{Al}$ ).

Table 2.3 Atomic radii <sup>[18]</sup> of some common elements used in Mg alloys.

Elements	Mg	Zn	Ca	Ge	Cu	In	Sn
Radius / nm	0.16013	0.13945	0.19760	0.12400	0.12780	0.16590	0.16200
$ASD_{Mg}$ / %		12.915	23.3997	22.563	20.19	3.6033	1.167
$ASD_{Al}$ / %	11.8461	2.598	38.0177	13.39	10.735	15.8762	13.1522
Elements	Mn	Al	Ti	Ce	La	Si	Y
Radius / nm	0.13500	0.14317	0.14615	0.18247	0.18790	0.11530	0.18015
$ASD_{Mg}$ / %	15.693	10.591	8.73	13.9512	17.3422	27.996	12.5023
$ASD_{Al}$ / %	5.707		2.0814	27.4499	31.2426	19.466	25.8294

Aluminum and Zinc are the two main alloying elements in magnesium alloy AZ31, which cause solid-solution hardening, grain refinement, and improving strength and ductility. AZ31B is a popular wrought magnesium alloy used in many aerospace and automotive applications. However, its widespread is hindered by the poor corrosion resistance and low ductility. As tin has the potential of improve creep resistance and ductility of Mg-Al alloy <sup>[25]</sup>, Indium is used in Mg battery materials <sup>[26, 27]</sup>, AZ31-In-Sn material is listed as one of the object materials in our study. This is not only because the above reasons, but also because that in our laboratory there is already a subject about this material on the research of battery plate <sup>[28]</sup>. With the purpose of trying to find out whether it can form an amorphous phase contained material through the rapid solidification of TRC method in the current study or not, AZ31-In-Sn alloy was studied in this work. And AZ31 alloy was adopted as a material for contrast.

## Chapter 2 Kinetics of rapid solidification on microstructure and alloy composition design

As stated in Chapter 1, rare earth (RE) element has a characteristic of so-called “scavenger effect” in magnesium alloys <sup>[29]</sup>, impurity elements could form less cathodic intermetallic compounds with RE, in order to improve the corrosion resistance of the product, Lanthanum and Cerium were adopted in our designment. The design contents of La and Ce are 5.20 wt% and 5.24%, respectively, which has referred to the result of Wenjuan Liu <sup>[29]</sup> (i.e., The optimal content of Ce and La for improving the corrosion resistance of AM60 magnesium alloy was 0.82 wt.% and 0.59 wt%).

Designed composition and the real composition after melted by high frequency induction melting are listed in Table 2.4 and Table 2.5. The real compositions were tested by X-ray fluorescence (XRF) analysis method.

Table 2.4 Composition of the AZ31-In-Sn alloy (D: designed composition; R: Real composition)

Elements		Mg	Al	Zn	In	Sn
Atomic mass		24.31	26.98	65.41	114.8	118.7
wt. %	D	91.2	2.85	1.95	2	2
	R	92.768	5.655	0.697	0.59	0.29
a.t. %	D	95.672	2.694	0.76	0.444	0.43
	R	94.378	5.188	0.247	0.127	0.060

Table 2.5 Composition of the Mg-RE alloy (D: designed composition; R: Real composition)

Elements		Mg	Al	Si	Mn	Zn	La	Ce
Atomic mass		24.31	26.98	28.09	54.94	65.41	138.9	140.1
a.t. %	D	94	4	-	-	-	1	1
	R	94.6	3.99	0.107	0.12	0.04358	0.464	0.66
wt. %	D	85.52	4.04	-	-	-	5.20	5.24
	R	89.2427	4.1779	0.1169	0.2550	0.1106	2.5007	3.5963

In order to compare the atomic size distribution of the designed alloy with Mg-based metallic glassy alloys in good glass forming abilities (e.g., Mg<sub>70</sub>Ni<sub>20</sub>Y<sub>10</sub> and Mg<sub>65</sub>Cu<sub>25</sub>Y<sub>10</sub>), atomic concentrations of these alloys were plotted versus atomic radii of the constitutive elements, as shown in Fig. 2.8. It can be seen from the plot that all the

three alloys we used are in concave downward shapes, which are similar to the Mg-based bulk metallic glasses. It should be noted that the shapes of three alloys are narrow than the shapes of Mg-based bulk metallic glasses, which indicate that glass forming abilities of the three alloys are lower.

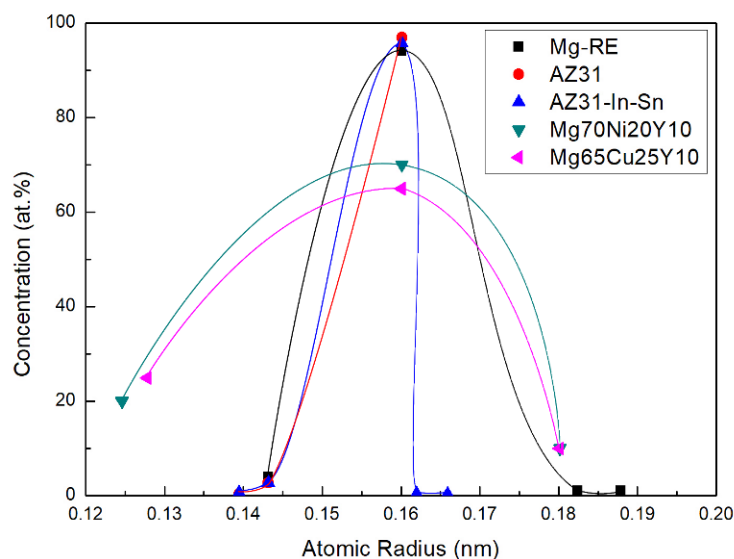


Fig. 2.8 Atomic size distributions in several magnesium alloys.

Although Yttrium is being used as a component of Mg-based bulk metallic glass materials, the reasons why we did not take it into consideration are: 1. Yttrium has a high melting point of 1522°C, 2. Yttrium can cause lung embolisms and have threat to liver. On the contrary, Lanthanum has a relatively low melting point of 920°C, the ion  $\text{La}^{3+}$  is used as a biological tracer for  $\text{Ca}^{2+}$ ; Cerium has a melting point of 798°C, Cerium sulfide is a non-toxic compound and is used as a pigment.

### 2.6 Concluding remarks

In this chapter, thermodynamics and kinetics of glass formation were briefly introduced. Using the homogeneous nucleation theory, TTT diagram which indicates the transformation of crystalline phase from supercooled liquid state was plotted. Based on the additivity rule, CCT diagram was transformed from the TTT diagram. In the

transformation process, we proposed two short programs to help calculation. And the critical cooling rates of materials to form metallic glasses were estimated.

Following the above, criteria for the formation of bulk metallic glasses were listed. We pointed out that all the criteria were based on analysis of abundant experimental data or proposed empirically and not appropriate for all the alloy systems. Referring to the criteria and considering the effects of alloying elements to Mg, three kinds of alloys (i.e., AZ31, AZ31-In-Sn and Mg-RE) were put forward as the objects for our study. Finally, the reasons why the above elements were selected were stated.

## References

- [1] Chen M. A brief overview of bulk metallic glasses [J]. NPG Asia Mater, 2011, 3(9): 82-90.
- [2] Suryanarayana C, Inoue A. Bulk metallic glasses [M]. CRC Press, 2010.
- [3] Turnbull D. Under what conditions can a glass be formed? [J]. Contemporary Physics, 1969, 10(5): 473-488.
- [4] Lu Z P, Liu C T. Glass Formation Criterion for Various Glass-Forming Systems [J]. Physical Review Letters, 2003, 91(11): 115505.
- [5] Ding S, Liu Y, Li Y, et al. Combinatorial development of bulk metallic glasses [J]. Nature materials, 2014, 13(5): 494-500.
- [6] Chen H S. Glassy metals [J]. Reports on Progress in Physics, 1980, 43(4): 353.
- [7] Lee S B, Kim N J. Kinetics of crystallization in continuously cooled BMG [J]. Materials Science and Engineering: A, 2005, 404(1–2): 153-158.
- [8] Jörg F L. Bulk metallic glasses [J]. Intermetallics, 2003, 11(6): 529-540.
- [9] Takeuchi A, Inoue A. Evaluation of Glass-Forming Ability for Metallic Glasses from Time-Reduced Temperature-Transformation Diagram [J]. MATERIALS TRANSACTIONS, 2001, 42(11): 2374-2381.
- [10] Uhlmann D R. A kinetic treatment of glass formation [J]. Journal of Non-Crystalline Solids, 1972, 7(4): 337-348.
- [11] Takeuchi A, Inoue A. Quantitative evaluation of critical cooling rate for metallic glasses [J]. Materials Science and Engineering: A, 2001, 304–306(1): 446-451.
- [12] Busch R, Liu W, Johnson W L. Thermodynamics and kinetics of the Mg<sub>65</sub>Cu<sub>25</sub>Y<sub>10</sub> bulk metallic glass forming liquid [J]. Journal of Applied Physics, 1998, 83(8): 4134-4141.
- [13] Xu K, Wang Y, Li J-f, et al. Critical cooling rate for the glass formation of ferromagnetic Fe<sub>80</sub>P<sub>13</sub>C<sub>7</sub> alloy [J]. Acta Metallurgica Sinica (English Letters), 2013, 26(1): 56-62.
- [14] Umemoto M, Horiuchi K, Tamura I. Pearlite Transformation during Continuous Cooling and Its Relation to Isothermal Transformation [J]. Transactions of the Iron and Steel Institute of Japan, 1983, 23(8): 690-695.
- [15] Busch R, Masuhr A, Johnson W L. Thermodynamics and kinetics of

- Zr–Ti–Cu–Ni–Be bulk metallic glass forming liquids [J]. *Materials Science and Engineering: A*, 2001, 304–306(00): 97-102.
- [16] Gu X, Shiflet G J, Guo F Q, et al. Mg–Ca–Zn Bulk Metallic Glasses with High Strength and Significant Ductility [J]. *Journal of Materials Research*, 2005, 20(08): 1935-1938.
- [17] Takeuchi A, Inoue A. Calculation of Supercooled Liquid Range and Estimation of Glass-Forming Ability of Metallic Glasses using the Vogel-Fulcher-Tammann Equation [J]. *MATERIALS TRANSACTIONS*, 2002, 43(5): 1205-1213.
- [18] Senkov O N, Miracle D B. Effect of the atomic size distribution on glass forming ability of amorphous metallic alloys [J]. *Materials Research Bulletin*, 2001, 36(12): 2183-2198.
- [19] Greer A L. Confusion by design [J]. *Nature*, 1993, 366(6453): 303-304.
- [20] Gutzow I, Kashchiev D, Avramov I. Nucleation and crystallization in glass-forming melts: Olds problems and new questions [J]. *Journal of Non-Crystalline Solids*, 1985, 73(1): 477-499.
- [21] Inoue A. Stabilization of metallic supercooled liquid and bulk amorphous alloys [J]. *Acta Materialia*, 2000, 48(1): 279-306.
- [22] Inoue A, Negishi T, Kimura H M, et al. High Packing Density of Zr- and Pd-Based Bulk Amorphous Alloys [J]. *Materials Transactions, JIM*, 1998, 39(2): 318-321.
- [23] Takeuchi A, Inoue A. Calculations of Mixing Enthalpy and Mismatch Entropy for Ternary Amorphous Alloys [J]. *Materials Transactions, JIM*, 2000, 41(11): 1372-1378.
- [24] Inoue A. Bulk amorphous and nanocrystalline alloys with high functional properties [J]. *Materials Science and Engineering: A*, 2001, 304-306(1): 1-10.
- [25] She J, Pan F, Zhang J, et al. Microstructure and mechanical properties of Mg–Al–Sn extruded alloys [J]. *Journal of Alloys and Compounds*, 2016, 657(1): 893-905.
- [26] Schloffer D, Bozorgi S, Sherstnev P, et al. Manufacturing and characterization of magnesium alloy foils for use as anode materials in rechargeable magnesium ion batteries [J]. *Journal of Power Sources*, 2017, 367(1): 138-144.
- [27] Murgia F, Weldekidan E T, Stievano L, et al. First investigation of indium-based electrode in Mg battery [J]. *Electrochemistry*

Communications, 2015, 60(1): 56-59.

- [28] Yu Z, Shi G, Ju D. Electrochemical Properties Evaluation of a Novel Mg Alloy Anode on Mg Air Batteries [J]. International Journal of Electrochemical Science, 2014, 9(11): 6668-6676.
- [29] Liu W, Cao F, Chang L, et al. Effect of rare earth element Ce and La on corrosion behavior of AM60 magnesium alloy [J]. Corrosion Science, 2009, 51(6): 1334-1343.



## Chapter 3 Simulation of solidification behavior during twin roll casting

### 3.1 Introduction

In continuous producing wide metallic ribbon process, a single wheel or a twin-roller configuration is commonly adopted. It first came to be a topic of considerable interest in the 1970s <sup>[1, 2]</sup>, and now the improvements and variations of the process are known as melt spinning and twin roll strip casting <sup>[3-6]</sup>. The melt spinning process involves the lips of nozzle held very close to the rotating wheel to attain wide sheets, and this will make the requirement in nozzle chosen strictly. Contrarily, in the twin roll casting process, molten metal is fed through two rotating rolls, and the formation of the final strip is controlled by the rolls nip, the question of nozzle is no longer that rigorous.

Over the past decade, many studies have been carried out on the fabrication of bulk amorphous alloy sheets via twin-roll casting (TRC) method <sup>[3-6]</sup>. It turns out that TRC is an available process for producing amorphous alloy sheets with a wide range of cooling rates. Well, nearly all the studies so far are based on horizontal type twin-roll casters. Previous studies show that the casting speed of VTRC is higher than horizontal-type twin-roll casting (HTRC), and the heat transmission of the VTRC is more effective <sup>[7, 8]</sup>. Vitreloy 1 ( $\text{Zr}_{41.2}\text{Ti}_{13.8}\text{Cu}_{12.5}\text{Ni}_{10.0}\text{Be}_{22.5}$ ) alloy is widely used for the study of TRC of bulk metallic glasses technique so far and has been investigated deeply, because it has a low critical cooling rate of 1 K/s and having a large amount of experimental data. And the processes are based on the horizontal type twin roll caster with casting speed from 0.6 m/min to 2.1 m/min <sup>[3, 4, 6, 9]</sup>. As for the alloys with less experimental data and could not be tested easily, however, numerical computation becomes a good method because adjustment of the process conditions, observation of the phenomena and measurement of the results are more convenient. As mentioned

above, heat transmission of VTRC is more effective than HTRC, a wide range of variable casting speed could also be attained by VTRC process. VTRC technique would be an effective method for producing metallic glass sheets continuously.

Twin-roll thin strip casting process combines casting and hot rolling process into a single step, in which the melt and solid state exist in the casting region. Amorphization or crystallization can occur depending on the cooling rates and thermal behavior experienced by the melt, and for a better understanding of the behavior of TRC process, thermal flow simulation is a good tool <sup>[3, 8]</sup>.

#### 3.2 Pilot vertical type twin roll caster

Generally, horizontal type twin roll casting technology was adopted in non-ferrous industry. However, vertical type twin roll casting technology has been successfully applied to steel industry. The output can reach 500000 tons/year, with higher casting speed and thinner gauge [1-5]. Recently, some researchers have focused their attention to vertical twin roll casting process for non-ferrous industry. T. Haga et al. have developed a high speed vertical type twin roll caster, magnesium alloys strip was cast with casting speed from 60 to 180 m/min and thickness 3 mm. As-cast sheets with equiaxed structure or spherical structure were attained in this caster and the mechanical properties were improved attributing to semisolid casting and rapid solidification [6-8].

In this research, a pilot vertical twin roll caster was employed, by which magnesium sheet casting experiments were carried out. The characteristics of vertical twin roll casting magnesium alloy sheets will be studied. The overview of pilot caster is shown in Fig. 3.1. The concept of strip casting is simple but the physical change phenomena during the strip casting process are very complicated [9-12]. The schematic diagram of pilot vertical twin roll caster is shown in Fig. 3.2.



Fig. 3.1 Pilot vertical twin roll caster

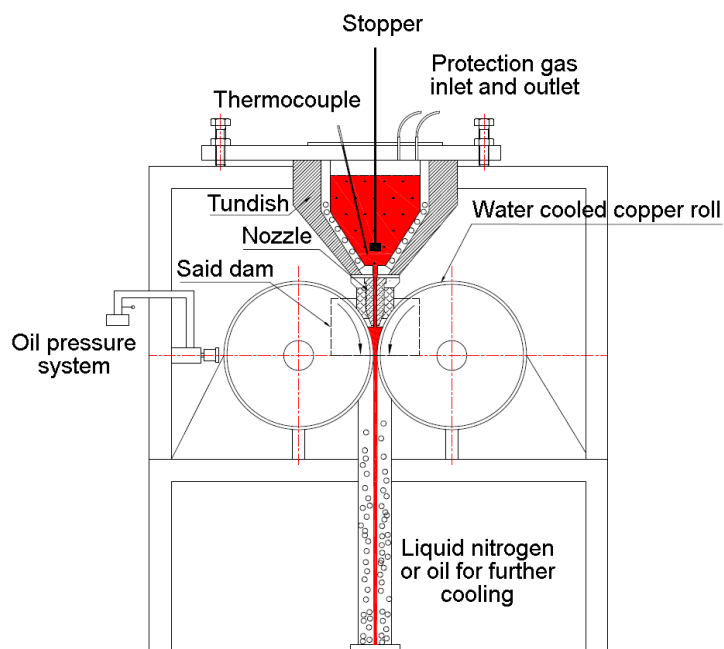


Fig. 3.2 Schematic diagram of the pilot vertical twin roll casting process

When the molten liquid from the tundish is poured into the space formed by two rotating rolls and side dams, solidification starts at the point of first metal-roll contact; the solidified shells will move with water cooled rolls and get thicker. When the thickness of the two solidified shell is more than the narrowest gap called ‘kissing

point' between the two rollers, the two solidified shells will be cohered above kissing point, the liquid metal in the mush zone will be crushed out upward in the coherence region and non-uniform deformation will occur until the strip exits the rolls because non-uniform temperature distribution along the strip thickness.

Twin roll casting process is a rapid solidification process, and all the physical changes will be happened in very short time. The complication of strip casting process reflects on three aspects <sup>[10-12]</sup>:

(1) It is difficult to get a uniform thickness strip. The as-cast strip thickness was affected by pool level, pour temperature, casting speed, separating force and these factors will interact and make it difficult to get a uniform thickness strip.

(2) It is difficult to get a crack free strip. High temperature gradient and deformation are the two main reasons causing strip cracks. Especially for magnesium alloy which has hexagonal close-packed crystal structure and poor formability. This is quite different from aluminum and steel materials in twin roll casting process.

(3) The microstructure and mechanical properties of as-cast strip were greatly affected by casting conditions, suitable mechanical properties and microstructure are the basic requirements for the consequent coiling and rolling process.

Therefore, precise measurement and control systems must be considered in every step of twin roll casting process from melting, refining, alloying, holding, pouring, metal delivering, and especially for the casting conditions of pouring temperature, molten level, separating force and casting speed.

The vertical pilot twin roll casting system in this study is consist of an integrated

### Chapter 3 Simulation of solidification behavior during twin roll casting

melting and melting metal delivering nozzle system, protection gas system, twin roll and side dam system, casting process control system for molten pool level, pouring temperature, separating force and casting speed, data acquisition system and in-line heat treatment system. The specification of the caster is listed in Table 3.1. The integrated melting and metal delivering nozzle system is used to heat magnesium alloy to a proper pouring temperature and uniformly distribute the melt metal to the molten pool, which is the core of a strip casting system; three places i.e. inner of tundish, molten pool surface and exit section were protected by a mixture of SF<sub>6</sub> 10% and Ar<sub>2</sub> 90% gas because molten magnesium is readily oxidized and ignited in air; the water cooled rolls made from Copper Chromium alloy and side dams made of refractory form the space containing the molten metal; two casting rolls are reverse rotated through drive shafts and gear reduction box by an AC motor; molten pool level, pouring temperature, separating force and casting speed are the main casting parameters that need to be controlled, which will influence the quality of as-cast strips greatly; the change of casting conditions during twin roll casting process are measured and record by data acquisition system. The as-cast strip will be dipped into an oil tank when it exits the casting rolls and quenched in the oil. This process not only can reserve the microstructure of as-cast strip at high temperature, which will convenient for the research of microstructure evolution during twin roll casting process at different casting conditions, but also can protect the high temperature as-cast strip surface from oxidation in air.

Table 3.1 Specification of vertical pilot twin roll caster

Items	Specification	Remark
Roll diameter	300 mm	Copper Chromium alloy
Roll width	100 mm	
Drive motor	AC 5 kW	Variable Frequency
Casting speed	6~30 m/min	
Strip thickness	0.5~4 mm	

### Chapter 3 Simulation of solidification behavior during twin roll casting

Items	Specification	Remark
Separating force	0-10000 N	
Nozzle	Slot type	Refractory<1000 ℃
Side dam		Refractory<1000 ℃
Protection gas	SF <sub>6</sub> 10% + CO <sub>2</sub> 90%.	

#### 3.3 Simulation of twin roll strip casting

In order to estimate the ability to produce metallic glasses by a vertical-type twin-roll caster, temperature distributions of the melt in molten pool were computed and cooling rates under different casting conditions were calculated with the simulated results.

##### 3.3.1 Simplifications, boundary conditions and governing equations

In this simulation, the following assumptions were made for a steady-state simulation: the rolls are regarded as rigid bodies; there is no relative slip between the roll and strip, and heat transfer coefficient between them is constant (i.e., 10 kW·m<sup>-2</sup>·K<sup>-1</sup> and 3 kW·m<sup>-2</sup>·K<sup>-1</sup>); free surface of the melt is steady; surface temperature of the roller is 373 K; considering the high speed feeding flow of liquid metal during the strip casting process character of the melt in casting zone is turbulent. Considering of the latent heat, equivalent specific heat method is adopted.

##### (1) Governing equations

The governing Navier-Stokes equations combined with the continuity equation, the thermal transport equation, and the constitutive property relationship is given by the following equation:

$$\frac{\partial}{\partial x_k}(\rho V_i \Phi) + \frac{\partial}{\partial t}(\rho C_\Phi \Phi) = \frac{\partial}{\partial x_k} \left( \Gamma_\Phi \frac{\partial \Phi}{\partial x_k} \right) + S_\Phi \quad (3-1)$$

### Chapter 3 Simulation of solidification behavior during twin roll casting

where  $\rho$  is the density,  $\Phi$  represents the dependent variable and  $C_\Phi$ ,  $\Gamma_\Phi$ , and  $S_\Phi$  indicate transient items, diffusion items and source items, respectively. Each correspond items are listed in Table 3.2. The time-averaging  $k$ - $\varepsilon$  model was used in the above obtain fluid flow equations.

Table 3.2 Representation of the items in the transport equations.

$\Phi$	Equations	$C_\Phi$	$\Gamma_\Phi$	$S_\Phi$
$I$	Continuous equations	$I$	0	0
$T$	Energy equations	$c$	$\mu$	$k$
$V_i$	Moments Equations	$I$	$\mu_e$	$-\frac{\partial P}{\partial x_k} + \frac{\partial}{\partial x_i} \left( \mu_e \frac{\partial V_k}{\partial x_i} \right) + \Delta \rho g_k$
$k$	Turbulent kinetic energy	$I$	$\mu_e/\sigma_k$	$\mu_t \left( \frac{\partial V_i}{\partial x_j} + \frac{\partial V_j}{\partial x_i} \right) \frac{\partial V_j}{\partial x_i} - \rho \varepsilon$
$\varepsilon$	Turbulent kinetic energy of dispersion rate	$I$	$\mu_e/\sigma_\varepsilon$	$C_1 \frac{\varepsilon}{k} \mu_t \left( \frac{\partial V_i}{\partial x_j} + \frac{\partial V_j}{\partial x_i} \right) \frac{\partial V_j}{\partial x_i} + C_2 \frac{\rho \varepsilon^2}{k}$

#### (2) Boundary conditions

- The inflow conditions of the molten metal at inlet are: temperature  $T = T_0$ , velocity in  $x$  direction  $v_x = 0$ , velocity in  $y$  direction  $v_y = v_0$ , pressure  $P = P_0$ .
- The conditions at exit are:  $\partial T/\partial y = 0$ ,  $v_x = 0$ ,  $v_y = v_0'$ .
- The conditions at metal-roll contact surface are:  $v_x = v_c \cdot (-\{Y\})/R$ ,  $v_y = v_c \cdot (\{x\} - 0.15 \cdot d/2)/R$ ,  $-k \cdot \partial T/\partial n = h_{pr} \cdot (T - T_{rs})$ ,  $v_c$  is the rotation speed of the roll,  $h_{pr}$  is the heat transfer coefficient between melt and roll.  $T_{rs}$  is the surface temperature of the roll.

- d. The conditions at metal-air contact surface are:  $v_x = 0$ ,  $v_y = v_c$ ,  $\partial T / \partial x = h_{pa} \cdot (T - T_{as})$ ,  $h_{pa}$  is the heat transfer coefficient between metal and air.  $T_{as}$  is the ambient temperature near the roll exit.

### 3.3.2 Thermal flow simulation

As shown in Fig. 3.3, the schematic of TRC process was illustrated with melt supplied in two ways (i.e., center pouring mode shown in Fig. 3.3(a), and one side pouring mode shown in Fig. 3.3(b)). Because the ratio of the width to thickness is quite large, neglect the side dams effect, a 2D finite element method (FEM) model is used. Influences of melt level  $h$ , strip thickness  $\delta$ , casting speed  $v$  (i.e., rotating speed) and pouring temperature  $T_p$  are considered in simulation. And considering geometric symmetry of the center pouring mode (i.e., Fig. 3.3(a)), half of the twin roll casting model was employed.

The formation of the molten pool of the one side pouring mode was illustrated in Fig. 3.4. The process and dimensions are specified as follows: the melt is ejected on one roll using a nozzle, a strip shell forms along the roll surface, and the strip shell thickness is marked as  $d$ , which has the same value as nozzle. And the metal shell of this part is cooled by the roll (the metal-roll contact side) and the atmosphere around it (the metal-air contact side). As it rolling down towards to the nip, the metal shell contacts to the other side roll, and the height to the nip from this location is marked as  $h$ . The metal of this part is cooled by both of the rolls. In Fig. 3.4(a),  $h$ , which is marked as  $h_a$ , depends on the metal shell thickness  $d$  and the roll gap. We can get a larger value of  $h$  with a smaller roll gap under a certain metal shell thickness  $d$ . In Fig. 3.4(b), it forms a molten liquid level.  $h$  here is marked as  $h_b$ , is higher than  $h_a$  under a same metal shell thickness and roll gap, and can change independently. With the effect of roll pressure (i.e., roll separating force), a thinner solidified strip forms and gets out from the roll nip.



The total height of the molten pool is marked as  $L$ .

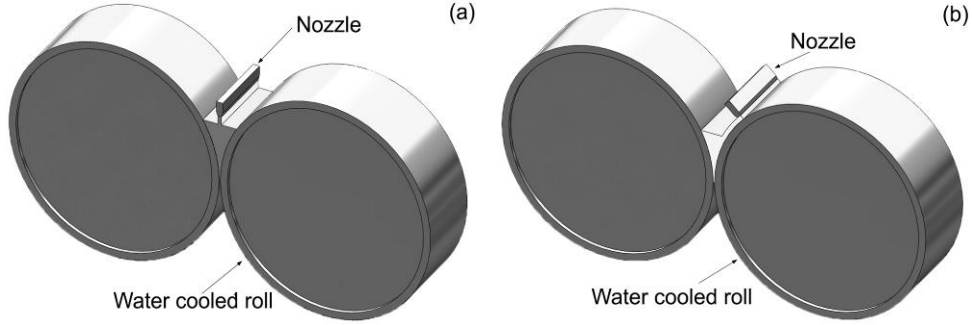


Fig. 3.3 Schematic of TRC process: (a) center pouring mode; (b) one side pouring mode.

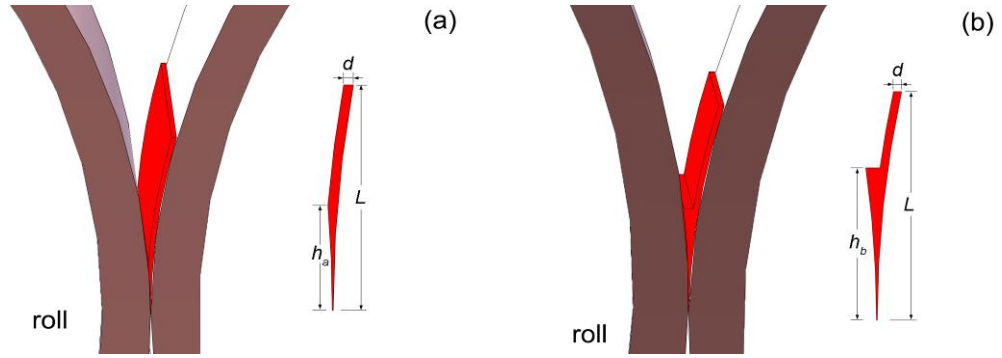


Fig. 3.4 Schematic of the molten pool of one side pouring mode: (a)  $h_a$  depends on the roll gap and  $d$ ; (b)  $h_b > h_a$  and can change independently.

### 3.4 Results and discussion

In the evaluation of the cooling ability of the twin-roll caster, average cooling rate,  $R_{AVG}$ , was calculated with the following equation:

$$R_{AVG} = \frac{\Delta T}{\Delta t} \approx \frac{T_p - T_{nip}}{h} \cdot v_c \quad (3-2)$$

where  $T_p$  and  $T_{nip}$  are, respectively, pouring temperature and temperature at the roll nip,  $h$  the melt level of molten pool, and  $v_c$  the casting speed. Fig. 3.5 shows the influences of different casting conditions on the average cooling rate for AZ31 alloy based on simulated results, and CP indicates the center pouring mode, OSP indicates the one side pouring mode. For the OSP mode, molten pool has a shape shown in Fig. 3.4(a). And

here, we call  $L$  the melt level. From these results we can see that the average cooling rate under the CP mode is faster than that under the OSP mode. Fig. 3.5(a) shows the results under the casting conditions of pouring temperature 953K, casting speed 0.5 m/s and strip thickness 0.08 mm.

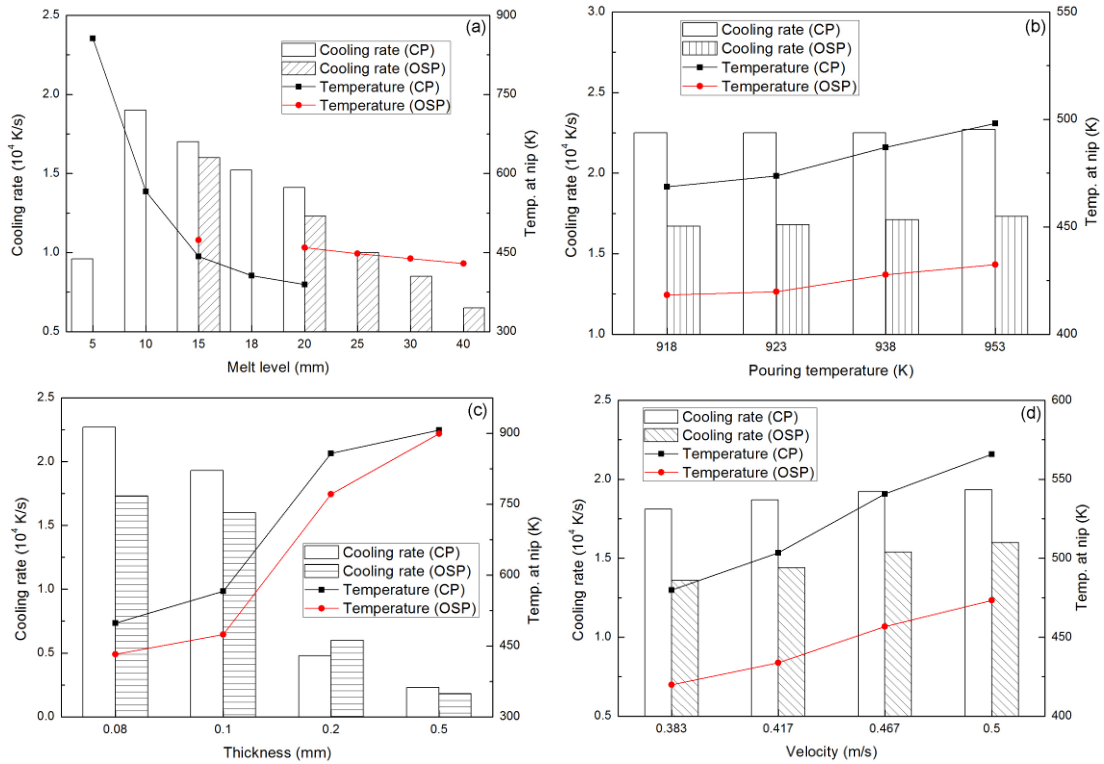


Fig. 3.5 Effects of casting conditions on cooling rate: (a) melt level; (b) pouring temperature; (c) strip thickness; (d) casting speed.

We can see that average cooling rate becomes slower with the increasing of melt level. Well, for the melt level of 5 mm, it is too fast to solidify within such a short metal-roll contact distance that temperature at the roll nip is 856.57 K, and the process will not continue. When the strip thickness (i.e., nip width) comes to 0.2 mm and 0.5mm with a melt level of 10 mm, as shown in Fig. 3.5(c), much more heat needs to be dissipated for the liquid gets fully solidified before it pass the roll nip, and the process cannot be continued too. On the other hand, with setting the melt level smaller and strip thickness thinner, a faster cooling rate could be attained and temperature at the roll nip

is also appropriate. However, it may cause a rolling block if the temperature at the roll nip gets too low since a fully amorphous metal is formed before it passes the roll nip. From Fig. 3.5(b) we can see that there is no influence of the pouring temperature on the average cooling rate, but it can adjust the temperature at roll nip, a lower pouring temperature leads to a lower nip temperature. And as a faster casting speed causes a faster cooling rate and a higher nip temperature (Fig. 3.5(d)), we can control the nip temperature through adjusting the pouring temperature. However, if the nip temperature is so high that it makes the temperature of the supercooled alloy still well above  $T_g$  before it passes the roll nip area, fully formation of amorphous structure might not be possible<sup>[3]</sup>, therefore the casting speed has an upper limit. Incidentally, the cooling rates at current conditions, as illustrated in Fig. 3.5(b) and (d), are all in the order of magnitude of  $10^4$  K/m, which has a same level with the calculated critical cooling rate.

Based on the continuum theory, a special form of material (or material-time) derivative for any physical quantity  $\psi$  under motion status in Eulerian coordinate has been proposed by Ju<sup>[13]</sup>:

$$\dot{\psi} = \frac{D\psi}{Dt} = \frac{\partial \psi}{\partial t} + \mathbf{v} \cdot \frac{\partial \psi}{\partial \mathbf{x}} \quad (3-3)$$

where  $\mathbf{v}$  is the velocity vector of material point,  $\mathbf{x}$  is a vector and represents a space-fixed coordinate system.

According to the theory above, in order to analyze the thermal phenomenon of the molten pool, cooling rate  $R(T)$  at the center of pool was calculated by:

$$R(T) = \frac{DT}{Dt} = \frac{\partial T}{\partial t} + v \cdot \frac{\partial T}{\partial y} \quad (3-4)$$

where  $T$  is the temperature at pool center,  $y$  is the location in the pool height direction,  $v$  is the velocity of the local melt, and  $t$  is the time. Temperature distributions of the

molten pool under the center pouring mode are shown in Fig. 3.6. Fig. 3.6(a) shows the temperature distribution of AZ31 alloy (with pouring temperature of 918 K, casting speed of 30 m/min, strip thickness of 0.08 mm, melt level of 10 mm) and illustrates the origin of coordinates used for calculation, point O is the center of the roll nip. Line D shows the isothermal line of 677.25 K ( $T_r = 0.75$ ), with a cooling rate of  $3.37 \times 10^4$  K/s calculated by the equation above, which has the same order of magnitude with the calculated critical cooling rate. Fig. 3.6(b) shows the temperature distribution of  $Mg_{80-x}Ca_5Zn_{15+x}$  ( $x = 5$  to 20) alloys (with pouring temperature of 736 K, casting speed of 3 m/min, strip thickness of 0.1 mm, melt level of 20 mm). It has a cooling rate of 2 to 3 orders of magnitude at the “nose temperature”.

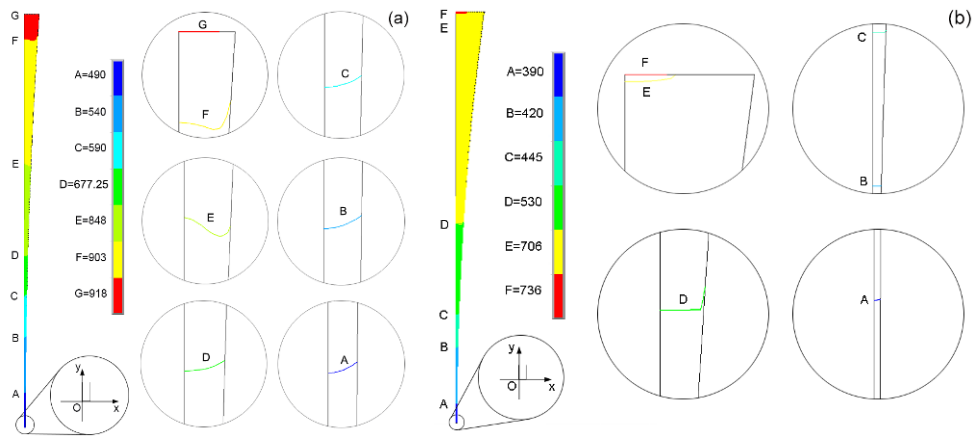


Fig. 3.6 Temperature distributions and isotherms of the center pouring mode: (a) AZ31 alloy; (b)  $Mg_{80-x}Ca_5Zn_{15+x}$  alloys ( $x = 5$  to 20).

In order to find out the characteristics of the pool metals under the two pouring methods (i.e., center pouring mode and one side pouring mode) mentioned above, temperature distributions of the molten pools during casting AZ31 alloy were compared and cooling rates at each temperature were also calculated (Fig. 3.7). Fig. 3.7(a) shows the results under the center pouring mode and with the following casting conditions: pouring temperature 918 K, casting speed 30 m/min, strip thickness 0.1mm and melt level 11.63 mm, which has a same value as  $h_a$  shown in Fig. 3.4(a). Fig. 3.7(b) shows the results under the one side pouring mode and has the same pouring temperature,

### Chapter 3 Simulation of solidification behavior during twin roll casting

casting speed and strip thickness as the center pouring mode. The value of  $h$  is 11.63 mm and  $L$  is 15mm (Fig. 3.4(a)), and we call this mode one side pouring mode-I. From these results we can see that, around the nose temperature of AZ31 alloy, cooling rates of four orders of magnitude could be attained under both of the two pouring methods. But under the one side pouring mode-I, we can get a faster cooling rate than under the center pouring one. On the other side, from the point of view of nip temperature, we can get a lower temperature at the roll nip in using the one side pouring mode-I.

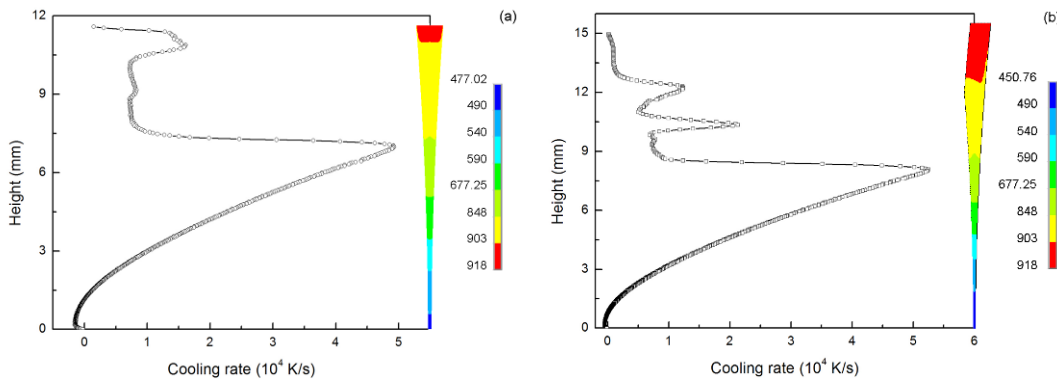


Fig. 3.7 Cooling rates and temperature distributions under the two pouring modes: (a) center pouring mode; (b) one side pouring mode.

In the twin roll casting process, one of the most important factors is the melt level  $L$ , and the influence of it to the temperature distribution is shown in Fig. 3.8. And we call the model used in Fig. 3.8(b) one side pouring mode-II. Casting conditions are as follows: pouring temperature 918 K, casting speed 30 m/min, strip thickness 0.1 mm, and melt levels under the two pouring mode are listed in Table 3.3. For the one side pouring mode-II, it has a strip shell thickness of 1mm (i.e.,  $d = 1$  mm).

Table 3.3 Influence of melt level to cooling rates and nip temperatures under the two pouring modes

Melt level $L$ / mm		11.63	15	20	25	30	35
Cooling rate $R(677.25)/$ $10^4 \text{ K}\cdot\text{s}^{-1}$	CP	2.83	3.49	1.92	32.7	37	
	OSP		3.41	1.9	2.23	1.44	1.53
$T_{\text{nip}}/ \text{K}$	CP	477.02	425.80	387.28	377.98	374.22	
	OSP		450.76	488.58	433.06	406.88	395.61

### Chapter 3 Simulation of solidification behavior during twin roll casting

The cooling rates along the center line of the molten pools were shown in Fig. 3.8(a) and (b). We can get a faster cooling rate with the CP mode when the melt level is not very high ( $L=15$  mm). However, when the melt level getting higher, the melt-roll contact area becomes larger, and the melt is cooled down directly to a low temperature, these would cause a rolling block. And one of the solution is adopting the OSP method to improve the temperature distribution.

It can be seen from Table 3.3 that, for a certain melt level, we can get a faster cooling rate with using the CP mode, and also nip temperature is lower than that under OSP mode. On the other hand, however, it is not expected to get a temperature too low at the roll nip because the special properties of metallic glass. Fully solidified metallic glass deforms hardly due to its very high strength. Therefore, we can use the OSP mode to adjust the strip temperature at nip for a certain melt level.

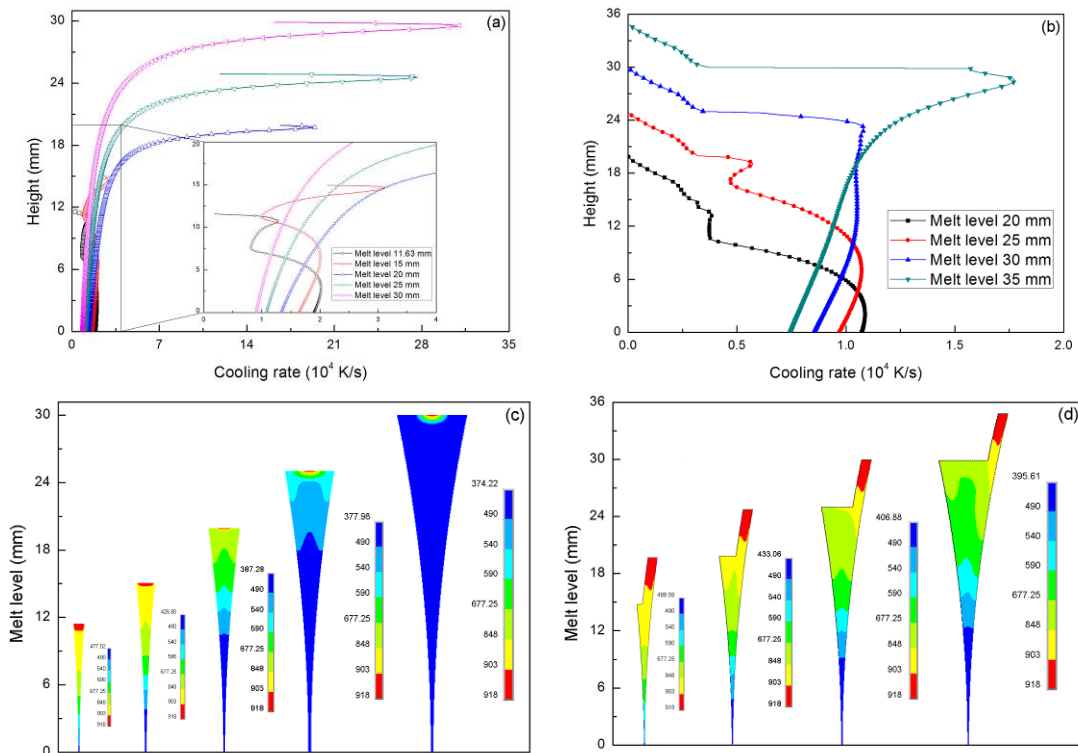


Fig. 3.8 Cooling rates rates and temperature distributions: (a, c) results of CP mode; (b, d) results of OSP mode.

Temperature distributions of the molten pools under the two pouring modes were shown in Fig. 3.8(c) and (d). The high temperature region under CP mode reduces rapidly compare with OSP mode as melt level getting higher. When the melt level is 30 mm, as shown in Fig. 3.8(c), mostly of the pool region is at low temperature, and this is not good for the casting process. In this situation, it is better to choose the OSP mode.

#### 3.5 Concluding remarks

In this chapter, based on a pilot caster in Saitama Institute of Technology, thermal-flow simulation was carried out to calculate the thermal and flow phenomena during TRC of magnesium alloys. In the VTRC process, simulation results under different casting conditions show that, we can attain a faster cooling rate using the center pouring mode comparing with the one side pouring mode when it forms a metal level in the molten pool because melt heat is extracted more efficiently of the former. However, for the situation of a molten pool with no formation of metal level (e.g., one side pouring mode-), a faster cooling rate could be attained in using the one side pouring mode. Changing the casting conditions or adopting the one side pouring mode could improve the temperature distribution of the pool metal, and the rolling block can be avoided. Cooling rates with 3 to 4 orders of magnitude by the VTRC process under the current conditions can be attained, which shows that VTRC technique has a potential ability in continuous fabrication of Mg-based bulk amorphous or amorphous phase and fine crystalline phase dual-phase alloys in sheet form.

#### References

- [1] Narasimhan M C. Continuous casting method for metallic strips [M]. U.S. Patent 4,142,571. 1979.
- [2] Andreas A K, Jörg F L, Florian H D T. Rapid Solidification and Bulk Metallic Glasses - Processing and Properties [M]. Materials Processing Handbook. CRC Press. 2007: 17.11-17.44.
- [3] Lee J G, Park S S, Lee S B, et al. Sheet fabrication of bulk amorphous alloys by twin-roll strip casting [J]. Scripta Materialia, 2005, 53(6): 693-697.
- [4] Lee J G, Lee H, Oh Y S, et al. Continuous fabrication of bulk amorphous alloy sheets by twin-roll strip casting [J]. Intermetallics, 2006, 14(8–9): 987-993.
- [5] Urata A, Nishiyama N, Amiya K, et al. Continuous casting of thick Fe-base glassy plates by twin-roller melt-spinning [J]. Materials Science and Engineering: A, 2007, 449–451(12): 269-272.
- [6] East D R, Kellam M, Gibson M A, et al. Amorphous magnesium sheet produced by twin roll casting [J]. Materials Science Forum, 2010, 654-656(1): 1078-1081.
- [7] Ding P-d, Pan F-s, Jiang B, et al. Twin-roll strip casting of magnesium alloys in China [J]. Transactions of Nonferrous Metals Society of China, 2008, 18(Supplement 1): s7-s11.
- [8] Hu X-d, Ju D-y, Zhao H-y. Thermal flow simulation of twin-roll casting magnesium alloy [J]. J Shanghai Jiaotong Univ (Sci), 2012, 17(4): 479-483.
- [9] Duggan G, Browne D J. Modelling and simulation of twin-roll casting of bulk metallic glasses [J]. Trans Indian Inst Met, 2009, 62(4-5): 417-421.
- [10] Steinbach S, Dagner J, Hainke M, et al. A combined numerical and experimental study of the effects of controlled fluid flow on alloy solidification; proceedings of the Materials science forum, F, 2006 [C]. Trans Tech Publ: 1753-1758.
- [11] Yun M, Lokyer S, Hunt J D. Twin roll casting of aluminium alloys [J]. Materials Science and Engineering: A, 2000, 280(1): 116-123.
- [12] Ju D, Oshika Y, Inoue T. Simulation of solidification and temperature in centrifugal casting process [J]. Journal of the Society of Materials Science



Japan, 1991, 40(449): 114-150.

- [13] Inoue T, Ju D-Y, Yosihara N. Temperature and Viscoplastic Stresses During Vertical Semi-Continuous Direct Chill Casting of Aluminum Alloy [M] BECK G, DENIS S, SIMON A. International Conference on Residual Stresses: ICRS2. Dordrecht; Springer Netherlands. 1989: 523-528.



## Chapter 4 TRC experiment and microstructure analyses

### 4.1 Experiment

Development of Mg alloy sheets has been quite slow due to the complexity of sheet production arising from the limited deformability of Mg <sup>[1]</sup>. In general, superplastic properties are exhibited in materials that have stable, equiaxed and fine grains under 10  $\mu\text{m}$  <sup>[2]</sup>. The microstructures of materials can be significantly altered by the conditions under which they are solidified <sup>[3]</sup>. Comparing with conventional ingot materials, rapidly solidified materials exhibit greatly reduced segregation levels. Thus, the grain size, dendrite arm spacing, and the size of constituent particles, precipitates and dispersoids are refined leading to significant reduction in diffusion times for homogenization. In contrast with conventional materials, rapid solidification processing has produced materials with greatly superior strength properties, improved corrosion resistance and a highly desirable combination of magnetic properties. Twin roll casting experiments were carried out in different casting conditions with the purpose of developing a novel Mg alloy sheets with good properties.

The ingots of AZ31-In-Sn alloy and Mg-RE alloy were prepared by induction melting the mixture of industrial AZ31 master alloy, pure In and Sn (for AZ31-In-Sn alloy) and pure Mg, Al and RE (for Mg-RE alloy) in an induction furnace under the protection of high-purity argon. Chemical compositions of the ingots were measured by X-ray Fluorescence spectrometry and the results are listed in Table 2.4 and Table 2.4. Twin roll casting experiments were carried out under casting conditions of casting speed 30 m/min and pouring temperature 953 K. Initial roll gap was set as 0 mm. An oil tank was set directly down to the rolls to avoid further grain growth as the as-cast strip was dipped into the oil tank as soon as it exits from the rolls.

Specimens for optical microscope (OM), scanning electron microscope (SEM) and electron probe micro-analysis (EPMA) were prepared by the standard technique of grinding and polishing, followed by etching in a saturated solution of picric acid.

### 4.1.1 Enlightenment form normal TRC experiment

As shown in Fig. 4.1, an AZ31 alloy bar was obtained by normal twin roll casting. It has a good toughness and could be bended over 180°. Microstructure of the as-cast AZ31 alloy bar is shown in Fig. 4.2. SEM images of the bar's cross section are shown in Fig. 4.3. The normal twin roll casting process had a casting speed of 10 rpm, with pouring temperature of 953K. The obtained strip had a thickness of 3 mm. During the casting process, a uniform strip with width of 100 mm was obtained at first. With the liquids in tundish reduced, the width of strip decreased and became a bar finally. Fig. 4.4 shows the microstructure of the as-cast strip obtained from the normal TRC process under the casting speed of 10rpm. We can see that it has an average grain size of 60  $\mu\text{m}$ . However, the alloy bar formed at the end of casting process, its grains sizes arranged from 3 $\mu\text{m}$  to 30 $\mu\text{m}$ , which was thought that this was due to the reduction of liquid mass. This leads to a decrease in thermal energy and an increased cooling rate. Thus, a fine grain alloy bar formed.



Fig. 4.1 Mg alloy bar obtained by normal twin roll casting process.

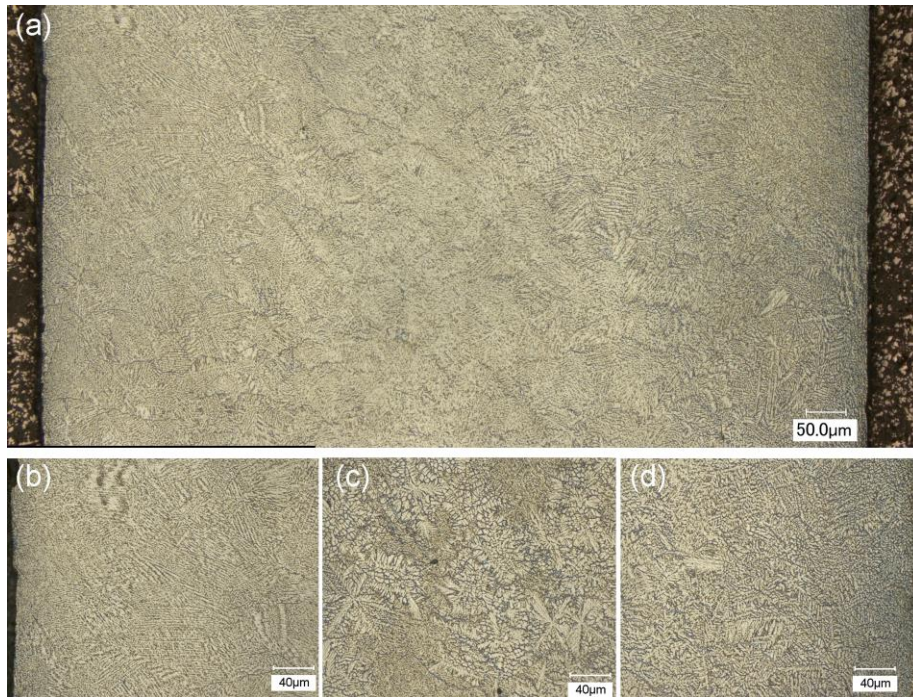


Fig. 4.2 Optical microstructure of the Mg alloy bar.

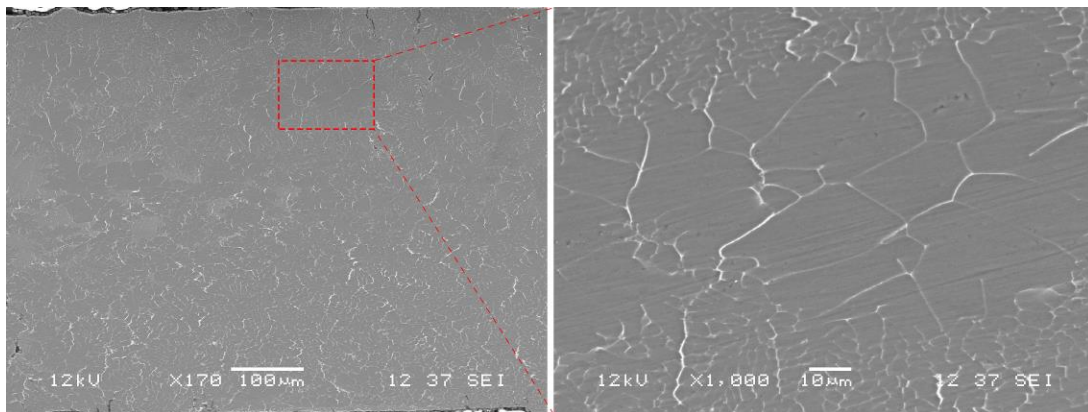


Fig. 4.3 SEM image of the Mg alloy bar in cross section.



Fig. 4.4 Microstructure of the as-cast strip produced by normal TRC.

From the phenomenon that the Mg alloy bar could be bended over 180°, we got some enlightenment with the following consideration: if we control the cooling rate faster during TRC process deliberately, whether or not the ductility of the strips would get better due to the rapid cooling impact or expectantly, whether or not we could get an amorphous phase due to the rapid cooling impact. Under this consideration, the following experiments were carried out.

### 4.1.2 Rapid solidification of TRC process

In order to get a faster cooling rate by the TRC process, we controlled the speed of the rolls at 30rpm, and set the initial roll gap into 0. Considering the separating force generated during casting, a metal block was set at the moving roll side to form a supporting force, to make a narrow roll gap during casting process as much as possible.

As AZ31B is a popular wrought magnesium alloy used in many aerospace and automotive applications, whilst its widespread is hindered by the poor corrosion resistance and low ductility, we carried out the experiments on this material firstly. Trying to find out whether we could get an amorphous phase or an amorphous phase and fine crystalline phase mixed dual phase microstructure.

#### (1) AZ31 alloy

An as-cast strip in thickness of 1.5mm and width of 80mm was produced by the rapid solidification TRC process. Fig. 4.5 shows the SEM image of the AZ31 alloy strip. It has an average secondary dendrite arm spacing (DAS) of about 2.2 μm.

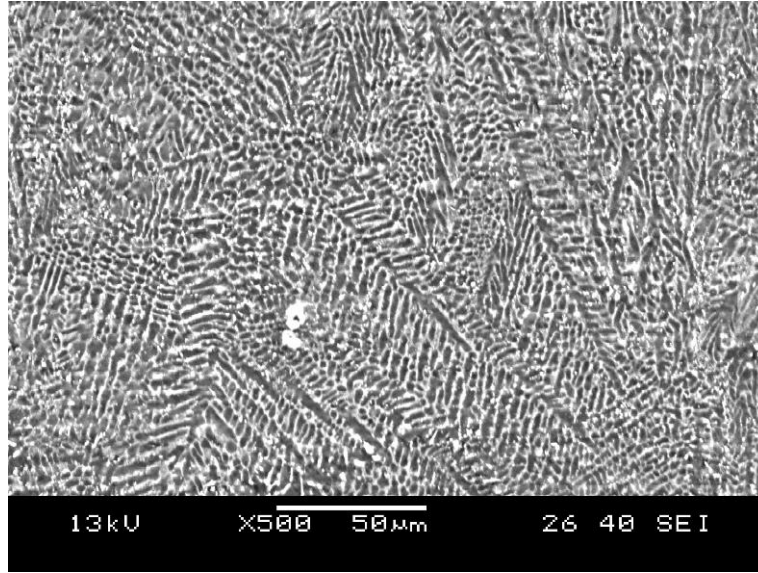


Fig. 4.5 SEM image of as-cast AZ31 alloy sheet in transverse section.

Dendrite arm spacing has been correlated with the overall solidification rate, and more rapid solidification rates resulting in finer dendrite arm spacings <sup>[3]</sup>. The relation between secondary dendrite arm spacing (DAS) and cooling rate can be described as the following equation <sup>[4]</sup>:

$$\lambda = 35.5R^{0.31} \quad (4-1)$$

where  $\lambda$  is DAS ( $\mu\text{m}$ ),  $R$  is cooling rate ( $\text{K}\cdot\text{s}^{-1}$ ).

Using the above equation, a cooling rate of  $7.9 \times 10^3 \text{K}\cdot\text{s}^{-1}$  can be calculated.

As the above sheet shows an dendrite microstructure, the expected glassy phase was not obtained, we made another effort. A smaller nozzle was set to the tundish. Under a small nozzle size, the liquid mass flowed slower and a 1.2 mm thickness strip was produced. Fig. 4.6 shows the SEM image of the strip. It forms by a number of equiaxed grains, and these equiaxed grains occupied 58% of the total area. Mg element distribution map of the as-cast AZ31 alloy strip specimen was recorded by electron probe micro-analysis (EPMA), as shown in Fig. 4.7.



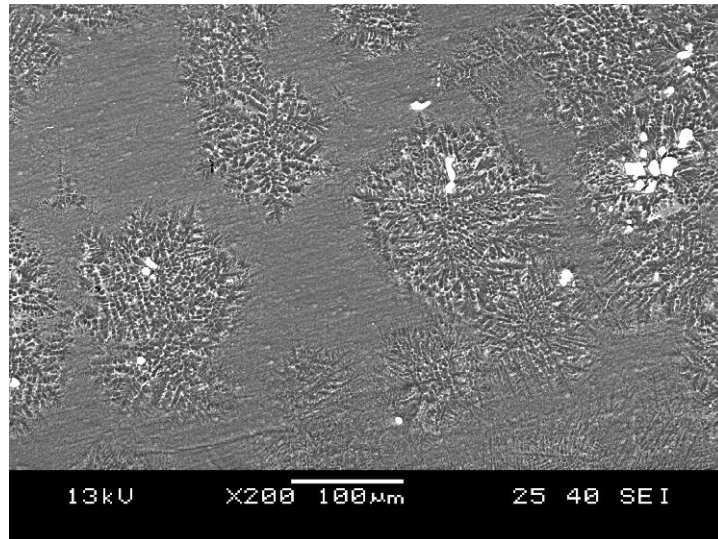


Fig. 4.6 SEM image of as-cast AZ31 alloy sheet in transverse section.

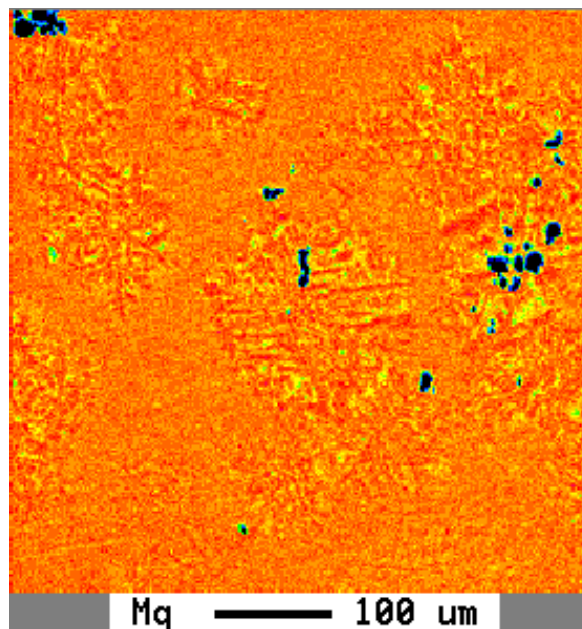


Fig. 4.7 EPMA mapping of Mg element distribution.

From Fig. 4.7 we can find that segregation of Mg formed at the equiaxed grains, whilst distributions of Mg in other regions were uniformly exist. In order to get more information about the uniformly area, a SEM image of this area was taken at higher magnification, as shown in Fig. 4.8.



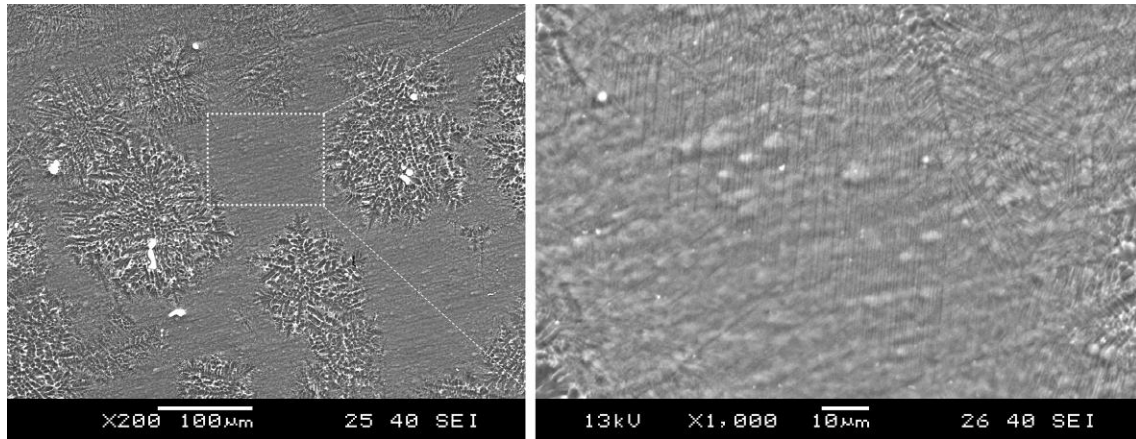


Fig. 4.8 SEM image of as-cast AZ31 alloy sheet in transverse section

The DAS of the 1.2mm thickness AZ31 alloy strip shown in Fig. 4.8 has the average value of  $0.7\mu\text{m}$ . Thus we can get a conclusion that the uniform distribution of Mg in this area due to the very fine dendrite. If the equation  $\lambda = 35.5R^{0.31}$  were suitable for the calculate of cooling rate, a value of  $2.5 \times 10^5 \text{ K}\cdot\text{s}^{-1}$  can get, it exhibits a quit fast cooling rate.

From the above discussion, we can get an conclusion that it is quite difficult to obtain a glassy state of AZ31 alloy even though we were trying to build a faster cooling rate hardly. Due to these, we tried the next alloy, i.e., AZ31-In-Sn alloy.

## (2) AZ31-In-Sn alloy

An as-cast slice in thickness of 0.4 mm was produced by the rapid solidification TRC process. The formation of the small slice due to a very small amount of mass was used during the casting process. Fig. 4.9 shows the SEM image of the cross section of the AZ31-In-Sn alloy slice. It shows an average secondary dendrite arm spacing (DAS) of about  $1.2 \mu\text{m}$ . Then a cooling rate of  $5.56 \times 10^4 \text{ K}\cdot\text{s}^{-1}$  can be calculated. Fig. 4.10 shows the SEM image of the cross section near the slice surface. There are a number of fine grains in sizes of  $0.5\sim 2 \mu\text{m}$  due to the effect of chilling. Although a narrow DAS at

the center of the slice and fine grains near the surface of the slice formed during the rapid cooling process, it still formed a crystalline phase under such a limit condition of the twin roll caster. Formation of noncrystalline phase by rapid solidification of TRC process seems to be also impossible for this alloy.

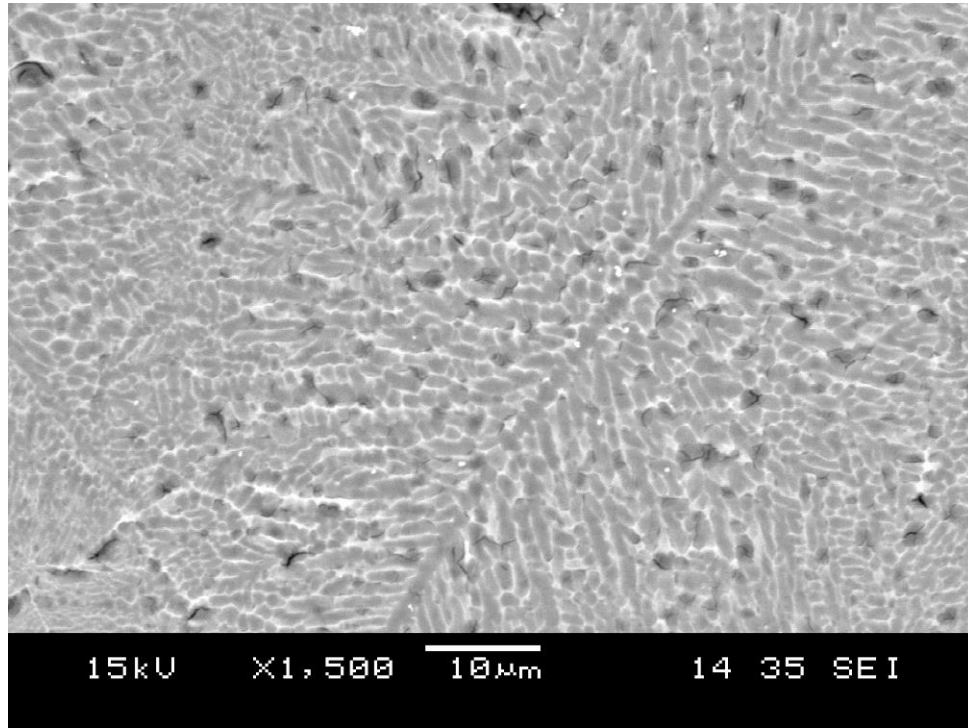


Fig. 4.9 SEM images of as-cast AZ31-In-Sn alloy sheet in transverse section at mid-thickness.

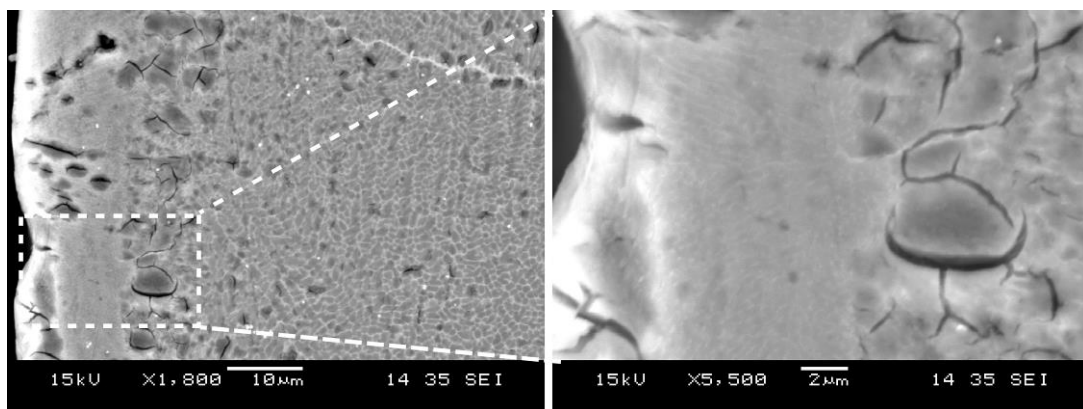


Fig. 4.10 SEM images of as-cast AZ31-In-Sn alloy sheet in transverse section near surface.

In order to further confirm the above conclusion, the AZ31-In-Sn alloy was melted

and produced by the melt spinning method. Mg element distribution map of the as-cast AZ31 alloy slice specimen was recorded by electron probe micro-analysis (EPMA), as shown in Fig. 4.11. We can see that the ribbon has a thickness of 0.35  $\mu\text{m}$ . As shown in Fig. 4.11(a), the right side of the ribbon is the metal-roll contact surface, and the left side is the free surface. Segregations generated across the transverse section. These confirm the conclusion that formation of noncrystalline phase of the AZ31-In-Sn needs a very large cooling rate. It may due to the small values of atomic sizes difference between the alloying elements and Mg.

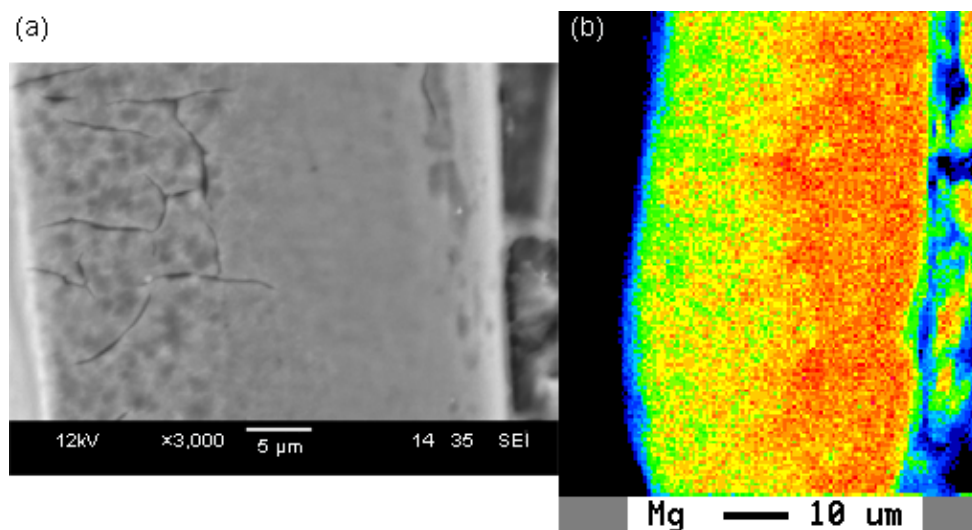


Fig. 4.11 SEM image (a) and EPMA mapping of Mg element distribution (b) of AZ31-In-Sn alloy ribbon produced by melt spinning method.

### (3) Mg-RE alloy

An as-cast strip in thickness of 1.1mm and width of 70mm of Mg-RE alloy was produced by the rapid solidification TRC process. Fig. 4.12 and Fig. 4.13 show the optical microstructures of the Mg-RE alloy sheet. SEM images of the same part are shown in Fig. 4.14 and Fig. 4.15. The microstructure is mainly characterized by fine equiaxed grains and dendrites with closely spaced secondary dendrite arms. Meanwhile, there are some special areas which do not reveal any crystalline features under the

optical observation (the red arrows). We name them *quasi-amorphous* solids for the moment here and the structure will be tested by the following X-ray diffraction (XRD) and Transmission electron microscopy (TEM) analysis. Critical cooling rate for forming metallic glass with the composition of the quasi-amorphous phase regions is lower than that of the crystalline phase regions, in other words, glass forming ability (GFA) of the former is better.

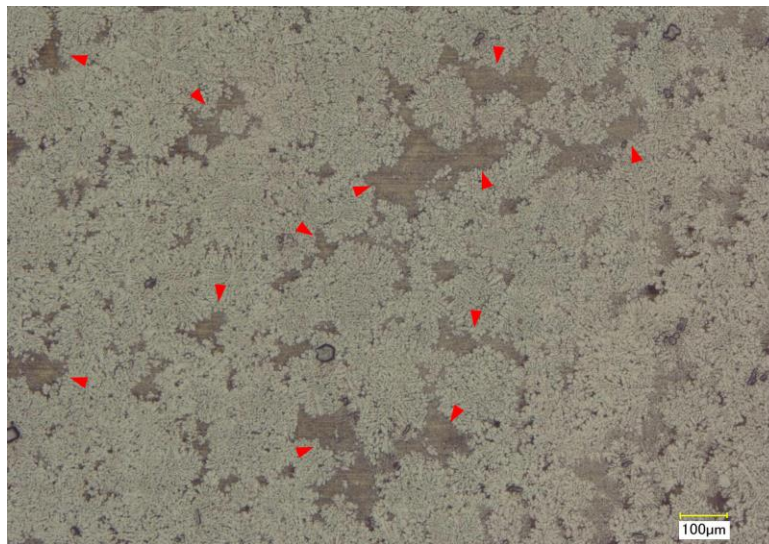


Fig. 4.12 Optical microstructure of the Mg-RE alloy sheet



Fig. 4.13 Optical microstructure of the Mg-RE alloy sheet—large quasi-amorphous phase.



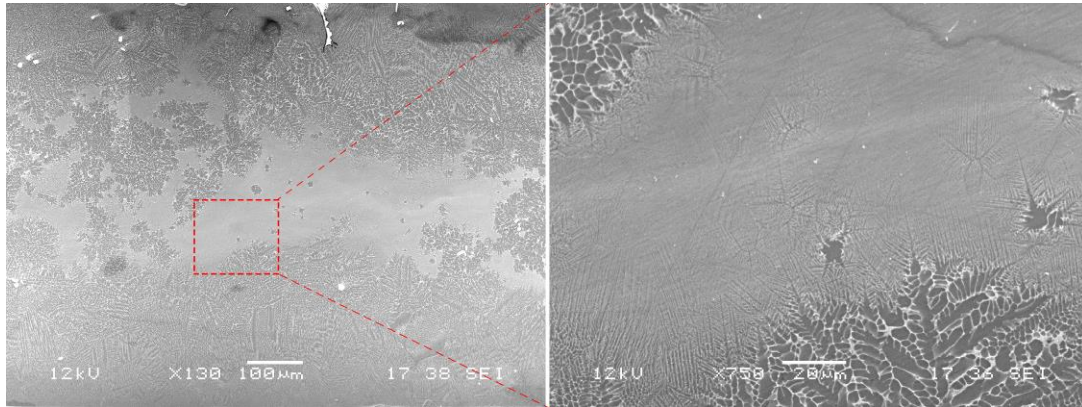


Fig. 4.14 SEM images of the Mg-RE alloy sheet—large quasi-amorphous phase.

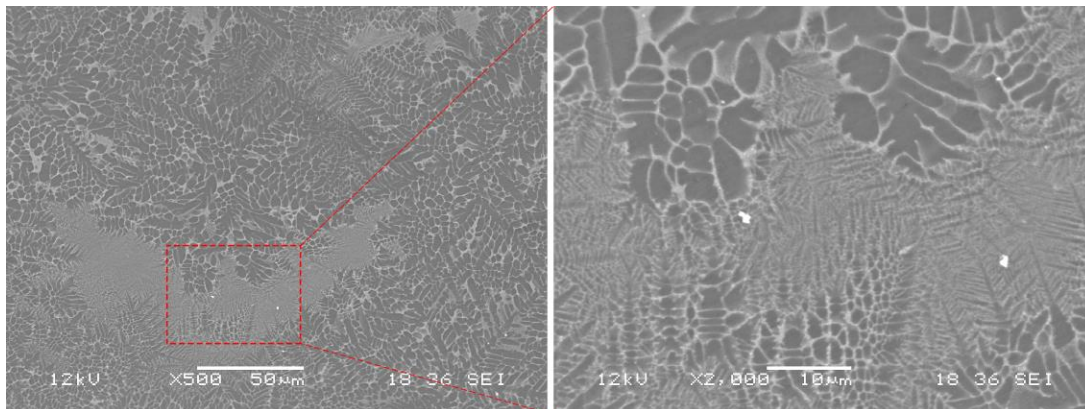


Fig. 4.15 SEM images of the Mg-RE alloy sheet—small quasi-amorphous phase.

The quasi-amorphous phases are surrounded by dendrites and fine grains. The areas of these phases are different, i.e., they are in different sizes. As shown in Fig. 4.14, areas of the large quasi-amorphous phases have a maximum incircle diameter of about 100  $\mu\text{m}$ . While for those areas with small phases, the maximum incircle diameter is about 50  $\mu\text{m}$  or less, as shown in Fig. 4.15. Dendrites around the quasi-amorphous phases are extraordinarily fine and their growth is prevented by the quasi-amorphous phases.

Elements distribution maps of the Mg-RE alloy sheet sample were recorded by electron probe micro-analysis (EPMA), as shown in Fig. 4.16 and Fig. 4.17. On the one hand, element segregation exists between the crystalline phase matrix and the

quasi-amorphous phases. On the other hand, it is said that grain boundary segregation forms easily as the atomic size difference (ASD) between Mg and alloying element is larger than 10% [5]. As the atomic sizes between Mg-Al, Mg-La, Mg-Ce, Al-La and Al-Ce are quite different, dendritic segregations also generate in the crystalline matrix.

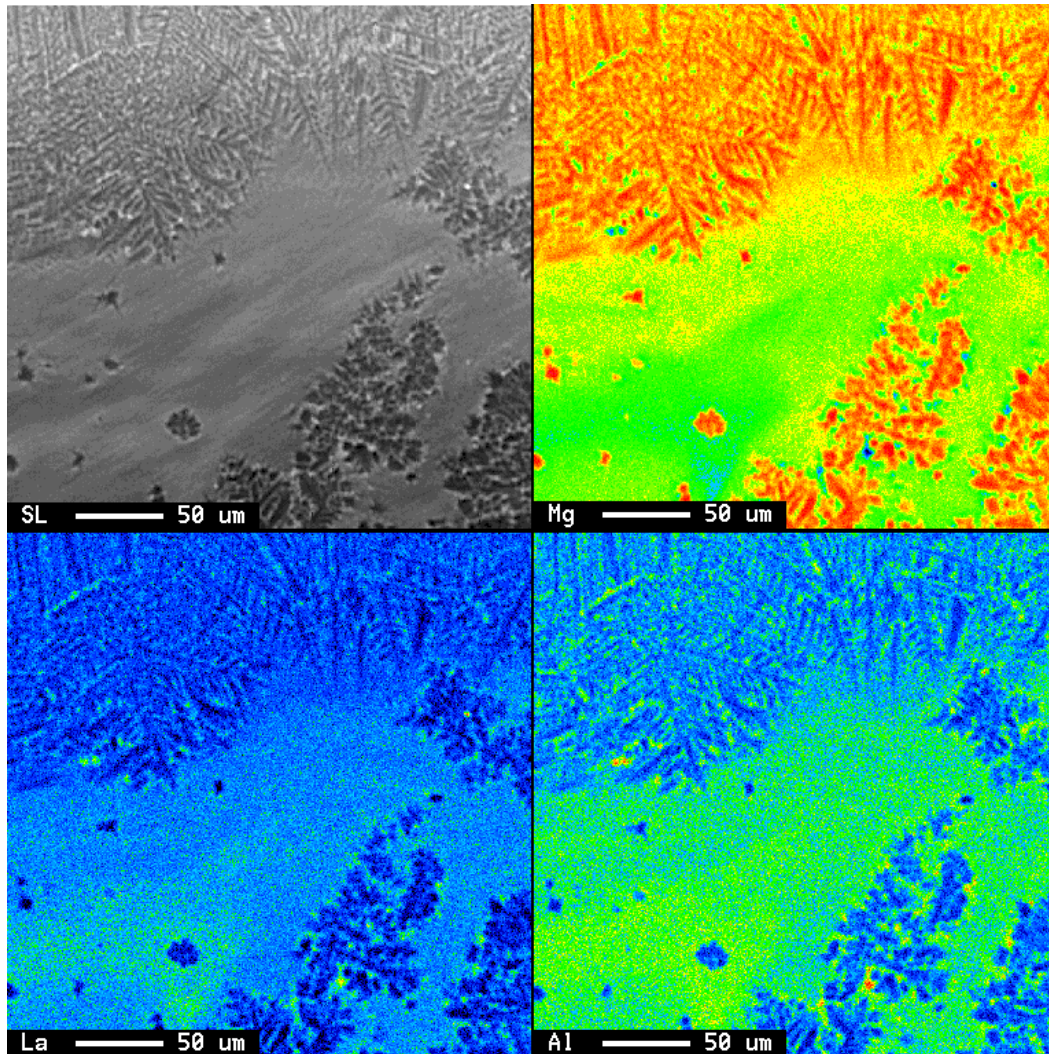


Fig. 4.16 EPMA mapping of the Mg-RE alloy sheet—large quasi-amorphous phase.

Microstructure characteristic of the quasi-amorphous phase and its surroundings is illustrated in Fig. 4.18. *A zone* shows the crystalline matrix with fine equiaxed grains and dendrites, segregation of elements occurs at the grain boundaries and dendrite spaces. *B zone* illustrates fine dendrites with closely spaced secondary dendrite arms



distributed around a large quasi-amorphous phase. Element segregation of this zone decreased due to the fine dendrites. *C zone* indicates the quasi-amorphous phase, elements uniformly distribute in this phase. It contains a low amount of Mg comparing to the crystalline matrix. Contrarily, the amount of Al and La is relatively large. Few nuclei can be found inside the quasi-amorphous phase, their growths are restricted and the final sizes are less than 20  $\mu\text{m}$ .

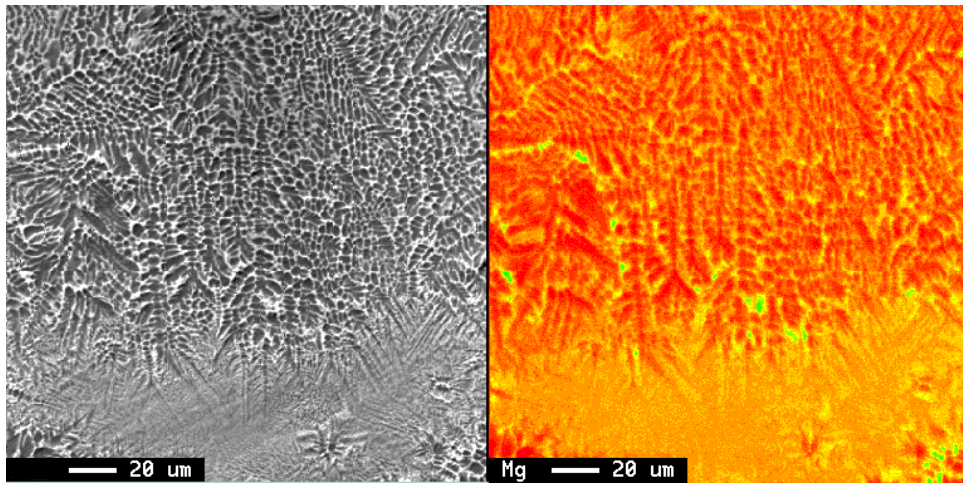


Fig. 4.17 EPMA mapping of the Mg-RE alloy sheet—small quasi-amorphous phase and its surroundings.

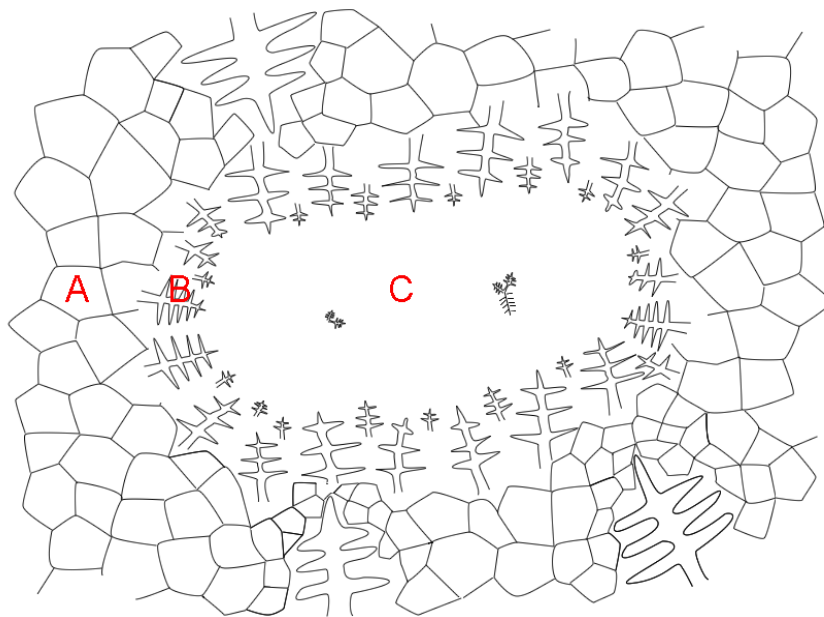


Fig. 4.18 Schematic illustration of microstructure characteristic of the quasi-amorphous phase and its surroundings.

### 4.2 X-ray diffraction analysis

X-ray diffraction (XRD) technique is commonly used because it gives information about the structure of solids and permits nondestructive structure analysis.

#### (1) $2\theta/\omega$ scan

Samples using for XRD analysis were taken from the as-cast Mg-RE alloy sheet with a thickness of about 0.9mm. Microstructures taken by optical microscope are shown in Fig. 4.19. At the surface of the as-cast sheet, Fig. 4.19(a), grains are very fine which have an average grain size about  $2.5\mu\text{m}$ . At the mid-thickness of the as-cast sheet, grains sizes become larger, about  $3\sim 6\mu\text{m}$  as shown in Fig. 4.19(b). From Fig. 4.19(b) and (c) we can see that the *quasi-amorphous* solids (indicated by red arrows) located in the crystalline matrix and coexist with the matrix grains. Around the quasi-amorphous phases, the matrix is formed by small dendrites and the growth of the dendrites is restricted by the quasi-amorphous phases.

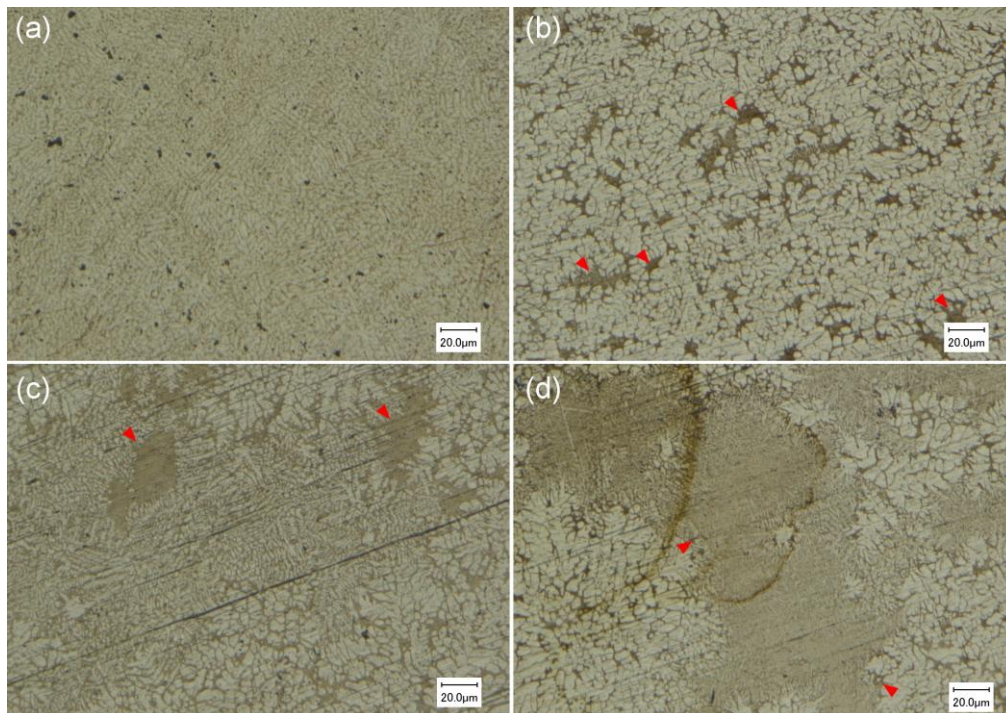


Fig. 4.19 Microstructure of the as-cast Mg-RE alloy: (a) surface; (b), (c) and (d) mid-thickness.



Results of XRD analysis are shown in Fig. 4.20. Using these XRD patterns, crystallite size of each detected phase could be calculated by the Scherrer equation. The equation is expressed by  $D_{hkl} = K\lambda/B_{hkl} \cos\theta$  <sup>[6]</sup>, where  $D_{hkl}$  is the crystallite size in the direction perpendicular to the lattice planes,  $hkl$  are the Miller indices of the planes being analyzed,  $K$  is a numerical factor frequently referred to as the crystallite-shape factor,  $\lambda$  is the wavelength of the X-rays,  $B_{hkl}$  is the width (full-width at half-maximum) of the X-ray diffraction peak in radians and  $\theta$  is the Bragg angle. The calculated results are listed in Table 4.1, Table 4.2 and Table 4.3. It can be found that the grain sizes are very small. And this further explains the existence of the very fine grains around the quasi-amorphous phases as shown in Fig. 4.19(c).

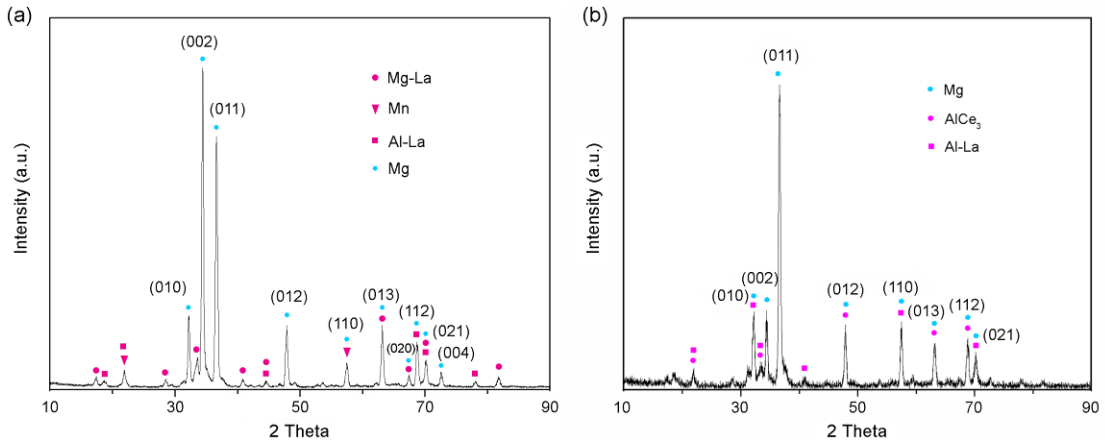


Fig. 4.20 XRD pattern of the as-cast sheet: (a) surface; (b) mid-thickness.

Table 4.1 Crystallite sizes at the as-cast sheet surface calculated by Scherrer equation (Mg).

(hkl)	(010)	(002)	(011)	(012)
$D_{hkl}/\text{nm}$	59.71988	30.63795	41.25575	41.14509

Table 4.2 Crystallite sizes at the as-cast sheet mid-thickness calculated by Scherrer equation (Mg).

(hkl)	(010)	(002)	(011)	(012)	(110)
$D_{hkl}/\text{nm}$	11.93841	24.45067	13.97384	18.84977	13.41517

Table 4.3 Crystallite sizes at the as-cast sheet mid-thickness calculated by Scherrer equation (Al-La).

(hkl)	(101)	(202)	(303)	(224)	(321)
$2\theta$	21.9636	44.7067	68.9229	70.1493	78.1329
$D_{hkl}/\text{nm}$	13.60109	11.6459	57.52747	30.4624	40.24124

(2) Micro area X-ray diffraction ( $\mu$ -XRD) —  $2\theta$  scan

As the results shown in Fig. 4.19, areas of the quasi-amorphous phase are small (approximately  $\Phi 50\mu\text{m}$  at maximum). The line focus side of the X-ray tube is not suitable for analyzing such small areas because the line focus is typically 0.1 to 0.2 mm wide and 8 to 12 mm long <sup>[7]</sup>. Besides, irradiated region of the sample is uncertain. In order to solve these problems, micro area X-ray diffraction technique is adopted to analyze the structure of quasi-amorphous solids. In this technique, the position sensitive proportional counter (PSPC) with a  $2\theta$  range of  $5^\circ \sim 155^\circ$  is used to simultaneously detect diffracted rays generated at different angular positions, as shown in Fig. 4.21. The measuring point is located at the intersection of the three axes, i.e.,  $\omega$  axis,  $\chi$  axis, and  $\Phi$  axis. Testing area can be confirmed by an attached optical microscope. A collimator in diameter of 0.03mm is fixed to the point focus side of the X-ray tube at the current work. Thus, a very small area could be analyzed without reflecting structure information of needless areas.

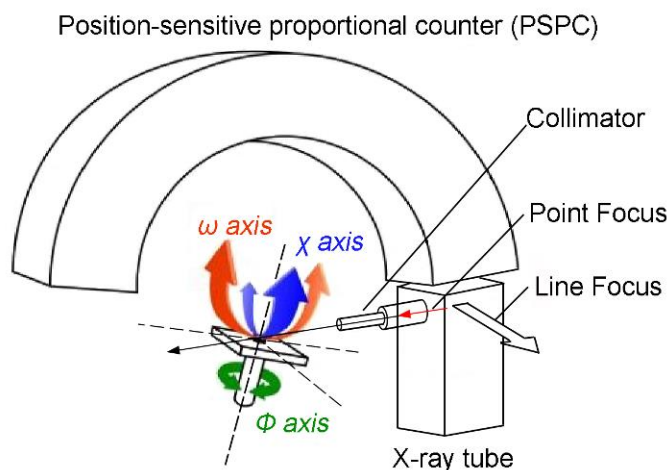


Fig. 4.21 Illustration of micro area X-ray diffraction.

Microstructures of the as-cast sheet sample used for  $\mu$ -XRD analyses are shown in Fig. 4.22. Their  $\mu$ -XRD patterns are represented in Fig. 4.23. In Fig. 4.23(a), there is a peak in the quasi-amorphous phase  $\mu$ -XRD pattern at  $2\theta=57.4^\circ$ , which may cause by

that the area of tested region was smaller than collimated incident beam ( $\Phi=0.03$  mm) and some of the crystalline phase information was mixed in it, as the regions marked with polygons shown in Fig. 4.22. Another reason of the peak is the find dendrites existed in the large quasi-amorphous solids, as shown in Fig. 4.14. In Fig. 4.23(b), the crystalline phase  $\mu$ -XRD pattern exhibits only one peak at  $2\theta=68.4^\circ$ ; this may due to the detection area contains a single crystal and a small quasi-amorphous phase, as the regions marked with rounded rectangles shown in Fig. 4.22. Considering the XRD patterns shown in Fig. 4.20, the peaks mentioned above may be identified as Mg phases with miller indices  $(11\bar{2}0)$  and  $(11\bar{2}2)$ , which has a  $2\theta$  value of  $57.4^\circ$  and  $68.4^\circ$  respectively. As listed in Table 4.4, possible phases of the above two peaks stand for are presented.

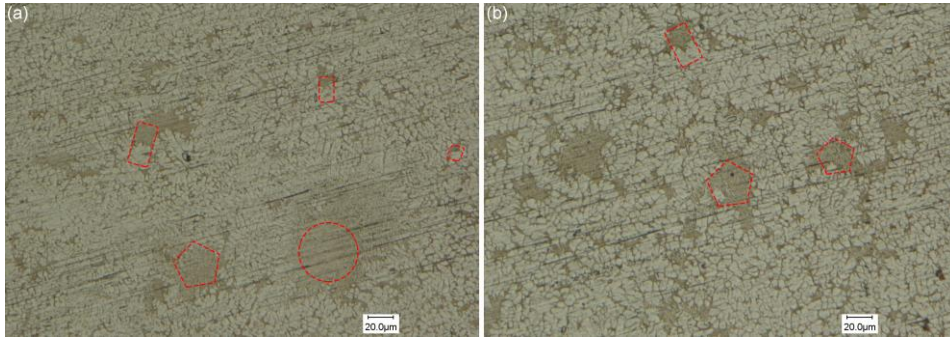


Fig. 4.22 Microstructures of as-cast sheet sample used for  $\mu$ -XRD analyses: (a) and (b) shows microstructures at different locations.

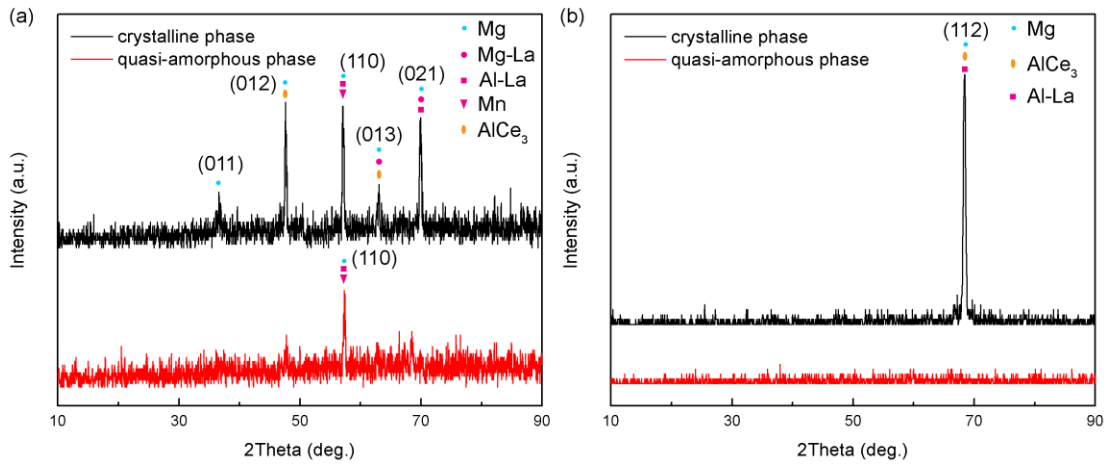


Fig. 4.23  $\mu$ -XRD patterns of the as-cast sheet mid-thickness: (a) small quasi-amorphous phase with crystalline structure; (b) large quasi-amorphous phase without crystalline structure.

## Chapter 4 TRC experiment and microstructure analyses

Table 4.4 Possible phases of the two peaks: peak at  $2\theta=57.4^\circ$  of the quasi-amorphous phase pattern and peak at  $2\theta=68.4^\circ$  of the crystalline phase pattern.

$2\theta$		Mg	Mn	Al-La	Al-Ce
$57.4^\circ$	Crystal system	Hexagonal	Cubic	Orthorhombic	
	(hkl)	(110)	(331)	(055)	
$68.4^\circ$	Crystal system	Hexagonal		Tetragonal	Hexagonal
	(hkl)	(112)		(303)	(004)

\*When a plane is specified using four indices (hkil) where the third index is always the negative of the sum of the first two, i.e.,  $i=-(h+k)$ .

### 4.3 TEM analysis

#### 4.3.1 Sample preparation by focused ion beam (FIB) milling technique

The FIB equipment we used for preparing TEM samples is JIB-4500 Multi Beam system. And the sample making process is illustrated in Fig. 4.24. As an initial work of specimen preparation, the as-cast sheet was cut into a size of  $10\text{mm}\times 10\text{mm}$ . After thinning the slice thickness to about  $30\mu\text{m}$ , a  $1.5\text{mm}\times 1.5\text{mm}$  foil was cut off and glued on a Mo grid. Then the sample was further cut by FIB and the final shape of the sample was shown in Fig. 4.24(b).

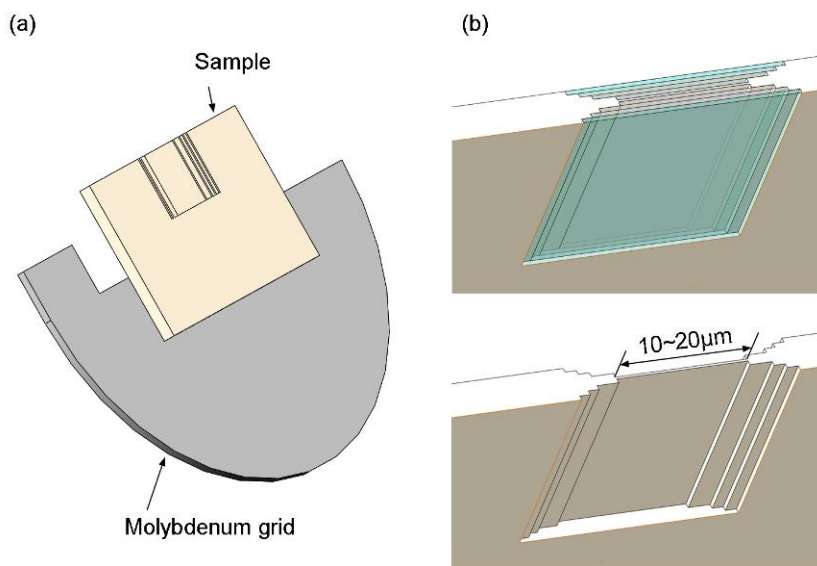


Fig. 4.24 Schematic illustration of TEM sample

The milling processes by FIB method was shown in Fig. 4.25. The sample was milled into stair-step shape initially and finally it was milled down to a thickness of 0.1  $\mu\text{m}$ .

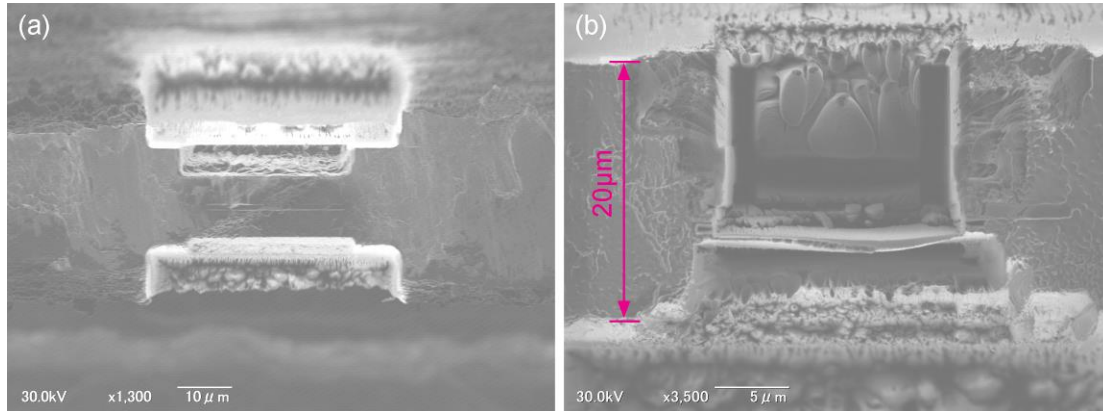


Fig. 4.25 Specimen preparation by FIB technique.

In order to analysis the quasi-amorphous phase in the Mg-RE alloy sheet, we have prepared many initial specimens for FIB process. Because the quasi-amorphous phases in the current material are in a size scale of micro degree, finding a right area with quasi-amorphous phase was an arduous task. Fig. 4.26(a) shows a small quasi-amorphous phase we found, and the SEM image of the final specimen we made is shown in Fig. 4.26(b).

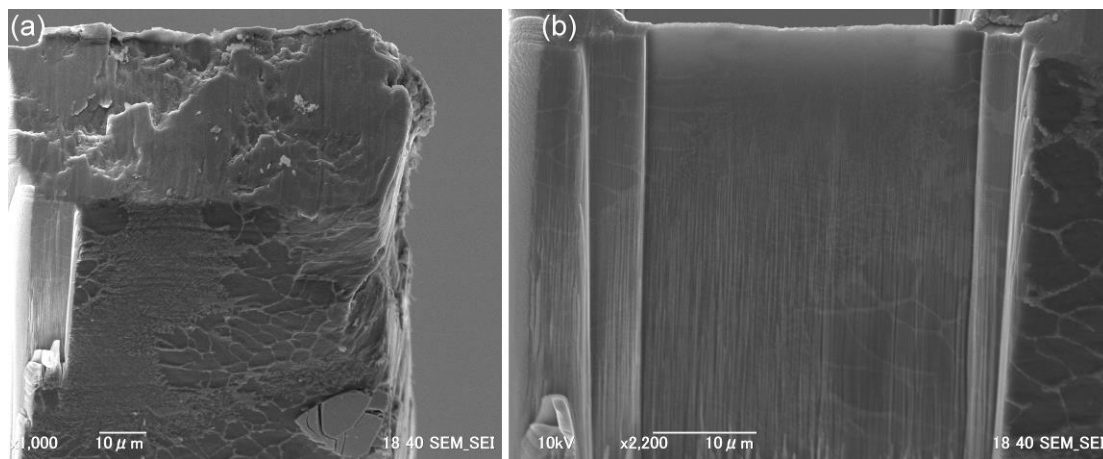


Fig. 4.26 TEM specimen: (a) before FIB processing; (b) after FIB processing.

#### 4.3.2 TEM analysis results

From the selected area diffraction pattern, d-spaces corresponding to the rings could be calculated by the following equation <sup>[8]</sup>:

$$Rd = L\lambda \quad (4-2)$$

where R is the distance of any reflections from the center of pattern, d is the interplanar spacing, L is the effective camera length,  $\lambda$  is the wave length of the incident beam.

TEM image of the as-cast Mg-RE alloy was shown in Fig. 4.27. Inset is SAED pattern of the grain. The grain is a Mg crystal in a grain size of about 5  $\mu\text{m}$ . In the model we proposed in Fig. 4.18, the Mg crystal expresses the A zone.

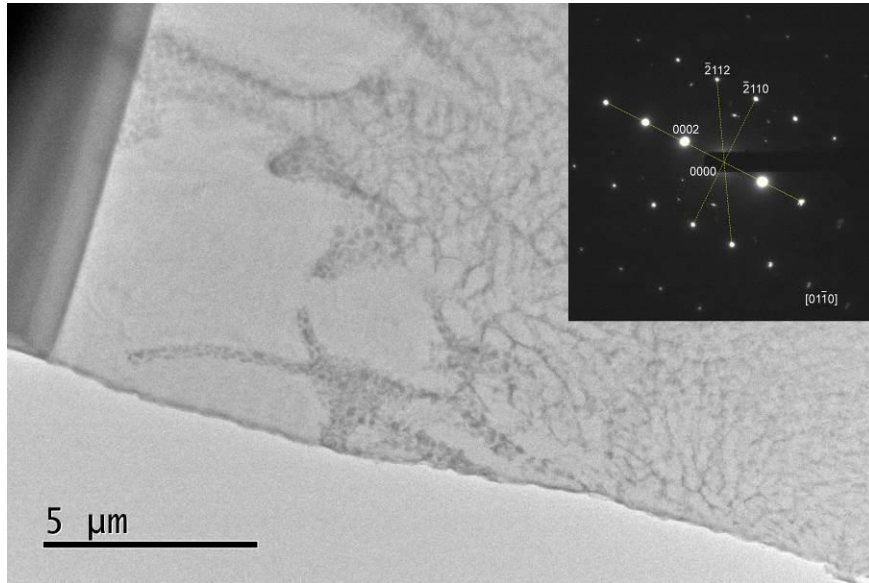


Fig. 4.27 TEM image of the as-cast Mg-RE alloy. Inset, SAED pattern of the grain.

As shown in Fig. 4.28, it is the TEM image of B zone expressed in our model. This image shows the very fine grains with average grain size of about 0.5  $\mu\text{m}$ . It was identified as Mg-La phase by the SAED pattern.



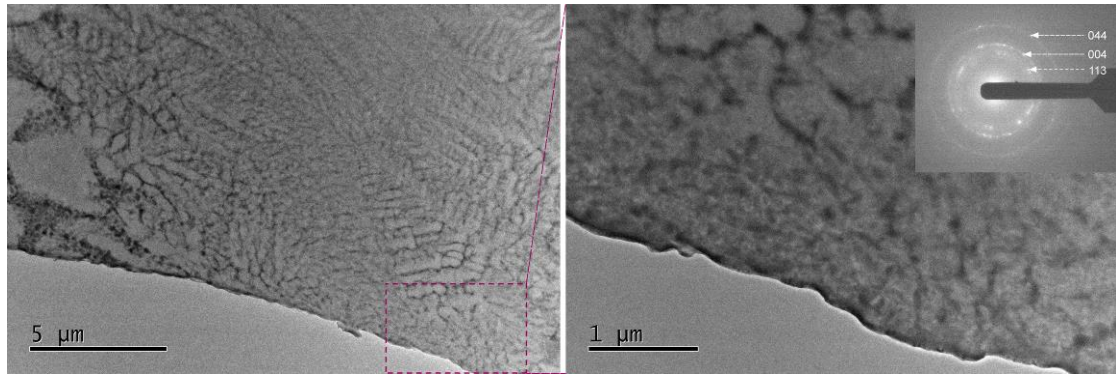


Fig. 4.28 TEM image of the as-cast Mg-RE alloy— $\text{La}_8\text{Mg}_{16}$  phase. Inset, SAED pattern.

TEM image of a Mg grain and its grain boundary and the corresponding SAED pattern was shown in Fig. 4.29. The Mg grain size is about 7  $\mu\text{m}$ . Near the grain boundary, there also exist an amount of very fine grains with size of about 0.3  $\mu\text{m}$ . And these grains were identified as Mg-La phase and Al-La phase. It seems that these two phase precipitated at the grain boundaries of Mg during the rapid speed solidification.

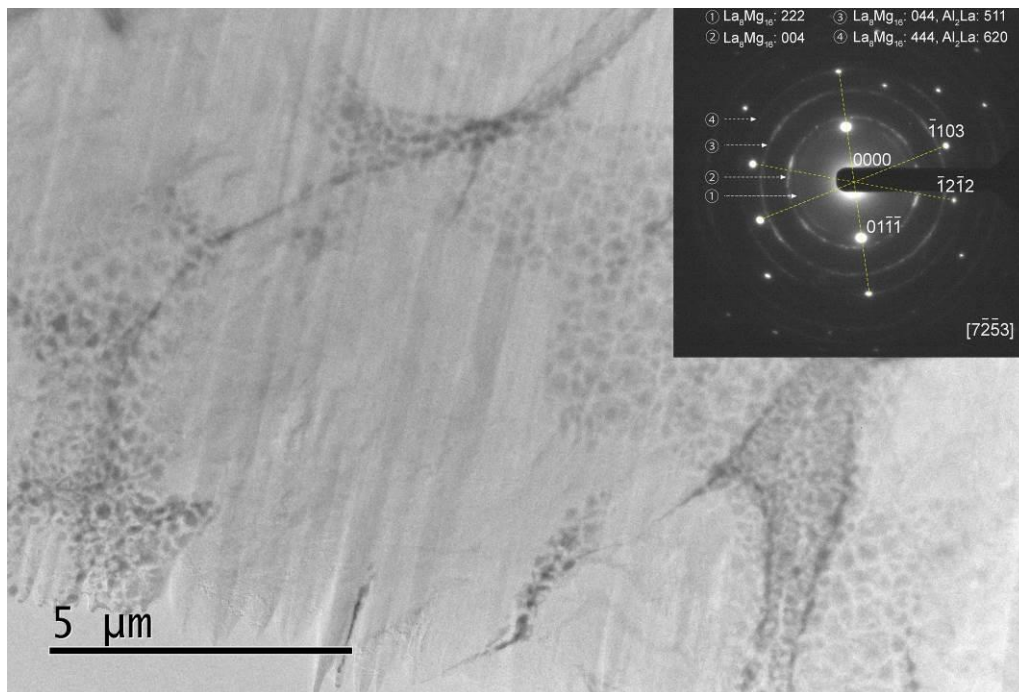


Fig. 4.29 TEM image of the as-cast Mg-RE alloy—Mg grain and La-Mg, Al-La phase at grain boundary. Inset, SAED pattern.

The border of B and C zone expressed in our model was shown in Fig. 4.30. In B

zone, it expresses fine dendrites feature. In C zone, although some spots of electron diffraction exist, but it shows a poor crystallinity. This may due to the quasi-amorphous phase of the current TEM specimen was in a small size or the specimen was damaged during the FIB milling.

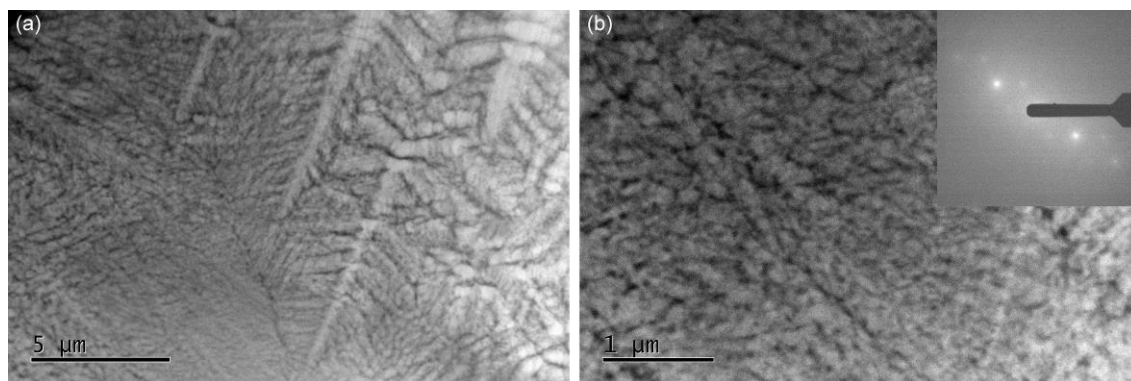


Fig. 4.30 TEM image of the as-cast Mg-RE alloy: (a) fine dendrites; (b) quasi-amorphous phase. Inset, SAED pattern.

### 4.4 Corrosion properties


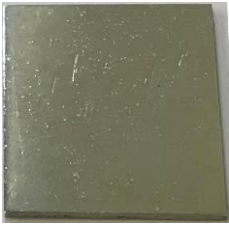
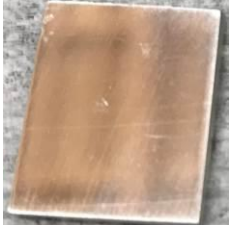



From the above analysis, it shows that only the Mg-RE alloy expressed the quasi-amorphous character which achieved the expected structure target at beginning, i.e., quasi-amorphous phased and fine crystalline phase dual-phase material. In order to evaluate the corrosion resistance of the Mg-RE alloy, corrosion tests were conducted. Considering the fine grains appeared at the surface of AZ31-In-Sn alloy, it was adopted as comparison. Also, we used AZ31 light battery sheet material as one more group of comparison.

Table 4.5 presents surface morphologies of the three kinds of alloys after immersed in 3.5% NaCl solution for 48h at 50°C. It is obviously shows that filiform and pitting corrosion are the main corrosion types. The AZ31 light battery sheet was corroded seriously and the original shape could not be retained. The surface of the AZ31-In-Sn sample produced by TRC exhibits a pitting corrosion. Abundant white corrosion



products accumulated in the corrosion pits. Only slight corrosion has occurred on the Mg-RE sample and no change could be detected by visual observation except for color. This corroborates the effect of RE on improving corrosion resistance.

Table 4.5 Surface states of the Mg alloy sheets before and after corrosion.

	AZ31 Light sheet	AZ31-In-Sn	Mg-RE
Before corrosion			
After corrosion			

### 4.4.1 Surface morphology of the AZ31 Light sheet after corrosion

The surface of the AZ31 light alloy is covered with corrosion product. As shown in Fig. 4.31(a), some parts of the specimen were corroded seriously and dissolved into the corrosion solution. Fig. 4.31(b) shows the corrosion status of the other regions. The loose and cracked corrosion products generated and vermicular expanded as immersion time gets longer. It shows filiform corrosion.

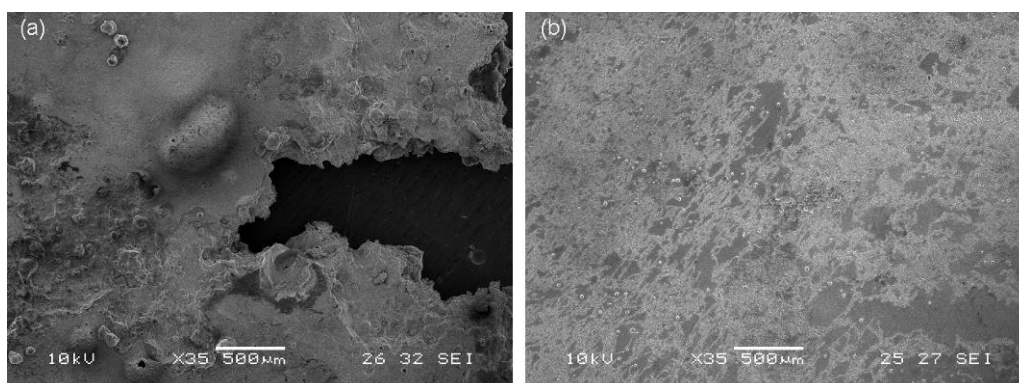


Fig. 4.31 SEM image of the AZ31 Light sheet after immersion.

As shown in Fig. 4.32, it shows the results of SEM image of the corrosion products (left) and distribution map of magnesium on the corroded surface after corrosion (right). It can be found that the content of Mg decreased with the generation of corrosion products. This also reflects that the corrosion layer contains less amount of Mg.

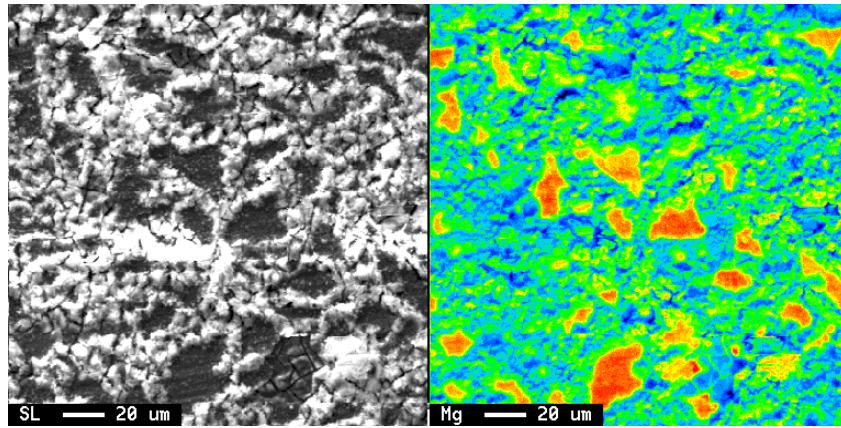


Fig. 4.32 Surface corrosion state and Mg element distribution after immersion—AZ31 Light sheet.

Optical microscopy image in the cross-section of the corroded specimen was shown in Fig. 4.33. It shows that the corrosion layer has a thickness of 10~20  $\mu\text{m}$ .

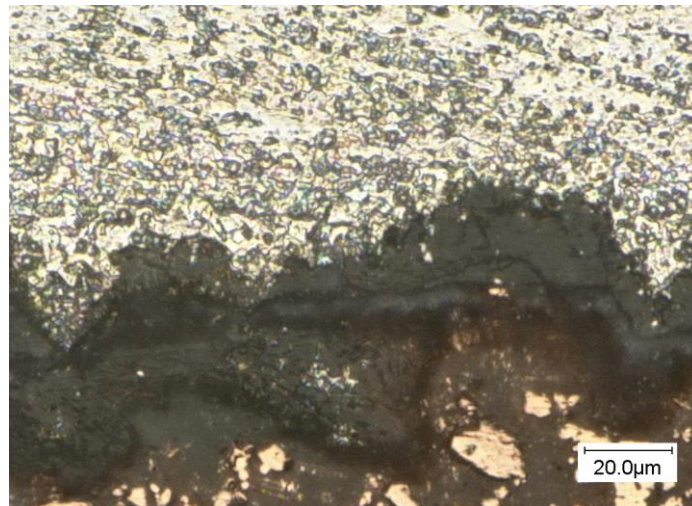


Fig. 4.33 Depth of the corrosion layer of the AZ31 Light sheet.

### 4.4.2 Surface morphology of the AZ31-In-Sn alloy sheet after corrosion

Pitting corrosion was observed on the surface of AZ31-In-Sn alloy sample. Loose

corrosion products accumulated in the corrosion pits and distributed on the sample surface non-uniformly, it suffered local attack during the immersion process. Fig. 4.34(b) shows the morphology of the slight corrosion region. Some white particles generated on the surface firstly and grow into large shape corrosion products over immersion time as shown in Fig. 4.34(a).

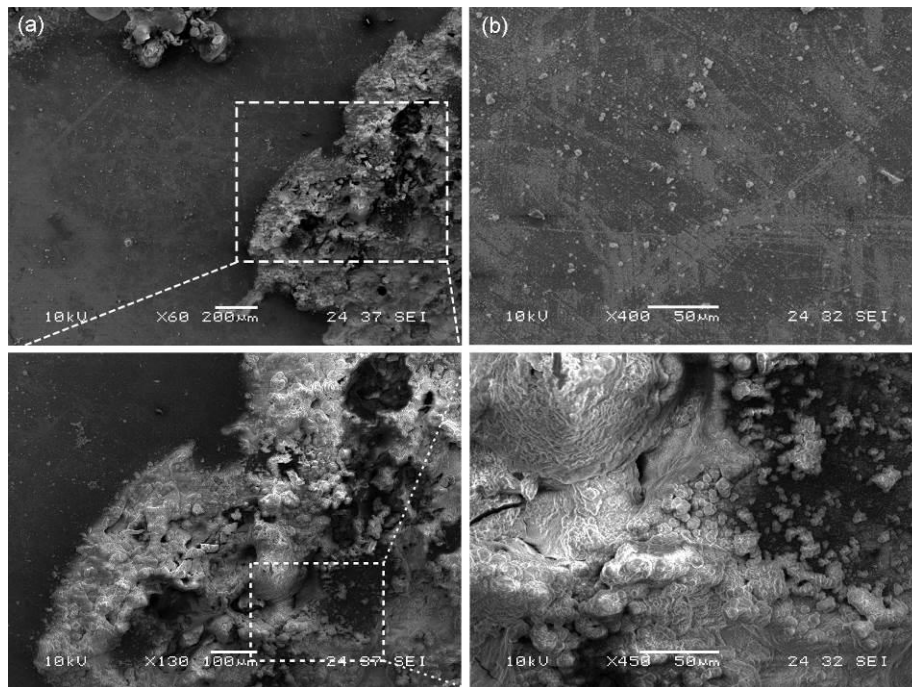


Fig. 4.34 SEM image of the AZ31-In-Sn alloy sheet after immersion: (a) severe corrosion region; (b) slight corrosion region.

SEM image of the corroded surfaces and distribution map of magnesium on the surface after corrosion were shown in Fig. 4.35. It has nearly the same phenomena as the AZ31 Light sample that the corrosion products contain a rare concentration of Mg.



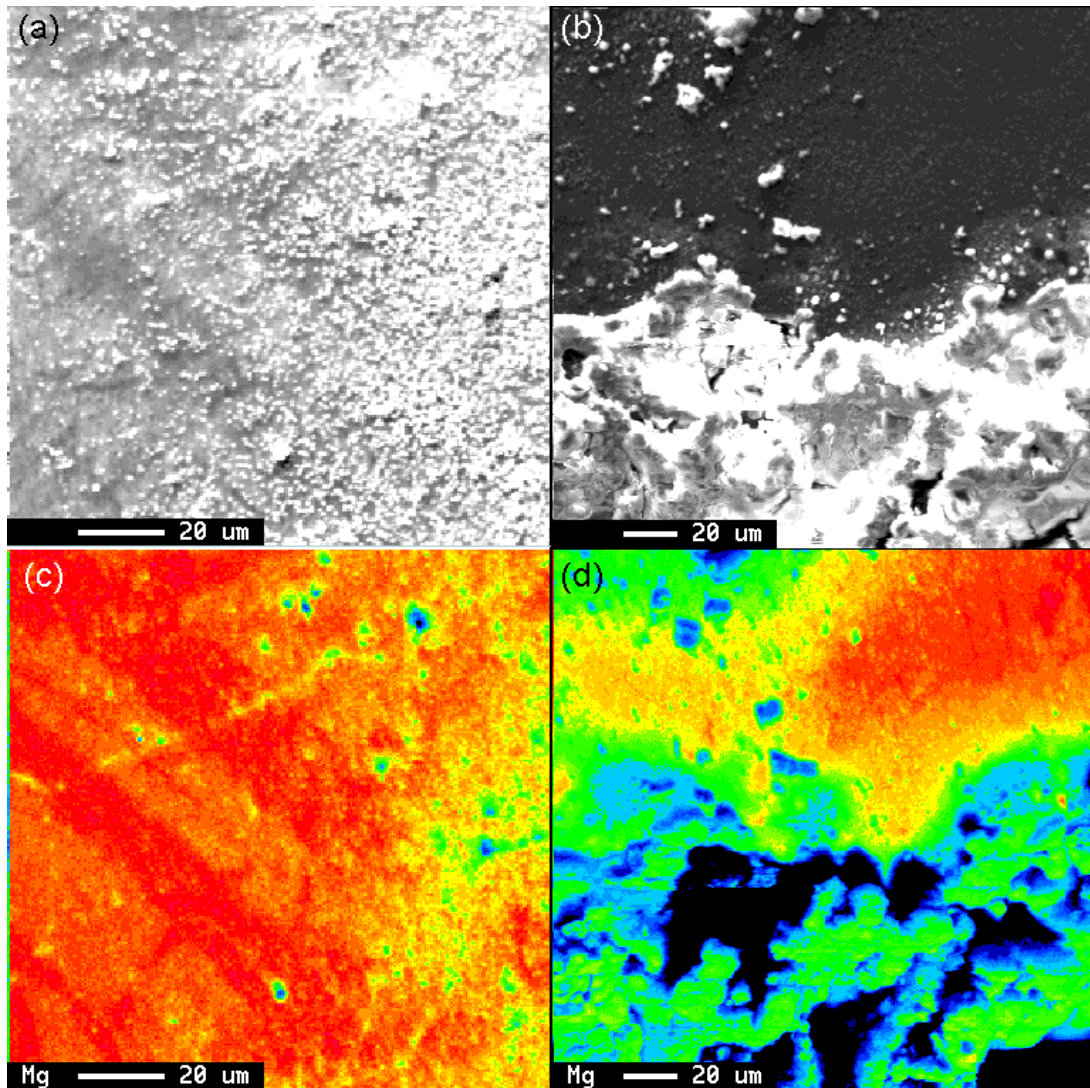


Fig. 4.35 Surface corrosion products and Mg element distribution after immersion—AZ31-In-Sn alloy sheet: slight corrosion region (a) and its corresponding EPMA Mg mapping (c); severe corrosion region (b) and its corresponding EPMS Mg mapping (d).

#### 4.4.3 Surface morphology of the Mg-RE alloy sheet after corrosion

Mg-RE alloy shows the best corrosion resistance among the current three alloys. As shown in Fig. 4.36, the grain boundaries can still be identified clearly after 48h immersion and only a very small amount of corrosion sites could be found. Grain boundary-like cracks generated at the black areas shown in Fig. 4.36(a) and make the sample surface appears local transgranular fracture. Fig. 4.36(b) shows the SEM image

in transverse section of the Mg-RE alloy specimen. The corrosion film is too thin to be detected.

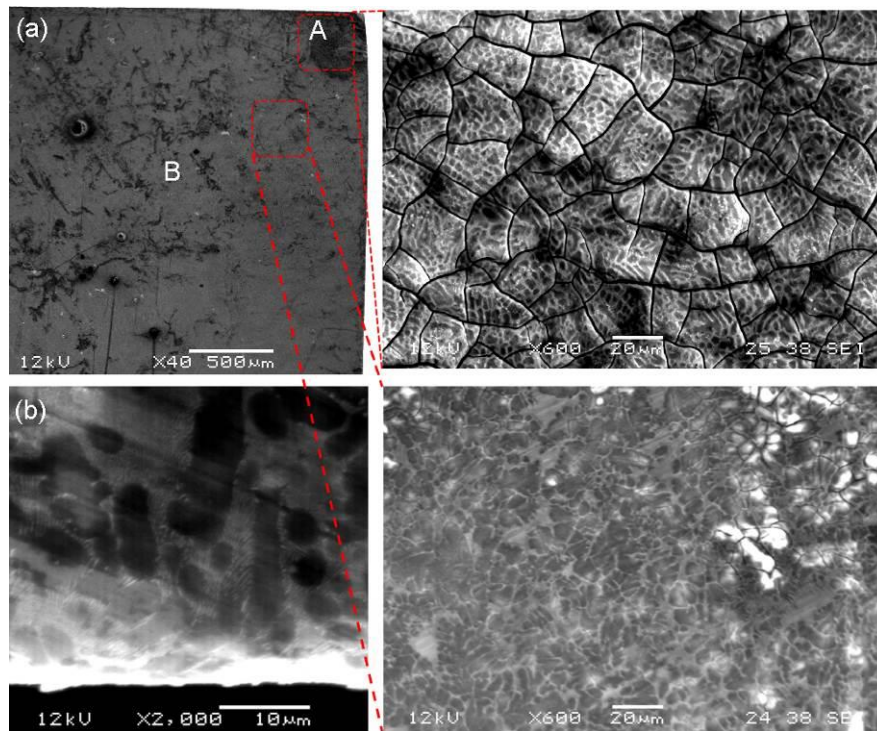


Fig. 4.36 SEM image of the Mg-RE alloy sheet after corrosion: (a) surface; (b) transverse section.

In order to evaluate the depth of the tiny cracks, the specimen was processed by FIB tool. SEM images of the prepared specimen were shown in Fig. 4.37. We can see that the tiny cracks generated after immersion have a depth of less than 1 μm.

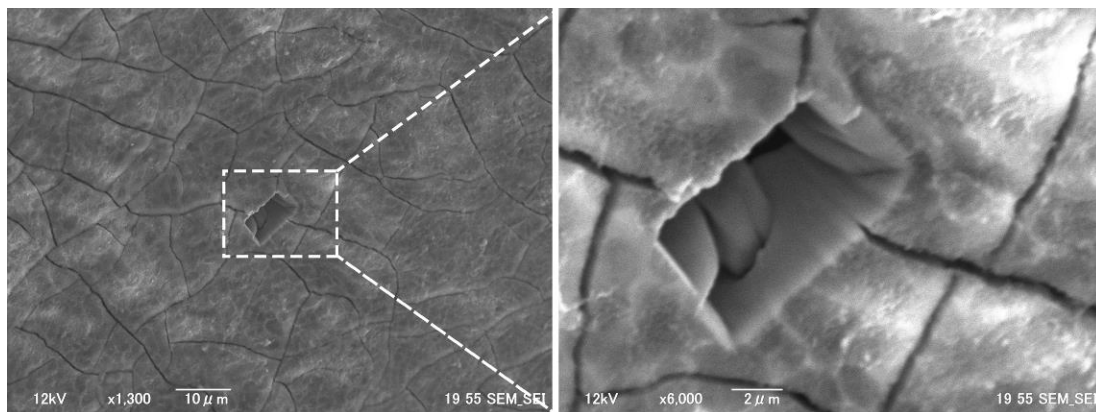


Fig. 4.37 Tiny crack depth of the corrosion layer.



As shown in Fig. 4.38, the SEM image of the Mg-RE surface (left) and element mapping of magnesium after immersion (right) were analyzed. We can find that magnesium content decreased in the surface with cracks.

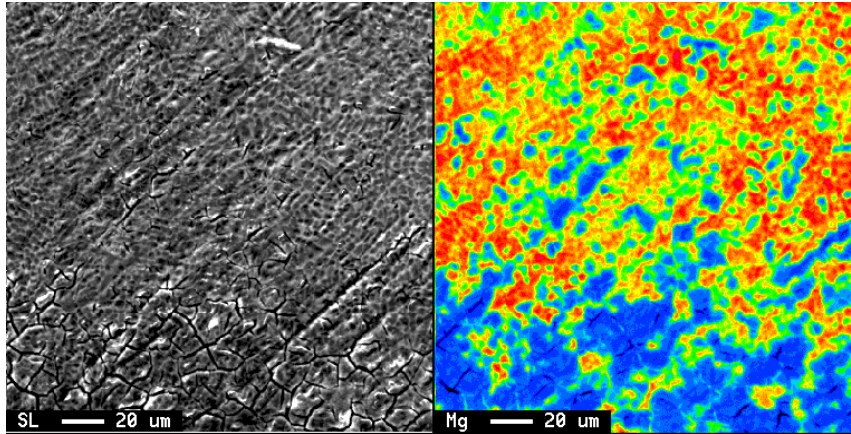


Fig. 4.38 SEM image and surface magnesium distribution of the Mg-RE sample after immersion.

### 4.4.4 Corrosion mechanism exploration

In order to find out the influence factors in corrosion resistance of Mg-RE alloy, details of the corrosion process were studied. Before this experiment, one more group of Mg-RE alloy sheet was produced by normal TRC under the casting speed of 10rpm. Fig. 4.39 shows the microstructure of the normal as-cast Mg-RE alloy. We can find that mean grain size of is about 20 $\mu$ m, and the chilled layer at surface has grain sizes in the range of 5~15 $\mu$ m.

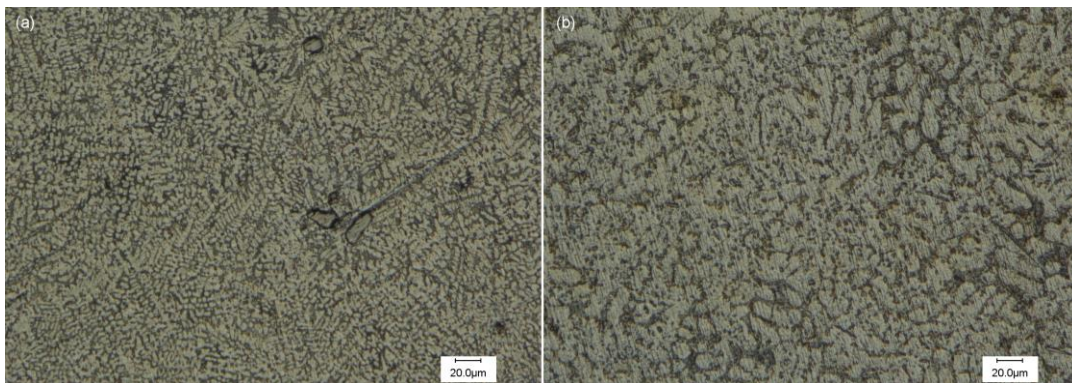
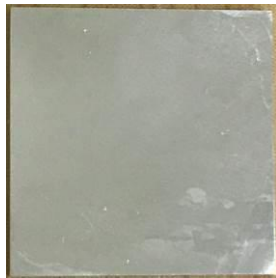

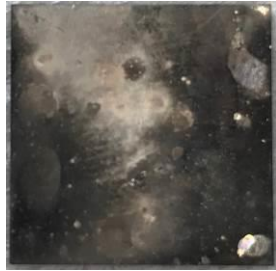





Fig. 4.39 Optical microstructure of Mg-RE alloy with casting speed of 10rpm: (a) surface; (b) mid-thickness.

## Chapter 4 TRC experiment and microstructure analyses

Surface morphological features of the two as-cast strips at each period of corrosion process are listed in Table 4.6. Masses of the specimens were weighed after drying.

Table 4.6 Morphological features of the surface of two as-cast Mg-RE alloy strips

	Mg-RE TRC strip — 10rpm Normal vertical TRC	Mg-RE TRC strip — 30rpm Rapid solidification of TRC
Size	14.35mm×14.45mm×0.95mm	13.20mm×13.65mm×0.70mm
Surface area	469.435mm <sup>2</sup>	397.95mm <sup>2</sup>
Microstructure features	Mean grain size of 20μm Chilled layer grain sizes are 5~15μm	Grain size less than 6μm Crystalline phase and quasi-amorphous phase
Before corrosion		
	Mass: 0.3287g	Mass: 0.2166g
24h / 50°C		
	Mass: 0.3291g	Mass: 0.2166g
48h / 50°C		
	Mass: 0.3289g	Mass: 0.2165g

From the above table we can find that the masses of the two samples had no significant change during the corrosion test. Comparing with the specimen made by

rapid solidification process (i.e., casting speed of 30 rpm), surface color of the specimen produced by normal TRC process (i.e., casting speed of 10 rpm) is darker after each corrosion step and the percentage of the dark area is larger.

As the photos shown in Table 4.6, the dark parts were seriously corroded comparing with the bright parts. Transition layer between the dark and bright regions of the specimen produced by rapid solidification process was characterized by EPMA. Fig. 4.40 shows the elements distribution of the sample surface after immersing in 3.5% NaCl solution for 48h. The content of magnesium decreased as the corrosion degree increased. On the other hand, the corrosion products contain a large amount of aluminum and a little lanthanum and cerium.

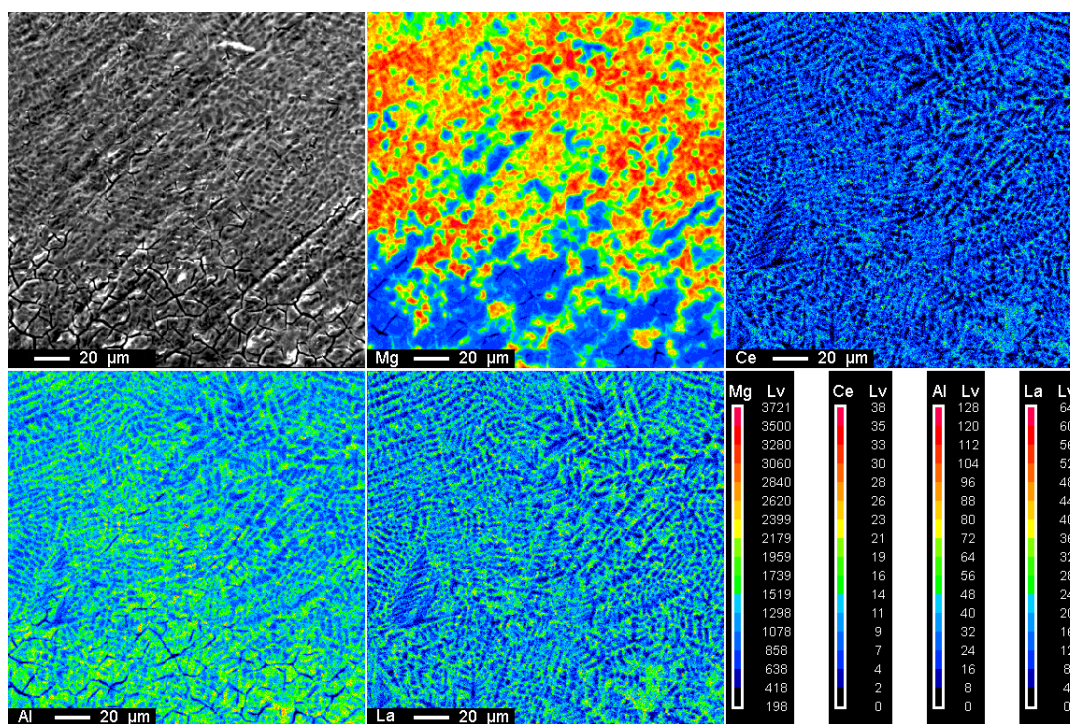


Fig. 4.40 Elements distribution after corrosion (30 rpm)

Concentrations of the metal ions in the solutions after immersion were analyzed by an Inductively Coupled Plasma (ICP) Emission Spectroscopy (ICPS-7000 Sequential Plasma Spectrometer, SHIMADZU Corporation). The results were listed in Table 4.7.



Magnesium content in the corrosion solution increases as the immersion time gets longer. On the contrary, concentration of aluminum decreased over immersion time. Considering the elements distribution states of the sample surface after corrosion test shown in Fig. 4.40, we can get a conclusion that the decrease of aluminum in corrosion solution may cause by the generation of corrosion products on the sample surface. From Table 4.7 we can also find out that magnesium content in the corrosion solution of the sheet produced by rapid solidification method is lower than the one produced by normal TRC method. This may due to the special texture formed under rapid cooling. The sheet produced by rapid solidification process exhibits an improved corrosion resistance.

Table 4.7 Metal ions concentrations after immersion.

Cooling method	Time / h	Concentration / ppm (1 ppm = 1 mg/l)				Dissolution amount per unit area / $\text{ppm}\cdot\text{mm}^{-2}$			
		Mg	Al	La	Ce	Mg	Al	La	Ce
Normal TRC	24	3.10657	1.09954	0.136890	0.275037	0.006618	0.002342	0.000292	0.000586
	48	4.87372	0.841169	0.158422	0.307328	0.010382	0.001792	0.000337	0.000655
Rapid solidification	24	2.39899	0.459788	0.152138	0.316834	0.006028	0.001155	0.000382	0.000796
	48	3.73850	0.232458	0.146644	0.280868	0.009394	0.000584	0.000368	0.000706

#### 4.5 Mechanical properties of the dual phase Mg-RE alloy

In order to check out whether the mechanical properties of the as-cast Mg-RE alloy were improved by using the processing method proposed by the current study, a tensile test was also conducted. The dimension of the specimen is shown in Fig. 4.41.

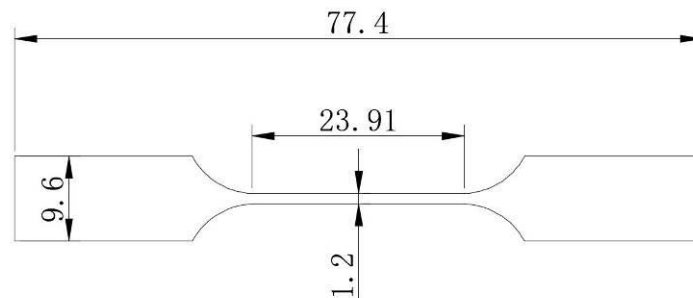


Fig. 4.41 Specimen dimension for tension test.

As shown in Fig. 4.42, the specimen was cut from the as-cast strip by a wire cutting machine. After that the specimen was grinded and polished. During the tensile experiment, a SHIMADZU IS-5000 tester with a tensile speed of 1.6mm/min at room temperature was adopted.



Fig. 4.42 Specimens used for tension test

Microstructure of the specimen surface and SEM image of the tensile fracture surface were shown in Fig. 4.43. In some place of the fracture surface, it showed a dimpled pattern, which implies a ductile fracture feature, the size of dimples varied slightly. Most of place reveals cleavage facets, which implies a brittle fracture feature.

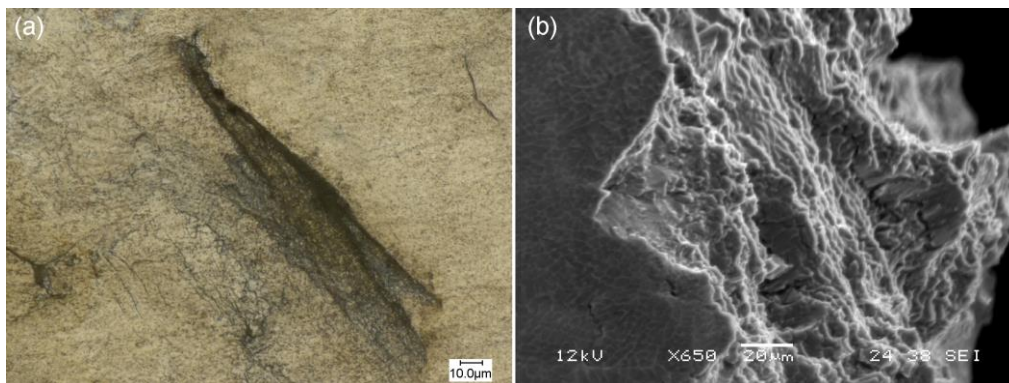


Fig. 4.43 Surface microstructures(a) and tensile fracture (b) of the specimen after tension test.

## Chapter 4 TRC experiment and microstructure analyses

Table 4.8 listed the ultimate tensile strength (UTS) of AZ31 as-cast strips at different casting conditions and the corresponding strips under different heat treatment. These AZ31 alloy strips were produced by the seniors in our laboratory. We list the data of these as-cast AZ31 strips here in order to compare these data with the Mg-RE alloy strip produced by rapid solidification process. The UTS and elongation of the Mg-RE alloy was list at the last. For a further comparison, some other Mg alloys are also listed in Table 4.9, and the data was taken from reference 9.

Table 4.8 Comparison of mechanical properties of AZ31 as-cast and homogenized 1h strips with Mg-RE alloy made by rapid solidification TRC process.

Strip No.	Casting speed (m/min)	Pouring temp. (K)	Strip Thickness (mm)	Homogenization temperature (K)	UTS (MPa)	Elongation (%)
A	8	973	3.58	as-cast	175.6	8.93
				623	191.24	10.57
				673	183.7	9.25
				723	178.4	7.65
B	13	953	2.78	as-cast	172.6	7.3
				623	188.87	6.92
				673	181.4	9.32
				723	217.8	12.3
C	18	953	2.05	as-cast	205.12	5.88
				623	182.04	8.21
				673	225	11.61
				723	220.47	10.98
D	30	973	1.05	as-cast	182.35	5.14
				673, 2h	82	3.6
Current work	30	953	1.1	As-cast	215.88	12.68

## Chapter 4 TRC experiment and microstructure analyses

Table 4.9 Tensile properties at room temperature for Mg alloys

Materials		UTS (MPa)	Elongation (%)	Ref.
Cast	AZ91(F)	131	1-3	[9]
	AZ91(T6)	235	3	
Cast	ZK60(F)	275	5	
	ZK60(T5)	314	4	
Powder metallurgy	AZ91	432	6	
Powder metallurgy	ZK61	400	7	
Alloys are annealed at 623K for 1.8ks after worm rolling at 473K.	Mg-5.5Li	131.5	52.3	
	Mg-8.5Li	121.2	65.2	
	Mg-8.5Li-1Y	121.2	64	

From the above comparison, we can get a conclusion ductility of the Mg-RE alloy made by rapid solidification TRC process was improve.

### 4.6 Concluding remarks

Rapid solidification of TRC experiments were conducted. The Mg-RE alloy strip exhibited good corrosion resistance and higher ultimate tensile strength and elongation comparing to the as-cast AZ31 alloy strips. The elongation of Mg-RE alloy strip is also high than the AZ91 and ZK61 under powder metallurgy processing. These indicate that Mg-RE alloy produced by our method has a better ductility. This may due to the special microstructure of the Mg-RE alloy forms, i.e., quasi-amorphous phase plus fine crystalline phase dual phase state. EPMA results and TEM analyses show that the quasi-amorphous phase has a high concentration in Al and RE element, which results in the fact that the quasi-amorphous phase has a better GFA than the matrix phase.

### References

- [1] Park S S, Bae G T, Kang D H, et al. Superplastic deformation behavior of twin-roll cast Mg–6Zn–1Mn–1Al alloy [J]. *Scripta Materialia*, 2009, 61(2): 223-226.
- [2] Chokshi A H, Mukherjee A K, Langdon T G. Superplasticity in advanced materials [J]. *Materials Science and Engineering: R: Reports*, 1993, 10(6): 237-274.
- [3] Liebermann H H. Rapidly solidified alloys made by chill block melt-spinning processes [J]. *Journal of Crystal Growth*, 1984, 70(1): 497-506.
- [4] Nakaura Y, Ohori K. Properties of AZ31 magnesium alloy sheet produced by twin roll casting [J]. *Materials Science Forum*, 2005, 488-489(1): 419-425.
- [5] Jung I-H, Sanjari M, Kim J, et al. Role of RE in the deformation and recrystallization of Mg alloy and a new alloy design concept for Mg–RE alloys [J]. *Scripta Materialia*, 2015, 102(1): 1-6.
- [6] Holzwarth U, Gibson N. The Scherrer equation versus the 'Debye-Scherrer equation' [J]. *Nature Nanotechnology*, 2011, 6(9): 534.
- [7] Pecharsky V K, Zavalij P Y. Properties, Sources, and Detection of Radiation [M]. *Fundamentals of Powder Diffraction and Structural Characterization of Materials*. Boston, MA; Springer US. 2009: 107-132.
- [8] Andrews K W, Dyson D J, Keown S R. Calculation of interplanar spacings and angles [M]. *Interpretation of Electron Diffraction Patterns*. Boston, MA; Springer US. 1967: 72-72.
- [9] Kubota K, Mabuchi M, Higashi K. Processing and mechanical properties of fine-grained magnesium alloys [J]. *Journal of Materials Science*, 1999, 34(10): 2255-2262.



## Chapter 5 Summary and prospect

### 5.1 Summary

In this thesis, the main target is to propose an effective rapid solidification method with low cost and high productivity to prepare amorphous or amorphous and fine grain mixed materials feasibly and practically. Improved ductility and better corrosion resistance are expected in our materials. Mg-RE alloy with quasi-amorphous phase plus fine crystalline phase dual phase microstructure was produced by our rapid solidification of TRC process. The rapid solidification process was realized by a faster casting speed and a thinner roll gap, it does not need any anther additional devices and vacuum environment.

In Chapter 2, thermodynamics and kinetics of glass formation were briefly introduced. Using the homogeneous nucleation theory, TTT diagram which indicates the transformation of crystalline phase form supercooled liquid state was plotted. Based on the additivity rule, CCT diagram was transformed from the TTT diagram. In the transformation process, we proposed two short programs to help calculation. And the critical cooling rates of materials to form metallic glasses were estimated.

Following the above, criteria for the formation of bulk metallic glasses were listed. We pointed out that all the criteria were based on analysis of abundant experimental data or proposed empirically and not appropriate for all the alloy systems. Referring to the criteria and considering the effects of alloying elements to Mg, three kinds of alloys (i.e., AZ31, AZ31-In-Sn and Mg-RE) were put forward as the objects for our study. Finally, the reasons why the above elements were selected were stated.

In Chapterr 3, thermal-flow simulation was carried out to calculate the thermal and

## Chapter 5 Summary and prospect

flow phenomena during TRC of magnesium alloys. In the VTRC process, simulation results under different casting conditions show that, we can attain a faster cooling rate using the center pouring mode comparing with the one side pouring mode when it forms a metal level in the molten pool because melt heat is extracted more efficiently of the former. However, for the situation of a molten pool with no formation of metal level (e.g., one side pouring mode-), a faster cooling rate could be attained in using the one side pouring mode. Changing the casting conditions or adopting the one side pouring mode could improve the temperature distribution of the pool metal, and the rolling block can be avoided. Cooling rates with 3 to 4 orders of magnitude by the VTRC process under the current conditions can be attained, which shows that VTRC technique has a potential ability in continuous fabrication of Mg-based bulk amorphous or amorphous phase and fine crystalline phase dual-phase alloys in sheet form.

In Chapter 4, rapid solidification of TRC experiments were conducted. The Mg-RE alloy strip exhibited good corrosion resistance and higher ultimate tensile strength and elongation comparing to the as-cast AZ31 alloy strips. The elongation of Mg-RE alloy strip is also high than the AZ91 and ZK61 under powder metallurgy processing. These indicate that Mg-RE alloy produced by our method has a better ductility. This may due to the special microstructure of the Mg-RE alloy forms, i.e., quasi-amorphous phase plus fine crystalline phase dual phase state. EPMA results and TEM analyses show that the quasi-amorphous phase has a high concentration in Al and RE element, which results in the fact that the quasi-amorphous phase has a better GFA than the matrix phase.

### 5.2 Prospect

RE alloying additions have generally been regarded as expensive alloying additions. In order to reduce the consumption of RE, ternary or a higher-order Mg alloy



## Chapter 5 Summary and prospect

would be a better choice in the future research. Addition of element Cu favors the formation of a nanocrystalline structure because it can hinder the growth of crystalline grain <sup>[1]</sup>. Meanwhile, Copper is one of a relatively small group of metallic elements which are essential to human health. These elements, along with amino and fatty acids as well as vitamins, are required for normal metabolic processes. In the future study, element Cu will be considered in designing new Mg-based quasi-amorphous alloys.

In the current study, SF10% was used, in the future work, it is better to consider other protective gas to make the process cost down and realize environmental protection.

### References

- [1] Suzuki K, Makino A, Inoue A, et al. Soft magnetic properties of nanocrystalline bcc Fe - Zr - B and Fe - M - B - Cu (M=transition metal) alloys with high saturation magnetization (invited) [J]. Journal of Applied Physics, 1991, 70(10): 6232-6237.

### Appendix

Programs used in constructing of CCT diagram.

(1)

```
>> syms T a c x;

for x=700:0.5:900

T=x:0.01:903;

a=(T./903);

c=(1-T./903);

y0=(2.58.*10.^-14).*(a.^-1.*c.^-0.75).*exp(0.268.*a.^-3.*c.^-2+0.4*(a./c).^0.75+2.24./(a-0.56)

);

y=1./y0;

q=trapz(T,y)

End
```

(2)

```
>> syms T a c x;

for x=400:0.5:700

T=x:0.01:706;

a=(T./706);

c=(1-T./706);

y0=(3.649.*10.^-14).*(a.^-1.*c.^-0.75).*exp(0.268.*a.^-3.*c.^-2+0.4*(a./c).^0.75+7./(a-0.35));

y=1./y0;

q=trapz(T,y)

End
```

## Appendix

### Related Publications

- [1] **ZP Pei**, DY Ju, HY Zhao, XD Hu. Thermal Flow-Solidification Simulation and Analysis of Strip Defects in Vertical Twin-Roll Casting of Magnesium Alloy. Materials Science Forum. 2015, 833: 15-18.
- [2] **Zhipu Pei**, Dongying Ju. Simulation of the Continuous Casting and Cooling Behavior of Metallic Glasses. Materials. 2017, 10(4): p1-9. (SCI Journal)
- [3] **Zhipu Pei**, Dongying Ju, Xue Li. Simulation of critical cooling rate and process conditions for metallic glasses in vertical type twin-roll casting. Transactions of Nonferrous Metals Society of China, 2017, 27(11): pp.2406-2414. (SCI Journal)

## Related Publications

## ACKNOWLEDGEMENTS

### ACKNOWLEDGEMENTS

I would like to express my sincere gratitude to my advisor, Prof. Dong-Ying JU, for taking me as his student and giving me the opportunity to pursue for my Ph.D. degree at Saitama Institute of Technology. Here, I would like to give my sincere thanks to Prof. JU for his support, encouragement and guidance throughout my study. Without his painstaking efforts in revising and polishing my drafts, the completion of the present thesis would not have been possible. I do appreciate his patience, encouragement, and professional instructions during my thesis writing. He devotes a considerable portion of his time to reading my manuscripts and making suggestions for further revisions.

I would like to thank Prof. S. Furuya, Prof. H. Ishizaki, Prof. R. Negishi and Prof. M. Uchida (alphabetical order), and for their productive suggestions and taking time away from their busy schedules to serve on my committee.

I would thank Prof. M. Uchida who gave me many valuable suggestions and help in microstructure measurement, Dr. R. Mukai for his help of preparing experimental device.

I would also thank all the Ju Laboratory members in over the years for their enjoyable help and collaboration.

My thanks also extend to all the peoples who engaged in or cooperated with our group in this research. I wish to sincerely thank all the professors and staff at SIT for their help. I would like to sincerely thank all the people who taught and gave hands to me.

I would like to acknowledge my funding sources. I received a JAPANESE GOVERNMENT (MONBUKAGAKUSHO: MEXT) scholarship during my study in Japan. I would like to express my heartfelt gratitude to the Japanese Government.

I would like to dedicate this work to my parents, Yu Pei & Yali Dai, and my aunt, Lin Dai. Their support gave me great courage to overcome all the difficulties during my study. Their love and encouragement has made me what I am.

February, 2018

Zhipu Pei